Silicon heterojunction solar cells on thin wafers – prospects in different utilization scenarios

Ugochi Kaosisochukwu Chime

Energie & Umwelt / Energy & Environment
Band / Volume 736
ISBN 978-3-95806-999-2

Mitglied der Helmholtz-Gemeinschaft

Schriften des Forschungszentrums Jülich
Reihe Energie & Umwelt / Energy & Environment Band / Volume 736

Forschungszentrum Jülich GmbH
Institute of Energy Materials and Devices (IMD)
Photovoltaik (IMD-3)

Silicon heterojunction solar cells on thin wafers – prospects in different utilization scenarios

Ugochi Kaosisochukwu Chime

Schriften des Forschungszentrums Jülich
Reihe Energie & Umwelt / Energy & Environment Band / Volume 736

ISSN 1866-1793 ISBN 978-3-95806-999-2

Bibliografische Information der Deutschen Nationalbibliothek.
Die Deutsche Nationalbibliothek verzeichnet diese Publikation in der Deutschen Nationalbibliografie; detaillierte Bibliografische Daten sind im Internet über http://dnb.d-nb.de abrufbar.

Herausgeber und Vertrieb: Forschungszentrum Jülich GmbH
Zentralbibliothek, Verlag
52425 Jülich
Tel.: +49 2461 61-5368
Fax: +49 2461 61-6103
zb-publikation@fz-juelich.de
www.fz-juelich.de/zb

Umschlaggestaltung: Grafische Medien, Forschungszentrum Jülich GmbH
Titelbild: KI-generiert

Druck: Grafische Medien, Forschungszentrum Jülich GmbH

Schriften des Forschungszentrums Jülich
Reihe Energie & Umwelt / Energy & Environment, Band / Volume 736

D 82 (Diss. RWTH Aachen University, 2026)

ISSN 1866-1793
ISBN 978-3-95806-998-5 (Print)
ISBN 978-3-95806-999-2 (E-Book)

Vollständig frei verfügbar über das Publikationsportal des Forschungszentrums Jülich (JuSER) unter www.fz-juelich.de/zb/openaccess.

Contents

Abstract

The urgent need to address climate change has accelerated the global transition from fossil fuels to renewable energy sources, with photovoltaics (PV) emerging as the fastest-growing technology in this field. By 2023, PV systems accounted for three-quarters of newly installed renewable energy systems, highlighting their central role in meeting global climate targets. Among PV technologies, crystalline silicon (c-Si) solar cells dominate the market due to their high efficiency, with silicon heterojunction (SHJ) solar cells demonstrating particularly strong potential. However, the transition to sustainable energy solutions requires strategies to reduce material usage, lower costs, and enhance the energy return on investment (ERoI). Reducing silicon wafer thickness has emerged as a promising approach, as theoretical studies predict high efficiencies for wafers in the 79–110 µm range. Despite the promise of thinner wafers, their experimental performance under diverse scenarios remains insufficiently explored, particularly for applications in tandem solar cells, indoor lighting, and module integration. This thesis systematically investigates the performance of thin wafer based SHJ solar cells under these different utilization scenarios, addressing the challenges and opportunities.

In the first part of this work, the impact of wafer thickness on the performance of single-junction SHJ solar cells was examined experimentally. Here, several SHJ solar cells of wafer thicknesses ranging from 60 to 170 µm were studied and their performance compared to theoretical predictions. In line with theoretical predictions, the implied open circuit voltage (iV_{OC}) was observed to increase as the wafer thickness reduced with some cells approaching the fundamental limit. However, contrary to predictions, the implied fill factor (*iFF*) was observed to reduce for thinner wafers due to the increased effect of surface recombination. Additionally, the short circuit current density (J_{SC}) was observed to reduce for thinner cells due to increased infrared light loss. The tradeoff majorly between the gains in V_{OC} and losses in J_{SC} resulted in a broad range of comparable high efficiency for cells between 75 μm and 170 μm.

In the second part of this work, the use of thin SHJ solar cells as bottom cells in perovskite-silicon tandem configurations was studied. Taking into considerations the major losses associated with thinner cells (surface recombination and infrared light loss), the potentials of increased passivation and light management were explored. Solar cells of wafer thicknesses of 80 μm and 135 μm were compared under standard AM1.5G and perovskite-filtered spectra. Under AM1.5G, thicker passivating layers improved passivation resulting in peak V_{OC} values of 747 mV for 80 μm cells and 741 mV for 135 μm cells. However, thicker passivation increased series resistance and parasitic absorption which resulted in lower efficiency compared to the standard passivation. Between wafer thicknesses, efficiency reduced slightly with thinner wafers, as the best 80 μm and 135 μm cells achieved efficiencies of 23.3% and 23.8%, respectively. However, under the perovskite-filtered spectrum, the effect of parasitic absorption was minimized due to the absence of short wavelength light under bottom cell conditions. Despite a 40% reduction in wafer thickness, the bottom-cell efficiency decreased only by 0.35%$_{abs}$ under the perovskite-filtered spectrum. Light management improvements, including an ITO/MgF_2/Ag back reflector and MgF_2 anti-reflection coating, resulted in enhanced J_{SC} . The back reflector increased J_{SC} by 0.58 mA/cm² for 80 μm cells and 0.52 mA/cm² for 135 μm cells, while the anti-reflection coating added ~0.3 mA/cm² across all cells.

In the third part of this thesis, the performance of thin SHJ solar cells under indoor lighting conditions, such as low light and LED illumination, which are relevant for applications in Internet of Things (IoT) devices, was studied. SHJ solar cells with thicknesses of 80 μm, 100 μm, 130 μm, and 170 μm under both solar and LED illumination demonstrated generally better open-circuit voltage, fill factor, and efficiency in the 80 μm and 100 μm cells under typical indoor conditions (250 – 500 LUX). While the 80 μm cells produced less power than the theoretically optimal 1.8 μm cells, they offered practical advantages due to their enhanced durability.

In the final part of this thesis, the transition of thin-wafer SHJ cells into modules was investigated, emphasizing laser cutting optimization, grid design, and mini-module

Abstract

performance. Laser cutting parameter sets were evaluated, with the optimized set achieving higher V_{OC}, FF, and overall efficiency, particularly for 80 µm cells. Grid design optimization further improved efficiency by reducing shading losses and series resistance, achieving a 0.6%$_{abs}$ efficiency gain. Mini-modules fabricated with 80 µm and 135 µm wafers showed no clear trends related to wafer thickness, as resistive losses introduced during soldering process overshadowed intrinsic thickness differences.

Zusammenfassung

Der dringende Bedarf, den Klimawandel zu bekämpfen, hat den globalen Übergang von fossilen Brennstoffen zu erneuerbaren Energiequellen beschleunigt, wobei die Photovoltaik (PV) als die am schnellsten wachsende Technologie in diesem Bereich hervorsticht. Bis 2023 entfielen drei Viertel der neu installierten erneuerbaren Energiesysteme auf PV-Systeme, was ihre zentrale Rolle bei der Erreichung globaler Klimaziele unterstreicht. Unter den PV-Technologien dominieren kristalline Silizium-Solarzellen (c-Si) den Markt aufgrund ihrer hohen Effizienz, wobei Silizium-Heterojunction (SHJ)-Solarzellen ein besonders hohes Potenzial aufweisen. Der Übergang zu nachhaltigen Energielösungen erfordert jedoch Strategien zur Reduzierung des Materialverbrauchs, Senkung der Kosten und Steigerung des Energierückflusses (ERoI). Die Reduzierung der Silizium-Wafer-Dicke hat sich als vielversprechender Ansatz herausgestellt, da theoretische Studien für Wafer im Bereich von 79–110 µm hohe Effizienzen vorhersagen. Trotz des Potenzials dünner Wafer bleibt ihre experimentelle Leistung in verschiedenen Szenarien, insbesondere für Anwendungen in Tandem-Solarzellen, Innenbeleuchtung und Modulintegration, weitgehend unerforscht. Diese Arbeit untersucht systematisch die Leistung von dünnen Wafer-basierten SHJ-Solarzellen in diesen unterschiedlichen Nutzungsszenarien und adressiert dabei die Herausforderungen und Chancen.

Im ersten Teil dieser Arbeit wurde experimentell untersucht, wie sich die Wafer-Dicke auf die Leistung von einkontaktigen SHJ-Solarzellen auswirkt. Dazu wurden mehrere SHJ-Solarzellen mit Wafer-Dicken von 60 bis 170 µm untersucht und ihre Leistung mit theoretischen Vorhersagen verglichen. Im Einklang mit den theoretischen Vorhersagen wurde festgestellt, dass die implizierte offenen Klemmenspannung (iV_{OC}) mit abnehmender Wafer-Dicke zunimmt, wobei einige Zellen dem fundamentalen Limit nahekommen. Im

Zusammenfassung

Gegensatz zu den Vorhersagen wurde jedoch beobachtet, dass der implizierte Füllfaktor (*iFF*) bei dünneren Wafern aufgrund des verstärkten Einflusses der Oberflächenrekombination abnahm. Zusätzlich nahm die Kurzschlussstromdichte (J_{SC}) bei dünneren Zellen ab, was auf erhöhte Verluste im Infrarotbereich zurückzuführen ist. Der Kompromiss zwischen den Gewinnen bei V_{OC} und den Verlusten bei J_{SC} führte zu einem breiten Bereich vergleichbar hoher Effizienzen für Zellen mit Dicken zwischen 75 µm und 170 µm.

Im zweiten Teil dieser Arbeit wurde die Verwendung von dünnen SHJ-Solarzellen als Bottom-Zellen in Perowskit-Silizium-Tandem-Konfigurationen untersucht. Unter Berücksichtigung der Hauptverluste dünner Zellen (Oberflächenrekombination und Infrarotlichtverluste) wurden die Potenziale von verbesserter Passivierung und Lichtmanagement erforscht. Solarzellen mit Wafer-Dicken von 80 µm und 135 µm wurden unter Standard-AM1.5G- und Perowskit-gefilterten Spektren verglichen. Unter AM1.5G verbesserten dickere Passivierungsschichten die Passivierung, was zu Spitzen- V_{OC} -Werten von 747 mV für 80 µm-Zellen und 741 mV für 135 µm-Zellen führte. Dickere Passivierungen erhöhten jedoch auch den Serienwiderstand und die parasitäre Absorption, was zu einer geringeren Effizienz im Vergleich zur Standard-Passivierung führte. Zwischen den Wafer-Dicken sank die Effizienz bei dünneren Wafern leicht, wobei die besten 80 µm- und 135 µm-Zellen Wirkungsgrade von 23,3 % bzw. 23,8 % erreichten. Unter dem Perowskit-gefilterten Spektrum wurde der Effekt der parasitären Absorption aufgrund des Fehlens von kurzwelliger Strahlung minimiert. Trotz einer Reduzierung der Wafer-Dicke um 40 % sank die Effizienz der Bottom-Zellen unter dem Perowskit-gefilterten Spektrum nur um 0,35 %abs. Verbesserungen im Lichtmanagement, einschließlich eines ITO/MgF_2/Ag-Reflektors und einer MgF_2-Antireflexbeschichtung, führten zu einer Erhöhung von J_{SC}. Der Reflektor erhöhte J_{SC} um 0,58 mA/cm² für 80 µm-Zellen und um 0,52 mA/cm² für 135 µm-Zellen, während die Antireflexbeschichtung über alle Zellen hinweg etwa 0,3 mA/cm² hinzufügte.

Im dritten Teil dieser Arbeit wurde die Leistung dünner SHJ-Solarzellen unter Innenbeleuchtungsbedingungen wie schwachem Licht und LED-Beleuchtung untersucht, die für Anwendungen in IoT-Geräten (Internet der Dinge) relevant sind. SHJ-Solarzellen mit Dicken von 80 µm, 100 µm, 130 µm und 170 µm zeigten unter sowohl Solar- als auch LED-Beleuchtung im Allgemeinen eine bessere offenen Klemmenspannung, einen höheren

Zusammenfassung

Füllfaktor und eine höhere Effizienz bei 80 µm- und 100 µm-Zellen unter typischen Innenbedingungen (250–500 Lux). Obwohl die 80 µm-Zellen weniger Leistung als die theoretisch optimalen 1,8 µm-Zellen erzeugten, boten sie praktische Vorteile aufgrund ihrer erhöhten Haltbarkeit.

Im letzten Teil dieser Arbeit wurde die Integration dünner Wafer-SHJ-Zellen in Module untersucht, mit einem Schwerpunkt auf der Optimierung des Laserschneidens, der Rastergestaltung und der Leistung von Mini-Modulen. Parameter für das Laserschneiden wurden evaluiert, wobei das optimierte Set höhere V_{OC} -, *FF*- und Gesamteffizienzen insbesondere für 80 µm-Zellen erzielte. Die Optimierung der Rastergestaltung verbesserte die Effizienz weiter, indem Verschattungsverluste und Serienwiderstände reduziert wurden, was zu einem Effizienzgewinn von 0,6 $\%_{abs}$ führte. Mini-Module, die mit 80 µm- und 135 µm-Wafern gefertigt wurden, zeigten keine klaren Trends in Bezug auf die Wafer-Dicke, da durch den Lötprozess eingeführte Widerstandsverluste die intrinsischen Dickenunterschiede überlagerten.

1. Introduction

The growing urgency of climate change necessitates a shift away from fossil fuels, which are a significant source of greenhouse gas emissions. To move towards a more sustainable future, the adoption of renewable energy has become essential in driving the global energy transition. This pressing need for an energy transition to effectively address climate change has resulted in an increased demand for renewable energy sources. Photovoltaics (PV) are central to this effort, along with other renewable energy sources such as wind, hydro, and geothermal power. Photovoltaics is currently the fastest-rising renewable energy source, and in 2023, accounted for three-quarters of newly installed renewable energy systems.[1] As reported by IRENA (2023), to align with the 1.5°C Scenario, global installed renewable power generation capacity must increase three-fold, rising from 3,382 GW in 2022 to 11,174 GW by 2030. In this context, PV capacity alone is expected to increase from 1,055 GW in 2022 to over 5,400 GW.[2] As demand for PV continues to grow, the development of cost-effective solar cells with high efficiency becomes increasingly important. Achieving these advancements will be crucial to meeting the predicted high demand for solar energy.

Today's solar cell market features several key technologies, including crystalline silicon, thin-film, and emerging perovskite cells. Thin-film solar cells, such as those made from amorphous silicon (a-Si), cadmium telluride (CdTe) and copper indium gallium selenide (CIGS), are known for their lightweight and flexible nature but generally offer lower efficiency.[3] Perovskite solar cells are an emerging technology with the potential for high efficiency and low production costs, though they are still largely in the research and development phase.[4] Crystalline silicon cells, including monocrystalline and polycrystalline types, dominate the market due to their high efficiency and reliability, with monocrystalline cells being the most efficient; these cells account for approximately 90% of global solar cell installations.[5]

Efforts to increase the efficiency of c-Si solar cells are ongoing and crucial for advancing renewable energy technologies. Although PERC (Passivated Emitter Rear Cell) solar cells currently lead the photovoltaic (PV) market due to their high performance and cost-effectiveness, they face a practical efficiency limit of around 24.5%, with mass production efficiencies nearing 23.3%. [6, 7] To surpass this limit, researchers are focusing on developing cell structures that accommodate better passivation of surfaces and interfaces. One promising approach involves silicon heterojunction (SHJ) solar cells, which combine silicon with thin layers of amorphous silicon to create a more efficient structure. SHJ cells have demonstrated the potential to achieve efficiencies of up to 27.3% in laboratory settings.[8]

Solar cells made from crystalline silicon have undergone significant advancements in recent years. The significant cost reductions and performance improvements[9] achieved over the past few decades have brought technology closer to its limits[10-12] and consequently, make further technical and economic progress on the solar cell level very challenging yet highly desirable. A potential way to enhance performance is to decrease the wafer thickness, which is associated with various benefits. To begin with, the reduction of material usage per solar cell area holds significant importance for global mass production. The reduction is motivated by the reduction of material usage, costs, CO_2 footprint[9] and supply chain resilience. For example, the European Commission considers Si as both a strategic and a critical raw material for green energy transition[13]. Utilization of thinner cut,[9, 14] exfoliated[15] or prepared in kerfless ways[16, 17] wafers leads to the production of larger active solar cell area per kg of Si. This approach has the potential to reduce costs and improve the energy return on investment (ERoI).[9] Additionally, thinner solar cells gain mechanical flexibility[18], making them well-suited for innovative applications such as building-integrated[19] or vehicle-integrated[20] systems. Solar cells based on thinner Si wafers have the advantage of requiring shorter diffusion lengths,[21] which reduces their sensitivity to bulk defect recombination and with ideal surface passivation these cells are more likely to achieve performance close to their intrinsic limits.[10] This improved capacity to withstand defects in bulk creates the possibility of achieving greater efficiencies using cost-effective materials, such as the upgraded metallurgical grade silicon.[22]

Introduction

Over the years, the thickness of crystalline silicon (c-Si) solar cells has been progressively reduced, with predictions indicating that it could fall below 100 micrometers.[9, 23] Given that industry-scale c-Si solar cells are expected to utilize the same feedstock for various applications, it is important to assess the implications of wafer thinning not only for traditional single junction silicon heterojunction (SHJ) solar cells but also for their roles as bottom cells in perovskite/silicon tandems, indoor applications, and their transition from cells to modules.

This thesis deals with the study of silicon heterojunction (SHJ) solar cells, with a primary focus on the effects of wafer thickness on their performance. It examines the effect of varying wafer thickness on the fundamental carrier dynamics such as carrier lifetime, and also on more practical cell parameters, such as the open-circuit voltage, fill factor, short-circuit current, and efficiency. The work is split into four parts: firstly, it investigates the impact of wafer thickness on single-junction SHJ solar cells; secondly, it analyzes the performance of thin SHJ cells as bottom cells in perovskite/silicon tandem configurations, evaluating how passivation layer thickness and light management strategies influence their performance. Additionally, the thesis assesses the performance of thin SHJ cells under indoor conditions, particularly under low light and LED illumination. Finally, it explores how wafer thickness affects the performance when soldered into shingle mini modules.

This thesis is structured as follows:

Chapter 2 provides a comprehensive understanding of solar cell technology and its core principles. Section 2.1 introduces the fundamentals of semiconductors and the formation of PN junctions. Section 2.2 covers important solar cell parameters with Subsection 2.2.1 discussing the electrical properties of solar cells, including efficiency (η), open-circuit voltage (V_{OC}), and short-circuit current density (J_{SC}), and fill factor (FF). Subsection 2.2.2 explores excess carrier dynamics such as charge carrier lifetime (τ) while Subsection 2.2.3 addresses quantum efficiency of solar cells. Section 2.3 discusses various loss mechanisms that limit the efficiency of solar cells with Subsection 2.3.1 covering optical losses, including reflection, transmission, and parasitic absorption. Subsection 2.3.2 looks into recombination losses. Subsection 2.3.3 discusses resistive losses, which result from resistance in the materials and electrical contacts. Subsection 2.3.4 discusses thermalization losses, where high-energy photons lose their excess energy as heat rather than contributing to the electrical current. Section 2.4 provides an overview of Silicon Heterojunction (SHJ) solar cells, highlighting their structure and components. Section 2.5 explores the effect of wafer thickness on solar cell performance. Section 2.6 addresses the fundamental performance limits of crystalline silicon solar cells, looking at theoretical efficiency limits and the role of wafer thickness in such limits. Section 2.7 introduces perovskite/silicon tandem solar cells, discussing the prospects of thin wafer SHJ as bottom cells. Section 2.8 examines the potential of thin SHJ solar cells for indoor applications. Section 2.9 discusses thin SHJ solar cells in shingle modules.

Chapter 3 outlines the experimental methods used to fabricate and characterize SHJ solar cells and mini modules. Section 3.1 describes the fabrication process of SHJ solar cells, including wafer preparation and thinning, deposition of thin films, and other functional layers. Section 3.2 covers the fabrication of mini modules, detailing the laser cutting and soldering process. Section 3.3 focuses on the characterization methods employed to evaluate solar cells and mini modules.

Chapter 4 examines the effects of wafer thickness on the performance of SHJ solar cells. Section 4.1 begins with an analysis of how different wafer thicknesses influence carrier lifetime. In Section 4.2, the impact of wafer thickness on key performance parameters is explored. Section 4.3 further investigates how varying the tilt angle of the solar cells affects performance in relation to wafer thickness. The chapter concludes with Section 4.4, summarizing the overall findings and implications for optimizing wafer thickness to enhance SHJ solar cell performance.

Chapter 5 focuses on the performance of thin SHJ solar cells under specific conditions, particularly when exposed to light filtered through a perovskite solar cell, emulating bottom cell operating conditions. Section 5.1 explores the effects of varying passivation layer thickness on cell performance, with Subsection 5.1.1 discussing light soaking effects, Subsection 5.1.2 examining intensity dependence, and Subsection 5.1.3 analyzing performance under a perovskite-filtered spectrum. Section 5.2 addresses light management strategies, including Subsection 5.2.1 on optimizing back reflectors and Subsection 5.2.2 on the effects of optimized back reflectors and anti-reflection coatings. Section 5.3 concludes with a summary of how passivation and light management impact the performance of thin SHJ solar cells under bottom cell conditions in perovskite/silicon tandems.

Introduction

Chapter 6 evaluates the performance of thin SHJ solar cells in indoor conditions. Section 6.1 examines how these cells perform under low light conditions and artificial LED illumination, assessing their efficiency and potential applications in indoor settings.

Chapter 7 discusses the development and optimization of mini-modules made from thin-wafer SHJ solar cells. Section 7.1 explores the optimization of laser cutting parameters for both 80 µm and 135 µm thick cells, comparing two parameter sets. Section 7.2 covers the optimization of contact grid designs to minimize shading and series resistance. Section 7.3 compares the performance of series connected 2- to 7-cell shingle mini-modules made from 80 µm and 135 µm c-Si wafers. Finally, Section 7.4 summarizes the findings, highlighting the benefits of thinner wafers for module performance.

Chapter 8 summarizes the research findings. It begins with a summary of the key findings and then concludes with an outlook on future research directions, offering recommendations for advancing c-Si solar cells based on thin wafers.

2. Fundamentals

In this chapter, the fundamentals of solar cells, with a focus on semiconductor physics and PN junctions, which are critical to their operation are introduced. Essential solar cell parameters are introduced, along with various loss mechanisms, including optical, recombination, and resistive losses. The concepts presented in this section are described with reference to the fundamental principles outlined in refs.[24-27]

2.1. Semiconductors and PN junctions

In simple terms, a solar cell, also known as a photovoltaic cell, is a device that converts light energy from the sun or any other light source into electricity. To understand the workings of this device, a slight delve into semiconductor physics is needed. When individual atoms come together to form a solid, their atomic orbitals overlap, causing their wave functions to interact. This interaction transforms initially discrete, quantized energy levels into extended states, resulting in the formation of multiple energy bands.[28] The band consisting of the highest occupied electronic state is called the valence band while the band with the lowest unoccupied energy state is the conduction band. These two bands are separated by a forbidden region, known as the energy band gap E_g, where no electron states are present. In semiconductors, the band gap is large enough to prevent the movement of electrons from the valence band to the conduction band but small enough to conduct when an external energy is applied as shown in Figure 2.1. In metals, there is an overlap between the two bands and the electrons flow freely between the bands without need for external energy. In insulators, however, the band gap is very large (approximately > 4 eV) and the transition of electrons between bands requires tremendous amount of energy.

In addition to the band gap energy, another important parameter which determines the electrical property of a semiconductor is the Fermi energy (E_F). This quantity is defined as the hypothetical energy level where there is a 50% probability of electron occupation at absolute zero atmosphere and at any given time. The Fermi level is usually located within the band gap and its proximity to the conduction band edge (E_C) or the valence band edge (E_V) gives information about the concentration of electrons and holes, respectively, in a material.

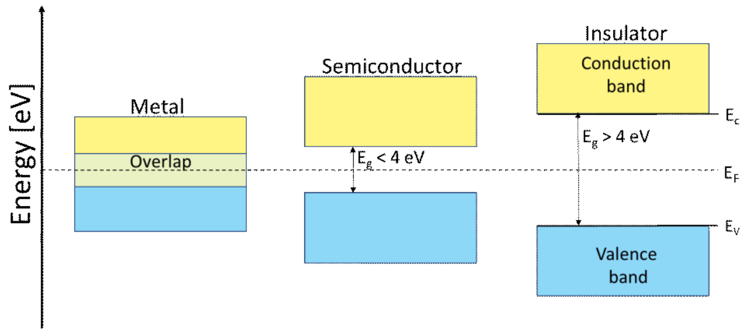

Figure 2.1: Schematic diagram of the band structures of metals, semiconductors, and insulators, showing the conduction band, valence band, energy band gap, and the Fermi energy.

Semiconductors can be classified into intrinsic and extrinsic semiconductors. Intrinsic semiconductors are pure materials without any impurities or external dopants. In thermodynamic equilibrium, the concentration of electrons (n) and holes (p) are equal. In this case, the E_F is located close to the center of the band gap. Extrinsic semiconductors contain impurities that were either unintentionally introduced during the material production process or intentionally added through doping to modify the material's conductivity. This doping can either increase the concentration of electrons (n-type) or create more holes (p-type). In silicon, the n-type semiconductor is produced by doping with an element that has one extra valence electron such as phosphorus which introduces donor energy levels just below the conduction band. Electrons in these donor levels require very little energy to migrate into the conduction band, increasing the concentration of free electrons that contribute to electrical conductivity. In contrast, p-type silicon is created by doping with an element that has one less electron than silicon, such as boron, which creates acceptor energy levels just above the valence band. Electrons from the valence band require very little energy to move into these acceptor levels, leaving behind mobile holes that act as positive charge carriers.

When a p-type semiconductor is placed in contact with an n-type semiconductor, a PN junction -which forms the basis of a diode and a solar cell – is formed at the interface between the two materials. The electrons and holes being the majority charge carriers for the n-type and the p-type materials, respectively, diffuse towards the region of lesser concentration through the junction. As the electrons diffuse from the n-type side towards the p-type side, they leave behind immobile positively charged ions. Similarly, the holes on the p-type side leave behind immobile negatively charged ions. This results in the formation of an electric field at the interface between the two semiconductors called the depletion region or space charge region (SCR) as shown in Figure 2.2(a). On the energy axis (Figure 2.2(b)), it can be seen as a band bending which creates a potential barrier that opposes the further diffusion of majority charge carriers.

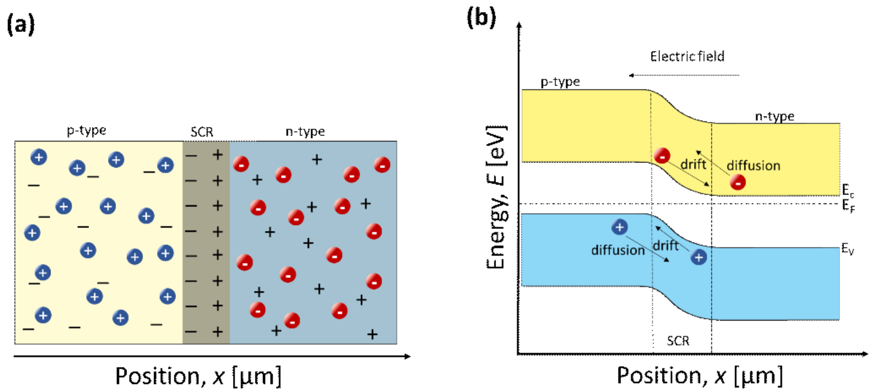

Figure 2.2: Schematic representation of (a) formation of the space charge (depletion) region at the interface of a p-type and n-type semiconductor due to the diffusion of majority carriers and the resulting fixed ionized charges.; (b) carrier transport in a PN junction showing band bending and the opposing drift and diffusion of electrons and holes along the energy bands.

When light is incident on a solar cell, the photons with energy equal to or greater than the bandgap of the absorber material excite the electrons from the valence band into the conduction band leaving behind holes in valence band. This results in a splitting of the Fermi energy level into two quasi-Fermi levels – one for the electron E_{FN} and one for the holes E_{FP}. The positions of these quasi-Fermi energy levels are dependent on the concentration of electrons and the holes within the conduction band and the valence band, respectively. The difference between E_{FN} and E_{FP} gives the maximum open circuit voltage (V_{OC}) a particular device can have. Due to the existing electric field in the space charge region, the electrons being the minority charge carriers on the p-side drift towards the n-side while the holes drift from the n-side to the p-side. In the presence of an external circuit, the electrons are collected from the n-side terminal, travel through the circuit (conducting electricity) and recombine with the hole on the p-side terminal.

2.2. Loss mechanisms in solar cells

Loss mechanisms in solar cells play a crucial role in defining the device's overall performance and efficiency. These losses can occur at different stages, such as light absorption, charge carrier generation and collection, and the transport of electrical current. While some losses are intrinsic and stem from fundamental properties of the material, it is important to understand all mechanisms to minimize losses and optimize solar cell efficiency. This section gives an overview of major loss mechanisms, including optical, recombination, resistive, and thermal losses, highlighting their impact on the efficiency of solar cells and strategies for mitigation.

2.2.1. Optical losses

Optical losses in solar cells pose significant challenges that have a direct impact on the short-circuit current and by extension, the overall efficiency of the device. These losses occur when incoming light photons are not successfully absorbed and utilized to generate electron-hole pairs, ultimately reducing the potential power output. A comprehensive understanding of these losses and the development of strategies to mitigate them is essential for optimizing solar cell performance. Figure 2.3 shows the principal optical losses in solar cells which include reflection, contact shading, transmission, and parasitic absorption.

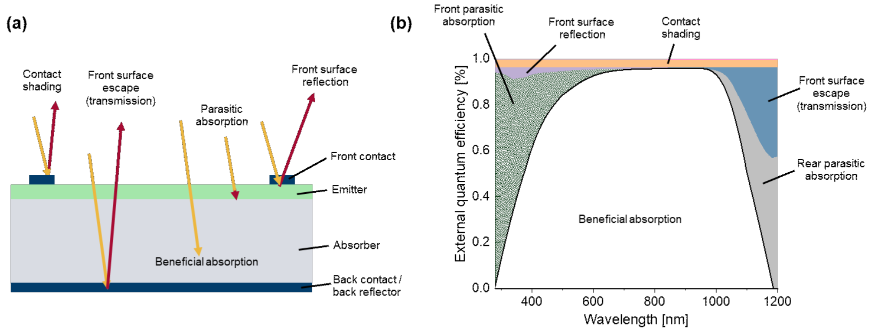

Figure 2.3: (a) Schematic representation of a solar cell showing the different optical loss pathways and (b) a representative external quantum efficiency curve of a solar cell showing useful portions of the light spectrum and portions lost to shading, reflection, transmission and parasitic absorption. Adapted from [29]

- **Front surface reflection:** Reflection losses in crystalline silicon (c-Si) solar cells occur when a portion of the incident sunlight is reflected off the cell's surface rather than being absorbed by the silicon wafer. This is particularly important in c-Si cells due to the high refractive index contrast between the air and the silicon wafer. For instance, a typical silicon wafer has a refractive index of about 3.5, while air has a refractive index of approximately 1.0, resulting in significant reflection at the air-silicon interface. To minimize reflection losses, anti-reflection coatings (ARCs) are commonly applied. These coatings typically have a refractive index that falls between that of air and silicon, which reduces the amount of reflected light by producing destructive interference at specific wavelengths. The thickness of the ARC is intentionally designed to enhance performance throughout the solar spectrum, thereby improving the cell's ability to absorb light. Additionally, surface texturing can be implemented to decrease reflection even more. In c-Si solar cells, the wafer surface is typically etched to create a pyramidal or random texture. This texturing enhances light incoupling and extends the path length of light within the wafer by causing multiple reflections within the textured surface, thereby increasing the probability of photon absorption reducing reflection losses.
- **Contact shading:** Metal contacts, which are essential for collecting and transporting the generated electron-hole pairs, contribute to optical losses in c-Si solar cells. These contacts, typically arranged as busbars and fingers on the front surface of the cell obstruct a portion of the incident light from reaching the active silicon absorber. The size of the

metal contact grid involves a compromise between minimizing optical shading and reducing electrical resistance. One innovative approach to addressing contact shading is the development of effectively transparent contacts (ETCs). ETCs are designed with a triangular cross-section which encourages the reflection of the incident light onto the absorber layer while maintaining a good conductivity.[30] Another approach is the fabrication of solar cells with interdigitated back contacts. In this case, all the contacts are situated on the rear side of the solar cell, eliminating the front-side shading.[31] However, the fabrication of IBC cells is complex and costly, hence, traditional designs are still more commonly used in the industry.

- **Transmission:** Transmission losses in solar cells occur when a portion of incident light passes through the cell without being absorbed. These losses are primarily influenced by the bandgap and thickness of the absorber material. Photons with energies below the bandgap of the material cannot be absorbed, regardless of the material's thickness. For crystalline silicon (c-Si) solar cells, which have a bandgap of approximately 1.12 eV, this results in the loss of photons with energies below this threshold. Additionally, as an indirect bandgap semiconductor, c-Si requires considerable thickness—typically in the range of hundreds of micrometers—to achieve effective absorption of photons. This presents a challenge for thin-wafer c-Si solar cells, where transmission losses can be significant. To enhance light absorption and mitigate transmission losses, strategies such as surface texturing and the incorporation of back reflectors are employed. Texturing increases the effective path length of light within the silicon, while back reflectors reflect transmitted light back into the absorber layer, providing a second opportunity for photon absorption. However, even with back reflectors surface texturing, front surface escape can still occur, where some internally reflected photons still leave the cell from the front side.
- **Parasitic absorption:** Parasitic absorption losses occur when incident light is absorbed by functional materials deposited on the solar cells. Instead of being absorbed by the active absorber material to generate electron-hole pairs, a portion of the incoming light is absorbed by materials such as passivation layers, transparent conductive oxides (TCOs), and even anti-reflective coatings. Since these losses cannot be completely eliminated due to their essential functions, it is important to optimize the thickness of these layers to

strike a balance between their roles in passivation or conductivity and maintaining transparency.

2.2.2. Thermalization

Thermalization occurs when photons with energy greater than the bandgap of the solar cell material excite electrons from the valence band to deeper levels within the conduction band. As these high-energy ("hot") electrons lose their excess energy, they quickly relax back to the edge of the conduction band, emitting the excess energy as heat. This process leads to significant energy loss, as the potential electrical energy is converted into heat rather than being harnessed for electricity generation. Thermalization is one of the major fundamental losses that limit the efficiency of conventional low-bandgap single-junction solar cells.[32] To mitigate this loss and enhance the utilization of the solar spectrum, tandem solar cells are employed.[33-35] In tandem cells, multiple layers of materials with different bandgaps are stacked, with the higher bandgap material placed at the top. This configuration allows the top cell to efficiently absorb higher-energy photons, while lower-energy photons that pass through are absorbed by the bottom cells with smaller bandgaps. By better matching the absorbed photon energy to the bandgap of each layer, tandem cells significantly reduce thermalization losses and improve overall energy conversion efficiency, making them a promising approach for achieving higher-efficiency solar cells. More of this will be discussed in Section 2.7. There are several other strategies to reduce thermalization losses, such as quantum dots[36], down conversion[37], and hot carrier solar cells[38]; however, these methods are largely still in the research phase.

2.2.3. Recombination losses

In an ideal solar cell, all generated charge carriers are collected at the terminals. However, in real situations, some electrons lose energy and recombine with holes before reaching the external contacts, leading to losses in the cell's open circuit voltage and by extension, the overall efficiency. Figure 2.4 illustrates a PN junction and the various recombination mechanisms that affect the efficiency of solar cells. These recombination mechanisms can be broadly classified into intrinsic and extrinsic types.

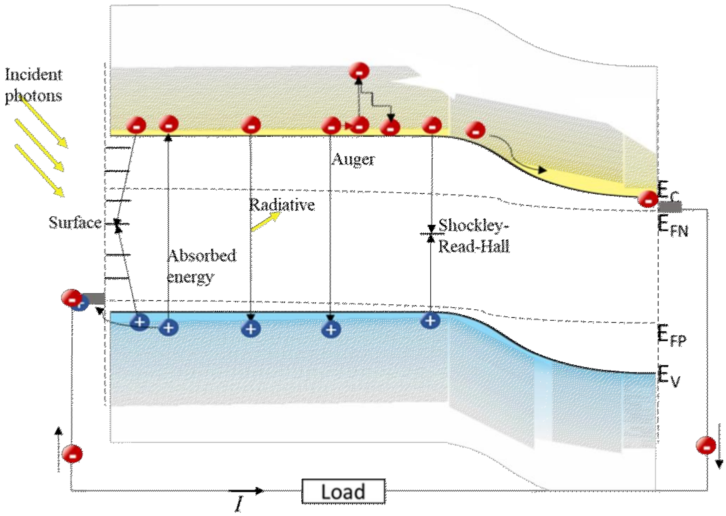

Figure 2.4: Schematic of a PN junction solar cell illustrating photogeneration, carrier separation, transport, and dominant recombination mechanisms.

2.2.3.1. Intrinsic Recombination

In low-temperature processed cells such as silicon heterojunction solar cells, intrinsic recombination is primarily governed by the fundamental material properties of the absorber and is largely unaffected by external factors during fabrication. There are two types of intrinsic recombination, and they are discussed below.

- **Radiative Recombination:** In radiative recombination, the direct opposite of electron-hole pair generation occurs. Here, an electron in the conduction band recombines with a hole in the valence band and emits a photon in the process. The energy of the emitted photon corresponds with the energy band gap of the absorber material. Since this recombination type involves only one electron and one hole, the radiative recombination rate is proportional to the product of the density of electrons and holes:

$$R_{rad} = B(pn - p_0 n_0) \tag{2.1}$$

where B is the coefficient of radiative recombination and $pn = (p_0 + \Delta n)(n_0 + \Delta n)$ and p_0 and n_0 are the hole and electron density in thermal equilibrium, respectively. The corresponding radiative lifetime becomes:

$$\tau_{rad} = \frac{\Delta n}{R_{rad}} = \frac{1}{B}\frac{1}{p_0 + n_0 + \Delta n} \tag{2.2}$$

Under low injection conditions i.e., when $\Delta n \ll p_0 + n_0 \approx N_{dop}$, the first part of the denominator dominates and the higher the dopant concentration N_{dop}, the lower the radiative lifetime. Consequently, for high injection conditions, i.e., when $\Delta n \gg p_0 + n_0$, the second part of the denominator dominates and τ_{rad} depends only on the excess charge carrier concentration. However, regardless of the injection conditions, the radiative lifetime in indirect semiconductors is relatively long and does not limit recombination in crystalline silicon solar cells. This is due to the inherently low value of the radiative recombination coefficient B in indirect semiconductors, where phonon participation is required, as opposed to direct bandgap materials, which exhibit much higher B values.

- **Auger Recombination:** The Auger recombination is a non-radiative process that involves three particles – two electrons and one hole (*eeh*) or one electron and two holes (*ehh*). In an *eeh* process, an electron, while recombining with a hole, transfers its energy to another electron in the conduction band and excites this electron into deeper states within the conduction band. Eventually, the newly excited electron relaxes back to the conduction band edge while releasing the excess energy in the form of phonons. A similar mechanism takes place for the *ehh* process except in this case, the energy transfer occurs within the valence band. The net Auger recombination rate R_{Auger} is the sum of the recombination rates of the *eeh* and the *ehh* processes, each being proportional to the respective carrier densities involved.

$$R_{Auger} = R_{eeh} + R_{ehh} = C_p(p^2 n - p_0^2 n_0) + C_n(n^2 p - n_0^2 p_0) \tag{2.3}$$

where C_p and C_n are the hole- and electron-related Auger coefficients, respectively. For n-type c-Si under low injection conditions, the Auger recombination lifetime can be approximated as:

$$\tau_{Auger,li} = \frac{1}{C_n N_D^2} \tag{2.4}$$

And under high injection conditions,

$$\tau_{Auger,hi} = \frac{1}{(C_p + C_n)\Delta n^2} \tag{2.5}$$

From the equations, it can be concluded that probability of Auger recombination steeply increases at high charge carrier concentrations which can be due to high injection conditions or high dopant concentration in the solar cell. In c-Si solar cells, the theoretical maximum efficiency is mostly limited by the Auger recombination.

2.2.3.2. Extrinsic Recombination

Extrinsic recombination is governed by the existence of defects and impurities in the semiconductor material and can be controlled by external endeavors in the production process of the cell. The types of extrinsic recombination are discussed below:

- **Shockley-Read-Hall (SRH) Recombination:** In this type of recombination, the electrons and holes recombine with the help of localized energy states or traps within the band gap which are created as a result of impurities, intentionally added dopant atoms, or defects within the crystal lattice. The tendency of a trap to capture an election or hole is described by its electron or hole cross-section (σ_n, σ_p). When σ_n is much higher than σ_p, the trap captures an electron from the conduction band and after a short time, the electrons are re-emitted into the conduction band and the probability of recombination is low. This is also the same for holes when σ_p is greater than σ_n. However, when σ_n and σ_p are comparable, the probability of recombination is much higher, and these kinds of traps are called recombination centers. In this case, firstly, the electron falls from the conduction band into the trap (electron capture) and emits vibrations within the lattice known as phonons then the electron loses more energy and drops into the valence band (hole capture).

  The SRH recombination rate R_{SRH} is expressed as:

$$R_{SRH} = \frac{np - n_i^2}{\tau_p(n + n_1) + \tau_n(p + p_1)} \tag{2.6}$$

  where n_1 and p_1 are the electron and hole concentrations in the conduction and valence bands, respectively, if the trap energy level (E_T) equals the Fermi energy level (E_F). The electron and hole lifetimes (τ_n, τ_p) are defined respectively as:

$$\tau_n = \frac{1}{\sigma_n v_{th} N_T} \tag{2.7}$$

$$\tau_p = \frac{1}{\sigma_p v_{th} N_T} \tag{2.8}$$

  where v_{th} is the thermal velocity of the charge carriers and N_T is the density of trap states in the material.

- **Surface Recombination:** Surface recombination is a specific form of SRH recombination that takes place at the surface of a semiconductor, where the crystal lattice terminates abruptly, creating dangling bonds. These dangling bonds create some energy states at the surface of the material which can be recombination centers for the generated electron-hole pairs that migrate towards the surface. In monocrystalline silicon solar cells, surface recombination dominates the bulk SRH recombination due to their high purity and inexistent grain boundaries within the bulk.

2.2.4. Resistive losses

Resistive losses in solar cells occur due to electrical resistance within the device that hinders the smooth flow of current. These losses mainly come from two sources: series resistance and shunt resistance. Both types of resistance significantly influence the fill factor and the overall energy conversion efficiency of the cell.

- **Series Resistance:** Series resistance (R_S) in a solar cell is the internal resistance encountered by electrons as they travel through the cell's structure and external connections. This resistance results from various factors, such as the semiconductor material's intrinsic resistance, the contact resistance between the semiconductor and metal grids, and the resistance of metal contacts and interconnections. High series resistance negatively impacts the solar cell's performance by reducing its operating voltage, thereby decreasing the fill factor and ultimately lowering the cell's overall efficiency. R_S can be extracted for the IV curve as the slope of the steep side of the curve near the V_{OC}.[39] To minimize series resistance, care is taken to optimize material quality, improve contact interfaces, and refine the cell's design to shorten the distance charge carriers must travel.
- **Shunt resistance:** Shunt resistance (R_{SH}) is a parallel resistance to the solar cell's PN junction that helps prevent leakage current by blocking unwanted paths, which often arise from manufacturing defects or impurities. A low shunt resistance is detrimental to the solar cell's performance, as it provides an alternative path for the current, reducing the voltage across the cell and lowering both the fill factor and overall efficiency. R_{SH} can be extracted from the IV curve as the slope of the steep side of the curve near the J_{SC}.[39] The effect of shunt resistance is more pronounced under low light intensity because the

lower generated current means that a larger percentage is lost through defects and shunts.[40]

2.3. Solar cell parameters

The performance of solar cells is determined by several key parameters. For instance, the current density–voltage (JV) characteristics provide valuable information about the electrical performance of a solar cell, including the open-circuit voltage, short-circuit current density, fill factor, and efficiency. To assess the potential of a silicon solar cell during the early stages of the fabrication process, excess carrier dynamics are studied. To understand the optical performance of a solar cell, the quantum efficiency is a crucial parameter. This section will discuss the important parameters that define the performance of solar cells in detail.

2.3.1. Electrical Properties

The electrical properties of a solar cell are typically described using its current-voltage (*JV*) characteristics. Figure 2.5 shows a typical *JV* curve of a solar cell. The important parameters obtained from this curve are discussed below.

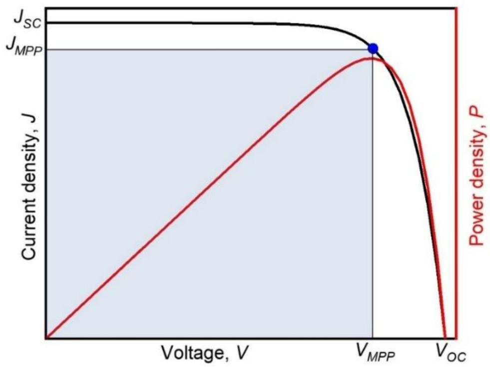

Figure 2.5: Illuminated current density - voltage (black) and power density - voltage (red) characteristics of a solar cell showing the open circuit, short circuit and maximum power point working conditions.

- **Short-circuit current density (J_{SC}):** The short-circuit current density represents the maximum amount of generated charge carriers flowing through the solar cell per unit area at short circuit. The J_{SC} is dependent on many factors, such as the intensity and spectrum of the incident light, the absorption coefficient, the thickness of the absorber material and the current collection efficiency of the device.

- **Open-circuit voltage (V_{OC}):** The open-circuit voltage is the difference in potentials between the two terminals of a solar cell as a result of accumulation of charge carriers when there is no current flow (i.e., in open circuit conditions). In the absence of losses due to imperfect contact selectivity, the V_{OC} can be described as the difference between the two quasi-Fermi levels in the PN junction. The V_{OC} is majorly determined by the lifetime of the electron-hole pairs and the temperature of the cell.
- **Maximum power density point (P_{MPP}):** The maximum power density point is the point on the *JV* curve where the cell generates the highest possible power. It is characterized by a specific voltage (V_{MPP}) and current (I_{MPP}), which correspond to the voltage and current at which the product of these two values reaches its maximum. Operating at the P_{MPP} ensures that the solar cell delivers the highest possible energy output.
- **Fill factor (*FF*):** The fill factor is given as a ratio of the maximum power (P_{MPP}) to the product of the J_{SC} and the V_{OC}. The *FF* is mainly affected by the series resistance, shunt resistance and defect-assisted recombination present within the cell.
- **Efficiency (η):** The efficiency of a solar cell is defined as the ratio of the maximum power output (P_{MPP}) generated by the cell to the incident power input received from the sun or any other light source. The efficiency gives comparable information on the performance of a solar cell and can be expressed as Equation 2.9.

$$\eta = \frac{J_{SC} \times V_{OC} \times FF}{P_{in}} \tag{2.9}$$

where P_{in} is the is the power density of the light incident on the solar cell. Under standard test conditions (AM 1.5g, 25 ^{o}C), P_{in} is 100 mW/cm^2.

To explain the *JV* behavior of a solar cell, a two-diode model is used, with the corresponding equivalent circuit shown in Figure 2.6.

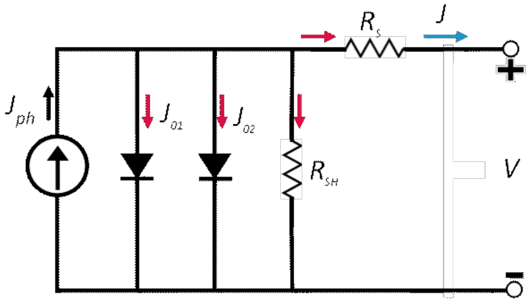

Figure 2.6: Equivalent circuit of a solar cell based on the two-diode model, including series resistance, shunt resistance, and recombination current paths.

This model depicts the combination of the collected photo-current and the injected current caused by the voltage at the PN junction as a constant current source parallel to two ideal diodes. The first diode, representing the ideal diode according to Shockley's diode equation, accounts for the diffusion current and is characterized by a saturation current density (J_{01}) influenced by recombination in the base, emitter, and their surfaces. The second diode, characterized by the saturation current density J_{02}, represents the recombination losses in the space charge region of the solar cell, which are significant in understanding the non-ideal behavior and efficiency losses in real solar cells. In addition to recombination losses, other factors such as series resistance (R_S) in the bulk of the solar cell or the external contact, as well as poor shunt resistance (R_{SH}), contribute to the overall performance of the solar cell and are all represented in the two-diode model in Equation (2.2).[41]

$$J(V) = J_{01}\left[exp\left(\frac{q(V-J(V)R_S)}{n_1kT}\right)-1\right]+J_{02}\left[exp\left(\frac{q(V-J(V)R_S)}{n_2kT}\right)-1\right]+\frac{V-J(V)R_S}{R_{SH}}-J_{ph} \tag{2.10}$$

where n_1 and n_2 represent the ideality factor for the first and second diodes and usually have the values of 1 and 2, respectively.

2.3.2. Excess carrier dynamics

Understanding the excess carrier dynamics is essential for analyzing the recombination processes that directly influence the efficiency of solar cells. Key parameters such as the effective minority carrier lifetime (τ_{eff}) and surface recombination velocity (S) which provide valuable insights into how long carriers remain in an excited state and how surface interactions affect their recombination are discussed here.

- **Effective minority carrier lifetime (τ_{eff}):**

  The effective minority carrier lifetime refers to the average duration that a carrier remains in an excited state following electron-hole generation before it recombines. The rate at which this recombination takes place is given as the ratio of the excess charge carrier (Δn) to the effective lifetime (τ_{eff}). In a non-steady-state condition, the rate of change in Δn is given as the continuity equation in Equation (2.3).

$$\frac{d(\Delta n)}{dt} = G(t) - \frac{\Delta n}{\tau_{eff}} \quad (2.11)$$

  where $G(t)$ is the generation rate of charge carriers.

  The effective lifetime is then given as

$$\tau_{eff} = \frac{\Delta n}{G(t) - \frac{d(\Delta n)}{dt}} \quad (2.12)$$

  This equation can be analyzed under two conditions: Under quasi-steady-state condtions, the generation rate $G(t)$ equals the recombination rate $R(t)$, hence the rate of change of excess charge carriers is zero and τ_{eff} becomes $\frac{\Delta n}{G(t)}$. In transient conditions, $G(t)$ is zero, and the effective lifetime becomes dependent only on the rate of change of excess charge carriers. More of this is discussed in Section 3.3.

- **Surface recombination velocity (S)**

  The surface recombination velocity (S) quantifies the rate at which charge carriers recombine at the surface of a semiconductor material, providing insight into the passivation quality of the cell. The net sum of all losses due to recombination that takes place in a silicon wafer is described by the effective lifetime (τ_{eff}) of the wafer. In the context of this work, isolation of the bulk and surface contributions to the effective lifetime is of interest. A common expression for the effective lifetime with bulk and surface lifetime components is[42]:

$$\frac{1}{\tau_{eff}} = \frac{1}{\tau_B} + \frac{2S}{W} \quad (2.13)$$

  where τ_B is the bulk lifetime, S is the surface recombination velocity and W is the thickness of the wafer. The second part of the equation represents the inverse of the surface recombination lifetime. Although this conditional "spatial" separation of recombination channels does not describe types or mechanisms of recombination, it is typical that surface recombination is dominated by Shockley-Read-Hall (SRH) or trap assisted mechanism[43, 44] due to high density of trap states at the surfaces and interfaces.[45, 46]. The surface recombination on the front and back surfaces can differ due to the actions of n- and p-type layers; however, for the sake of simplicity, they are assumed to have identical values. By using identical silicon wafers of varying thicknesses, the value of 2*S* can be determined as the slope of the linear fit of the plot of $\frac{1}{\tau_{eff}}$ with respect to $\frac{1}{W}$. The bulk lifetime, which is assumed uniform for all wafers, is obtained as the inverse of the intercept of the fit on the $\frac{1}{\tau_{eff}}$ axis.

- **Differential ideality factor**

The differential ideality factor, n_{id}^{diff} provides a valuable insight into how a solar cell deviates from ideal diode behavior. It serves as a diagnostic tool for identifying the dominant recombination mechanisms under various injection conditions. While the recombination mechanisms are discussed in Section 2.2.3, key characteristics relevant to this analysis are briefly introduced here.

The total recombination rate *R* in a semiconductor is generally expressed as the sum of the radiative, Shockley-Read-Hall (SRH), and Auger recombination components:

$$R = R_{rad} + R_{SRH} + R_{Aug} \tag{2.14}$$

In crystalline silicon (c-Si) solar cells, radiative recombination is typically negligible due to its relatively low probability. Therefore, the total recombination rate c-Si simplifies to:

$$R \approx R_{SRH} + R_{Aug} = \frac{np - n_i^2}{n\tau_p + p\tau_n} + C_n n^2 p + C_p p^2 n \tag{2.15}$$

The quasi-Fermi level splitting which defines the implied open circuit voltage of the cell is related to the charge carriers concentrations as:

$$\Delta E_F = qiV_{OC} = kT \ln \frac{np}{n_i^2} \tag{2.16}$$

Under low injection conditions ($n \approx N_D$ and $p \approx \Delta n$) for n-type c-Si:

Here, Auger recombination is negligible and SRH recombination is minority-carrier dominated:

$$R \approx \frac{\Delta n}{\tau_p} \tag{2.17}$$

Hence,

$$R \propto \Delta \text{n} \propto exp\left(\frac{\Delta E_F}{kT}\right) \tag{2.18}$$

This implies that $n_{id}^{diff} \approx 1$.

Under high injection conditions ($n \approx \Delta n > N_D$ and $p \approx \Delta n$):

For SRH recombination,

$$R \approx \frac{\Delta n}{\tau_p + \tau_n} \tag{2.19}$$

$$\Delta E_F \approx kT \ln\frac{\Delta n^2}{n_i^2} \approx 2kT \ln\frac{\Delta n}{n_i} \tag{2.20}$$

Hence,

$$R \propto \Delta \text{n} \propto exp\left(\frac{\Delta E_F}{2kT}\right) \tag{2.21}$$

This implies a symmetric SRH recombination of both the minority and majority charge carriers within mid-gap trap. Here, $n_{id}^{diff} \approx 2$.

Under very high injection conditions ($\Delta n \gg N_D$):

Here, Auger recombination is dominant hence, *R* becomes a three-particle process.

$$R \approx C_n \Delta n^3 \tag{2.22}$$

Deriving from Equation (2.21),

$$R \propto \Delta n^3 \propto exp\left(\frac{3\Delta E_F}{2kT}\right) \tag{2.23}$$

In this case, $n_{id}^{diff} \approx {}^{2}/_{3}$.

Numerical simulations can be used to illustrate the behavior of n_{id}^{diff} under different recombination regimes. In such simulations, the implied open-circuit voltage is computed as a function of generation rate, which is varied systematically to represent different injection levels. At each generation level, the corresponding carrier concentrations n and p are calculated, and the total recombination rate R is evaluated according to Equation (2.15). The differential ideality factor is then calculated using:

$$n_{id}^{diff} = \frac{q}{kT}\frac{\mathrm{d}iV_{OC}}{\mathrm{d}lnR} \quad (2.24)$$

Figure 2.7 shows a simulation of n_{id}^{diff} for three distinct recombination conditions: (i) pure SRH recombination, (ii) pure Auger recombination, and (iii) a combined case including both SRH and Auger terms. The figure clearly demonstrates the expected transitions across injection levels. At lower voltages, n_{id}^{diff} approaches 1, consistent with minority-carrier SRH recombination. As voltage increases, n_{id}^{diff} rises toward 2, reflecting symmetric SRH via mid-gap traps. At high voltages, typically above 700 mV [31], the curve bends downward toward, indicating Auger recombination dominance.

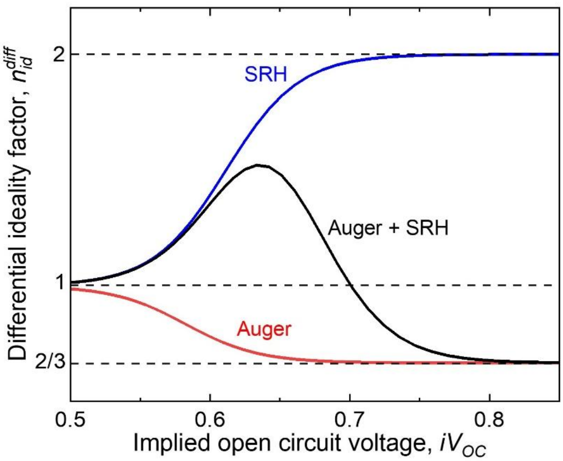

Figure 2.7: Illustration of differential ideality factor vs. implied open-circuit voltage highlighting dominant recombination mechanisms across injection levels in c-Si solar cells.

To simulate the effect of wafer thickness, the effective lifetime can be adjusted to represent typical lifetimes observed for different wafer thicknesses. The impact of wafer thickness on recombination dynamics will be discussed in more detail in Section 4.1. Using the quasi-steady-state and photoconductance measurement technique, the differential ideality factor n_{id}^{diff} of a doped c-Si wafer can be calculated directly from measured data using Equation (2.25)[47]:

$$n_{id}^{diff} = \frac{q}{kT}\frac{\mathrm{d}iV_{OC}}{\mathrm{d}ln(\varphi)} \tag{2.25}$$

where φ is the implied intensity of the light pulse in suns.

- **Implied current density-voltage (*JV*) characteristics**

The implied *IV* characteristics represent the wafer's ideal performance as a solar cell, assuming no additional recombination losses in further processing steps. The photoconductance measurements can be used to obtain the implied *JV* characteristics of Si wafers by generating a series of excess carrier concentrations (Δn) in the wafer through varying illumination intensities. For each Δn, the implied open-circuit voltage (iV_{OC}) is calculated using Equation (2.26):

$$iV_{OC} = \frac{kT}{q} ln\left[\frac{(\Delta n + N_D)\Delta n}{n_i^2}\right] \tag{2.26}$$

The photogeneration current density J_{ph} is derived based on the assumption of carrier balance under steady-state illumination. Specifically, the rate at which electron-hole pairs are generated is equal to the rate at which they recombine:

$$J_{ph} = J_{rec} \tag{2.27}$$

This steady-state condition allows J_{ph} to be expressed in terms of an effective minority carrier lifetime:

$$J_{ph} = \frac{q\Delta nW}{\tau_{eff}} \tag{2.28}$$

In quasi-steady-state and photoconductance (QSSPC) measurements, the implied short-circuit current density (iJ_{SC}) is derived by comparing this recombination-based photogeneration J_{ph} against a calibrated reference value. For example, under 1-sun AM1.5G illumination, a standard 380 µm thick silicon wafer is expected to generate approximately 38 mA/cm².[48] This reference allows the system to assign a photogeneration current to each illumination level. In the case of this work, the QSSPC software expresses the photogeneration data as:

$$iJ = 0.038 \left(\frac{A}{cm^2}\right) - J_{ph} \tag{2.29}$$

By plotting the implied current density (*iJ*) against the corresponding implied open-circuit voltage (iV_{OC}) for each excess carrier concentration, the implied *JV* curve is generated. This curve represents the ideal electrical performance of the wafer, assuming only recombination losses and no resistive, contact-related, or optical losses.

Following the reconstruction of this implied *JV* curve, the maximum power point (iJ_{MPP}, iV_{MPP}) can be identified. The implied fill factor (*iFF*), which provides an upper limit to the fill factor that a solar cell made from the wafer could achieve, can be obtained as:

$$iFF = \frac{iJ_{MPP} \times iV_{MPP}}{iJ_{SC} \times iV_{OC}} \tag{2.30}$$

It is important to note that implied values derived from QSSPC measurements are fundamentally more reflective of the material's chemical and recombination properties rather than its actual electrical behavior, since no lateral charge transport occurs during the measurement. Only generation and recombination processes are involved. Nevertheless, the implied *JV* curve provides an important upper limit for the expected electrical performance of the final solar cell.

2.3.3. Quantum efficiency

Quantum efficiency (QE) is a measure of the effectiveness of a device in converting incident photons into electrical charge carriers. There are two primary types of quantum efficiency: external quantum efficiency (EQE) and internal quantum efficiency (IQE). EQE is the ratio of the number of charge carriers collected by the device to the number of incident photons, including losses due to reflection. By integrating the EQE over the entire solar spectrum and considering the photon flux ($\Phi(\lambda)$), the short-circuit current density can be derived as:

$$J_{SC} = q \int \Phi(\lambda) \mathrm{EQE}(\lambda) d\lambda \tag{2.31}$$

The internal quantum efficiency (IQE), on the other hand, is the ratio of collected charge carriers to the number of absorbed photons, excluding losses due to reflection but including recombination losses within the device as is related to the EQE as

$$IQE = \frac{EQE}{1-R} \tag{2.32}$$

The IQE provides insight into the intrinsic material quality and the effectiveness of the photoactive layer in generating charge carriers from absorbed photons.

2.4. Silicon Heterojunction Solar Cells

Heterojunctions, unlike homojunctions, are defined by an interface that involves two semiconductors with different bandgaps. Silicon heterojunction solar cells usually consist of crystalline silicon (E_g = 1.12 eV) absorber sandwiched between intrinsic and doped amorphous silicon (E_g = 1.7 eV) layers, creating an n/i/c-Si/i/p stack. SHJ solar cells are a highly promising solar cell technology due to their high efficiency and low production costs related to temperature and materials. These cells are anticipated to become the industry standard for photovoltaic (PV) production, following the widespread adoption of passivated emitter and rear contact (PERC) technology[6, 7, 23]. Since the initial report on amorphous/crystalline silicon heterojunctions by Fuhs et al. in 1974[49], several research have been done in the improvement and development of silicon heterojunction solar cells.[31, 50-57] Currently, SHJ solar cells produced by LONGi company hold the world record efficiency of 27.30% for single-crystalline silicon solar cells[8]

Figure 2.8(a) shows a typical schematic of SHJ solar cells. The absorber material is usually made up of monocrystalline silicon which can be n-type or p-type[58]. N-type c-Si wafers are the preferred absorber material due to their immunity to boron-oxygen defects and hence, their lower light-induced-degradation (LID)[59], and their reduced susceptibility to interstitial metallic impurities, such as iron.[60] Before further depositions, the absorber wafer is usually texturized to create rough surfaces which improve the light absorption. The texturing could be done using wet reagents such as KOH and NaOH or dry processes such as Reactive Ion Etching which employs sulfur hexafluoride/oxygen (SF6/O2) plasmas.[61]

Fundamentals

Dangling bonds, which are comprised of unpaired electrons, are present on c-Si wafer surfaces. These bonds act as sites for recombination and are particularly prominent in textured surfaces. To suppress these surface defects, passivation layers are usually deposited on both sides of the wafer. There are two approaches that can work together in effectively passivating a surface. One of them is chemical passivation, where the vacant sites of the dangling bonds are filled by depositing thin films, such as hydrogen-rich dielectric materials. The second approach is field effect passivation, which involves the creation of an electric field near the surface, causing the minority charge carriers to be repelled from it, thus minimizing surface recombination.[62, 63] This can be accomplished by depositing highly doped films of a specific polarity on the surface.

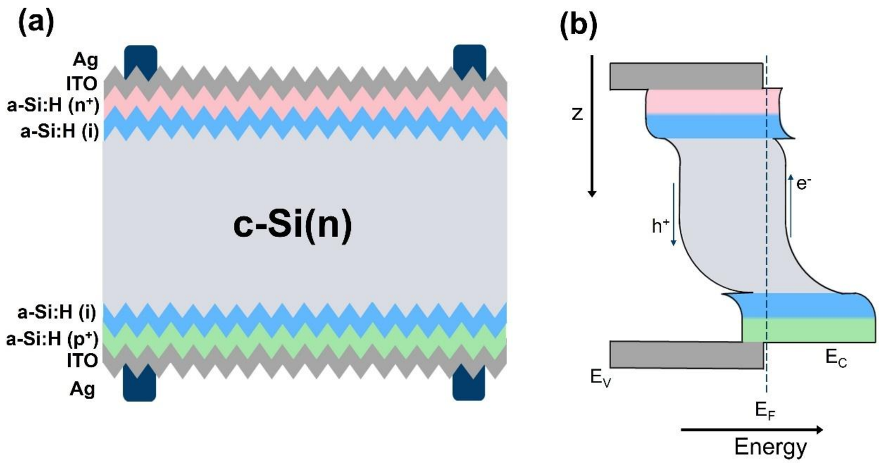

Figure 2.8: Schematic diagram of (a) a typical silicon heterojunction solar cell showing the passivation, doped and conductive layers and (b) band diagram showing band bending caused by each layer of the SHJ solar cell. Adapted from [64]

Hydrogenated amorphous silicon (a-Si:H) is widely utilized in SHJ solar cells due to its exceptional passivation properties, slightly broader bandgap, developed deposition technologies, and low-temperature (<200°C) deposition process, which enables the use of extremely thin wafers without causing substrate warping.[64, 65] Firstly, a chemical passivation is usually achieved by the plasma enhanced chemical vapor deposition (PECVD) of thin intrinsic layer of a-Si:H, which results in the formation of Si-H and Si-Si bonds on the surface, thereby efficiently suppressing dangling bonds.[66] The buffering effect originates from band offsets, which are the result of a disparity in bandgap energies between c-Si (1.1 eV) and a-Si:H (1.7 eV), as depicted in Figure 2.8(b).

To ensure field-effect passivation, an n-doped a-Si:H thin film is deposited on one side of the wafer, directly on top of the a-Si:H(i) layer, while a p-doped a-Si:H layer is placed on the opposite side. This creates a PN junction, resulting in the formation of an electric field, which encourages the transport of minority charge carriers away from the surface and reduces the likelihood of recombination, as demonstrated by the band-bending shown in Figure 2.8(b).[62, 63] At the c-Si/a-Si:H interfaces, the energy barriers created by the narrow spikes originating from the band offset can be overcome by band-to-band tunneling, trap-assisted tunneling or thermionic emission.[67] In n-type SHJ solar cells, the emitter layer, which is typically p-doped, can be deposited either on the front or rear side of the wafer. However, frontside emitters require a complex evaluation of the optoelectrical performance trade-off of the film layer, hence, it is more beneficial to deposit this layer on the rear side to minimize the parasitic absorption of the short wavelength light on the front side.[68]

To facilitate the lateral transport of charge carriers towards the contacts, thin films of transparent conductive oxides (TCOs) are typically applied on top of the a-Si:H layers. In SHJ solar cells, various TCOs such as ZnO[69], In_2O_3[70] aluminum-doped zinc oxide (AZO)[71] and indium tin oxide (ITO) have been investigated. At present, ITO is the most commonly utilized TCO in the silicon solar cell industry due to its high transmittance, electrical conductivity, carrier mobility, bandgap, and low refractive index.[72] At an optimal thickness, ITO also serves as an anti-reflection coating on the front side and pairs well with full back metal contacts for back reflection.[73] In addition, it has been reported that ITO, positioned as a layer between the a-Si:H layer and the metal contact, prevents passivation degradation over time in SHJ solar cells.[74, 75] Although front-side ITO possesses anti-reflection properties, it still causes the parasitic absorption of some short-wavelength and near-infrared photons when they hit the solar cell. In some cases, an additional anti-reflection coating like MgF_2 is applied on the front side to form double layer anti-reflection coating (DLARC).[76] Moreover, studies have revealed the occurrence of parasitic plasmonic absorption in the rear-side TCO/metal interfaces, resulting in additional J_{SC} losses.[77] To mitigate this issue, incorporating another interlayer of a low refractive index dielectric material like MgF_2 on the rear side may also prove effective.[68]

To finalize the stacks of a SHJ solar cell, highly conductive and degradation-resistant metallic contacts are deposited on the front and rear side of the cell to ensure the efficient collection of the produced electron-hole pairs. In SHJ solar cells, Ag pastes are favored as the contact material due to their low curing temperature, which is necessary to safeguard the already deposited amorphous layers from temperature-induced degradation.[64] Typically, contact grids comprised of fingers and busbars are screen-printed onto the wafer to finish the cell. On the front side, these grids are ideally kept as thin as possible to minimize reflection losses. On the rear side, contact grids can also be screen-printed to produce bifacial SHJ cells, or Ag can be evaporated entirely on the back to form back reflectors.

2.5. Wafer thickness effect on solar cells

Reducing the thickness of crystalline silicon (c-Si) wafers is key to advancing lightweight and flexible solar modules while minimizing material costs. From the solar cell physics point of view, the thickness of the wafer (W) is a crucial factor that determines the efficiency limit of a crystalline silicon solar cell. The decrease in the thickness of solar cells leads to significant changes in two key parameters that determine their efficiency. In Figure 2.9, a schematic illustrates the effect of wafer thickness on these parameters.

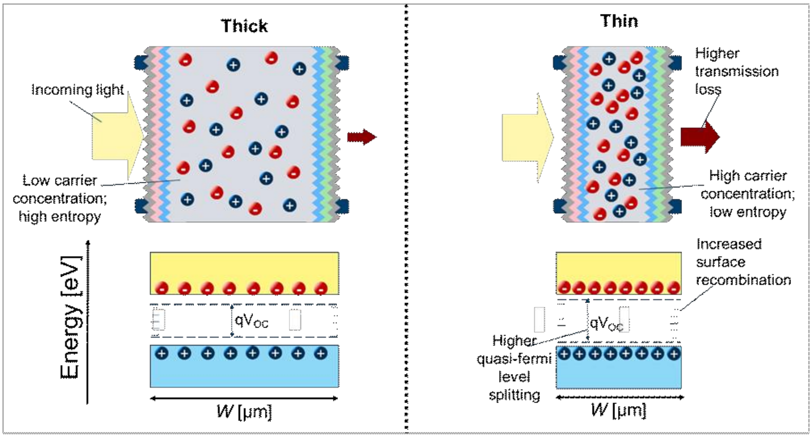

Figure 2.9: Schematic representation of the effect of wafer thickness on carrier concentration, light absorption, quasi-fermi splitting and surface recombination in a solar cell.

Firstly, there is an increase in transmission losses (including front surface escape in the case cells with back reflectors) in thinner wafers which ultimately leads to a reduction in J_{SC}. On the other hand, thinner wafers lead to nearly the same amount of carriers are generated in smaller volume, which has been linked thermodynamically to a decrease in entropy production per photon.[78] The higher concentration charge carries leads increased quasi-Fermi level splitting and ultimately increasing the V_{OC}. However, there is also an increase in surface recombination effect on thinner wafers which negatively affects the overall performance of the cells.

2.6. Fundamental performance limits of crystalline silicon solar cells

The maximum possible efficiency of a solar cell is determined by the intrinsic properties of its material. This can be studied through two primary aspects: generation and recombination. The current-voltage characteristics of a solar cell based only on its intrinsic properties is described by:

$$J = J_L - J_{rec} = J_L - qWR_{intr} \tag{2.33}$$

where J_L is the photogenerated current, J_{rec} is the intrinsic recombination current, q is the elementary charge, W is the thickness of the material and R_{intr} is the intrinsic recombination rate. The photogenerated current, J_L is fundamentally limited by the bandgap E_g and the absorptance A of the material and is expressed as:

$$J_L = q\int_{E_g}^{\infty} \Phi\,(E)A(E)dE \tag{2.34}$$

For theoretical limit calculations, light absorption is typically modeled using Lambertian randomization, which assumes a mean path length of $4n_rW$, where n_r is the refractive index of the solar cell.[79] In more detailed considerations, additional factors such as free-carrier absorption and photon recycling further influence photogeneration.

From the recombination point of view, as discussed in Section 2.3.3, the recombination mechanisms in a solar cell include radiative recombination, Auger recombination, and defect-assisted recombination (both bulk and surface). To calculate the efficiency limit of a solar cell, it is assumed that the material is defect-free and has perfectly passivated surfaces and hence, only intrinsic recombination is considered in the analysis. The intrinsic recombination rate is related to the excess carrier concentration Δn and the intrinsic carrier lifetime τ_{intr} and is defined as:

$$R_{intr} = \frac{\Delta n}{\tau_{intr}} = \Delta n \left(\frac{1}{\tau_{rad}} + \frac{1}{\tau_{Auger}} \right) \tag{2.35}$$

The intrinsic carrier lifetime for radiative τ_{rad} and Auger τ_{Auger} recombination can the calculated using Equations (2.25), (2.27) and (2.28) already discussed in section 2.3.2.

Assuming a narrow base and ideal contacts, the quasi-Fermi level splitting, which is the maximum output voltage, is related to the excess carrier density as:

$$np = (n_0 + \Delta n)(p_0 + \Delta p) = n_i^2 exp \left(\frac{qV}{k_B T} \right) \tag{2.36}$$

For an n-type silicon material, as used in this thesis, the output voltage V can be expressed in terms of the donor concentration N_d as:

$$V = \frac{k_B T}{q} \ln \left(\frac{\Delta n (N_d + \Delta n)}{n_i^2} \right) \tag{2.37}$$

By integrating the appropriate functions in Equation (2.31), the I-V characteristics of a solar cell at the highest achievable performance constrained solely by the intrinsic properties of the material can be determined. From there, the theoretical limits for all solar cell parameters can be extracted.

The limiting efficiency of silicon solar cells has been predicted based on various theoretical studies. The maximum efficiency of single junction solar cells based on the thermodynamic principle detailed balanced studies was first analyzed by Shockley and Queisser in 1961.[80] The Shockley-Queisser model considers the absorption of photons with energy equal to or above the material bandgap, the generation of electron-hole pairs by each absorbed photon, and the collection of all generated charge carriers from the device.[32] In this analysis, theoretical limits are determined only based on the bandgap of the material and radiative recombination. However, in c-Si solar cells, Auger recombination and parasitic free carrier absorption (FCA) contribute considerably to non-radiative intrinsic losses. Taking these losses into consideration, Green [81] and Tiedje [82] further calculated the limiting efficiency specific to c-Si solar cell establishing auger recombination as the limiting factor over radiative recombination. Over the years, new calculations have been reported taking into account factors such as Coulomb-enhanced Auger recombination [83], Coulomb-enhanced radiative recombination [84] and improved parameterizations combining both effects [85] to obtain more accurate predictions on the limiting efficiency of c-Si solar cells.

In the most recent and widely accepted model, Richter et al. [10] calculated the limiting efficiency for c-Si solar cells not only for undoped c-Si but also for n-type and p-type base c-Si at different dopant concentrations and at different wafer thicknesses. Like previous models, this model does not take into consideration the effects of surface and defect-assisted recombination while also assuming perfect anti-reflection on the front side and perfect back reflectors with Lambertian light trapping. The following were considered in the formation of the Richter model:

i) An updated and internationally accepted solar spectrum [86]
ii) Improved optical parameters for undoped c-Si based on experimental data presented by Green [87]
iii) New parameters for free carrier absorption obtained by Rüdiger et al. [88]
iv) Improved parametrization for intrinsic recombination (radiative and Auger) [85]
v) Effect of band gap narrowing (BGN) [89]

Considering n-type wafers (which is studied in this thesis) in the theoretical estimation of Richter et al., a maximum efficiency of 29.43% with an optimal thickness of approximately 110 µm at very low dopant concentration ($<10^{13}$) was reported.[10] In a subsequent work Veith-Wolf et al.[11] built upon the calculations of Richter et al. by conducting a more in-depth analysis of light trapping, even thinner, W = 78.7 µm wafers are expected to achieve the highest efficiency of 29.47% for n-doped c-Si wafers.

Figure 2.10 shows a range of limits for silicon solar cell parameters according to Richter's parameterization.[10] The two solid black lines are the range of wafer resistivities (or dopant concentrations) used in this study. As mentioned in the previous section and shown in Figure 2.10(a), a decrease in wafer thickness results in an increase in the V_{OC} which is attributed mainly to the increase in charge-carrier concentration. Additionally, the impact of dopant concentration on the V_{OC} limit is evident, as an increase in dopant concentration causes a drop in V_{OC} with the effect becoming more pronounced as the wafer thickness increases.

The increase in *FF* with decreasing thickness in Figure 2.10(b) is directly related to a geometric relationship between *FF* and V_{OC} estimated by Green[90] and consequently revised by Leilaeioun et al.[91] as:

$$FF = \frac{v_{OC} - \ln 20}{v_{OC} + v_{OC}/20} \quad (2.38)$$

in which

$$v_{OC} = \frac{V_{OC}}{(n_{id}kT/q)} \quad (2.39)$$

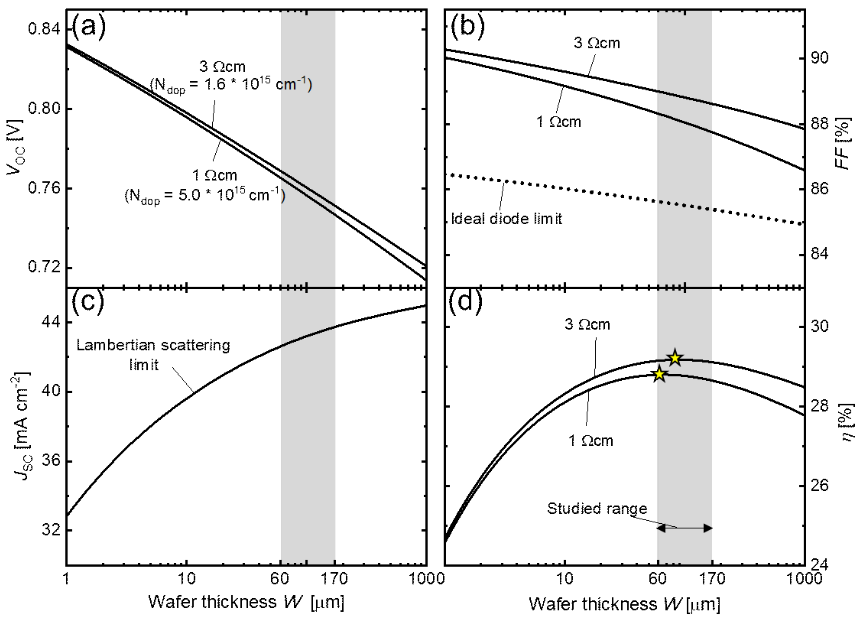

Figure 2.10: (a) open circuit voltage V_{OC}; (b) fill factor *FF*; (c) short-circuit current density J_{SC} and (d) efficiency η plotted with respect to wafter thickness *W* for n-type crystalline silicon solar cells. Solid lines represent the limits calculated by Richter et al. [10]. Dotted line represents fill factor limit at ideality factor n_{id} =1. Shaded area shows studied wafer thickness range (60 – 170 nm) in this thesis. Yellow stars show the maximum theoretical efficiencies for the dopant concentration range in this study.

An important point to note is that at high carrier concentrations where the Auger recombination is dominant, the local ideality factor (n_{id}) of a cell approaches the value of 2/3, thereby resulting in a limit of *FF* that surpasses the usual *FF* of “ideal diode” with n_{id} =

1. The Auger-recombination-limited lifetime leads to exceptional *FF* values in simulations of Richter et al.,[10] Andreani et al.[21] and Kowalczewski et al.[92] which depending on wafer thickness go beyond the expected *FF* value from ideal diode with ideality factor of 1 by 3-4%$_{abs.}$ This potential has been demonstrated experimentally by Yoshikawa et al., where Suns-Voc data show *pFF* of 85.6%[31] which surpasses the predicted 85.4% for an ideal diode at comparable V_{OC} values. In other words, high-quality passivated thin solar cells can operate at the Auger limit even in normal sunlight conditions, which is usually only seen in concentrator devices.[93-95]

The reduction in J_{SC} for thinner wafers, as shown in Figure 2.10(c), is geometrically linked to the assumed Lambertian optical path length of $4n_r W$. Even with optimized light trapping, thinner cells inherently generate lower J_{SC} compared to thicker cells due to their reduced ability to absorb and retain light. Figure 2.10(d) shows that the trade-off between the V_{OC} and the J_{SC} and the slight contribution from *FF* results in a limiting efficiency curve with an optimal thickness that varies based on the dopant concentration of the cell. The maximum theoretical efficiency attainable for the cells in this research is estimated to fall between 28.81% at 63 µm for those with a higher dopant concentration (5 x 10^{15} cm^{-1}) and 29.18% at 83.2 µm for cells with lower dopant concentration (1.6 x 10^{15} cm^{-1}).

In Chapter 4, the influence of wafer thickness on the performance of silicon heterojunction (SHJ) solar cells is investigated experimentally. The study examines the potential and losses in experimental SHJ solar cells fabricated on wafers with thicknesses ranging from 60 µm to 170 µm and compares the results to the theoretical efficiency limits.

2.7. Perovskite/Silicon Tandems

A strategy to exceed the theoretical limit of any single junction solar cell is to use multi-junction tandems that incorporate two or more semiconductor materials with varying bandgaps.[96, 97] To optimize the utilization of the solar spectrum, the top layer of such tandems should be a semiconductor with a higher bandgap that enables the transmission of lower energy photons to the lower bandgap bottom layer, while absorbing high energy photons with minimal loss due to thermalization compared to conventional c-Si solar cells.[33, 98] With a bandgap of 1.12 eV, exceptional stability and electronic properties, crystalline silicon (c-Si) solar cells are a suitable choice for use as the bottom cell in double stack tandem structures.[98, 99] Group III-V semiconductor materials such as GaAs and GaInP have been reported to be promising for the use as the top cell in such tandems due to their wide tunable bandgap and high efficiencies.[100] However, the poor availability and high cost of production of these types of solar cells prevent their use for large scale utilization. An alternative candidate for top cells due to their low manufacturing cost, high absorption in the visible light spectrum and a high open circuit voltage (V_{OC}) is the perovskite solar cell.[101] In addition, with a tunable bandgap between 1.48 and 2.23 eV,[102] there is considerable flexibility to optimize light transmission to the bottom cell effectively. These qualities make the Perovskite/Silicon (Pero-Si) tandem a promising tandem combination in terms of efficiency, cost, and scalability for terawatt production scale.[103-107]

The thickness of Si wafers has been progressively decreasing from 400 µm in 1990[9] to approximately 150 µm at present, and it is expected that the wafer thickness will continue to decrease for at least the next decade.[23, 108] Based on this, it is anticipated that Si-bottom cells for Pero-Si tandems will be fabricated on wafers that are less than 100 µm in thickness in the future. A major concern with thin SHJ solar cells a bottom cell is the transmission loss of some infra-red light, which is more enhanced for thinner cells. In this case, employing light trapping techniques is essential to avoid substantial reductions in J_{SC}. A section of this thesis has been allocated to investigate the consequences of wafer thinning on the functionality of the bottom SHJ cell when it operates under the perovskite-filtered spectrum.

Figure 2.11 shows a schematic of a typical perovskite / silicon heterojunction tandem solar cell showing near infrared light transmitted to the bottom cell and the solar spectrum showing the portion available to the bottom cell. In Pero-Si tandem cells, only the long wavelength portion of the solar spectrum reaches the Si bottom cell. As a result, the losses related to short wavelength light, such as parasitic absorption by the functional layers on the front side of silicon solar cells, are no longer relevant because this portion of the spectrum is already absorbed by the perovskite top cell. From the point of view of SHJ solar cells as the bottom cell, it allows the freedom of optimization of the stacked layers such as the passivation layer, doped layer, and the transparent conductive layer.

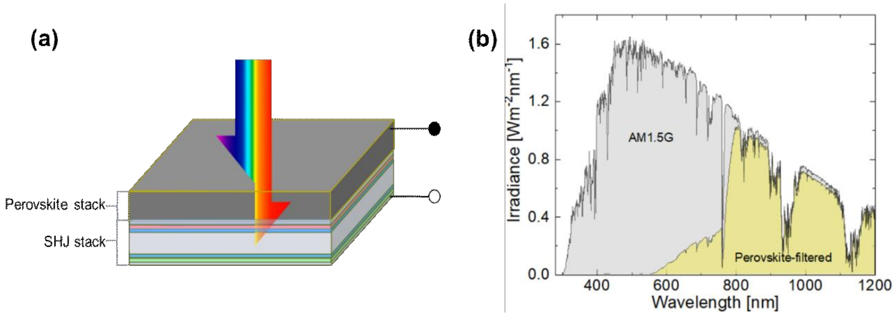

Figure 2.11: (a)Schematic of a typical perovskite / silicon heterojunction tandem solar cell showing near infrared light transmitted to the bottom cell and (b) Solar spectrum showing the portion that travels to the bottom cell calculated from perovskite transmittance data from ref [109].

As previously discussed, one of the significant losses associated with silicon solar cells stems from recombination caused by the cells' imperfect surfaces.[110] The utilization of thicker passivation layers reduces the effects of surface recombination, thereby, increasing both the V_{OC} and FF of the solar cell. Under AM1.5G illumination, concerns about J_{SC} losses due to parasitic absorption and FF losses due to series resistance may emerge. However, under the new spectrum, the front side parasitic absorption is diminished while the resistive losses are reduced due to lower light intensity.[111, 112]

In Chapter 5, a thorough examination of thin SHJ cells as bottom cells in Pero-Si tandem devices is presented. The effect of passivation layer thickness on V_{OC} and FF under the new light spectrum is studied. The analysis takes into account the impacts of spectral effects, light intensity, and the usage of back reflectors to enhance light trapping.

2.8. Thin SHJ solar cells for indoor applications

The increasing demand for self-powered, low-power microelectronic devices, such as sensors, meters, wearables, and actuators for indoor use, is primarily due to the growth of the Internet of Things (IoT).[113-116] It is predicted that approximately 75 billion interconnected wireless devices will be in use by 2025, and using wired power or regular batteries will not be practical.[117] Harnessing energy from indoor ambient lighting using photovoltaic devices is a practical approach for supplying power to wireless electronic devices with low power requirement.

Typical indoor lighting is 300-3,000 times dimmer than direct sunlight, while in some outdoor settings such as nighttime sidewalk lighting, the illumination level can be 30,000 times dimmer than direct sunlight.[114, 118] In contrast to natural sunlight, which approximates a blackbody with a broad emission spectrum, artificial indoor lighting such as light emitting diodes (LED) typically has a narrower spectrum of radiation concentrated in the visible part of the spectrum, as illustrated in Figure 2.12b. Given that c-Si solar cells have a bandgap of 1.1 eV, this means that most of the light emitted by the LED lamp will be absorbed by the solar cell, thus minimizing any losses resulting from thermalization caused by high-energy photons and transmission through the rear of the solar cell.

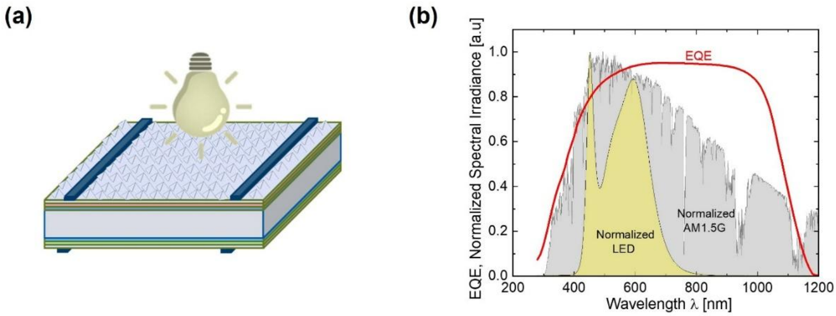

Figure 2.12: (a) Schematic representation of solar cell under LED lighting and (b) External quantum efficiency of a typical c-Si solar cell with normalized AM1.5G and LED spectra .

For a uniform representation of the intensity of artificial lighting such as LED lamps, the intensity is measured in lux, which is the illuminance or the amount of visible light falling on a surface. This unit considers the human eye's sensitivity to the different wavelengths of light. To calculate illuminance in lux, the spectral power density distribution P(λ) for the respective light source is considered. Additionally, the photopic luminous efficiency function *V(λ)*, which represents the relative sensitivity of the human eye to different wavelengths of light under daylight conditions and peaks at 555 nm, is taken into account.[119-121] The luminous flux (φ) in lumens/m^2 or lux can then be determined by integrating the product of P(λ) and V(λ) over the visible spectrum (from 380 nm to 780 nm), using the formular in Equation (2.38):

$$\Phi = 683 \cdot \int_{380\,nm}^{780\,nm} P(\lambda) \cdot V(\lambda)\, d\lambda \qquad (2.40)$$

Here, 683 has a unit of lumens/W and is a constant that represents the maximum luminous efficacy of light at 555 nm.

According to theoretical calculations, the optimum thickness of c-Si solar cells under white LED at 250 lux, which is a typical illumination level of a well-lit office, is 1.8 μm.[118] However, given that such thickness of c-Si is achievable only through expensive bottom-up processes such as epitaxial growth method, it is important to consider the use of practical thin c-Si solar cells produced using the existing mainstream processes. Additionally, ultrathin c-Si wafers tend to be more fragile and prone to breakage, making them less suitable for certain applications. In Chapter 6, a brief experimental study of the effect of wafer thickness ranging between 80 and 170 μm under indoor LED lighting and compared to AM 1.5G is discussed.

2.9. Thin SHJ solar cells for shingle modules

Interconnecting solar cells into modules is an important step toward making photovoltaic devices applicable in practical systems. Of particular interest in this work is the integration of silicon heterojunction (SHJ) mini modules with electrochemical (EC) cells for solar fuel production at the laboratory scale. To enable direct solar-to-fuel conversion, SHJ solar cells must be configured into modules that provide sufficient voltage to drive electrochemical reactions under ambient conditions. These reactions, such as CO_2 reduction and water splitting, typically require operating voltages greater than 1.5 V[122] when considering both thermodynamic requirements and kinetic overpotentials, whereas individual SHJ cells usually provide open-circuit voltages below 0.75 V. This makes it necessary to connect at least three cells in series to meet the voltage demands of electrochemical cells.

Figure 2.13 shows the polarization curve of an artificial leaf device, adapted from recent work, which illustrates the current-voltage characteristics of an electrochemical cell converting carbon dioxide and water into hydrogen and formate.[123] Also shown in the figure are the current–voltage (IV) curves of silicon heterojunction mini modules composed of one to five cells connected in series. The curves show that configurations with only one or two cells do not provide enough voltage to drive the electrochemical reactions, while modules with three or more cells reach the required voltage range for effective operation. This highlights the need to carefully match the voltage output of the photovoltaic module with the operating requirements of the electrochemical cell. The figure also illustrates the importance of coupling efficiency: the closer the maximum power point of the photovoltaic module (indicated by the black dots) is to the operating point of the electrochemical cell (marked by the red dots), the better the coupling factor and the higher the overall system efficiency.

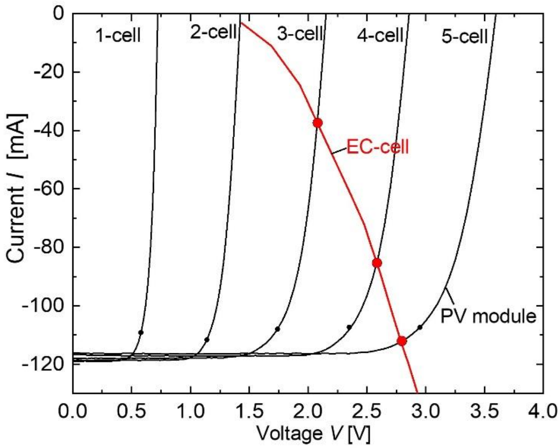

Figure 2.13: Current–voltage characteristics of silicon heterojunction mini-modules consisting of 1 to 5 cells in series (black curves) and the polarization curve of an electrochemical cell (red curve) converting CO_2 and H_2O into hydrogen and formate.[123] The black dots indicate the maximum power points of each photovoltaic configuration, while the red dots represent the corresponding operating points where the PV and EC characteristics intersect.

As discussed in Section 2.5, thin-wafer-based SHJ solar cells typically achieve higher open-circuit voltages than thicker-wafer-based cells, largely due to their increased charge carrier concentration. This difference could be even more significant when cells are connected in series to form a module, as the total V_{OC} is the sum of the V_{OC} values of the individual cells. Thin wafers, with their inherently higher V_{OC}, offer the potential for substantially greater voltage output at the module level compared to modules made with thicker cells. Of particular interest is how the V_{MPP} evolves in these modules, as it directly impacts their operating voltage and overall power conversion efficiency. Exploring this aspect provides valuable insights into the performance potential of thin-wafer modules. As the industry continues to explore thinner wafers for cost reduction and improved performance, understanding how their advantages translate from the cell to the module level could provide valuable insights for advancing photovoltaic designs.

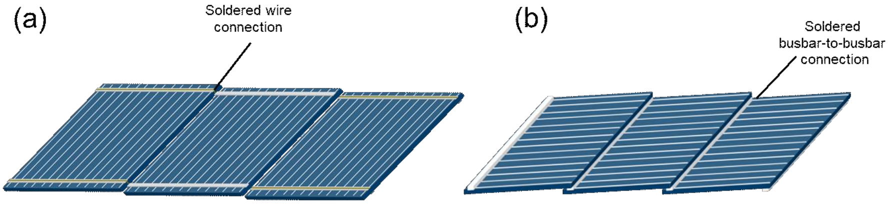

Figure 2.14: Schematic illustration of cell interconnection in (a) conventional solar modules using soldered interconnect ribbons and (b) shingle modules with busbar-to-busbar overlapping cells.

In conventional series-connected solar modules, individual cells are joined together using cell interconnectors. This connection typically involves a wire that is soldered to the busbars and connecting the top and bottom of each cell, collecting the current generated along the busbars as shown in Figure 2.14(a). The shingle modules on the other hand involve a direct soldering of the positive terminal of one cell and the negative terminal of the adjacent cell, eliminating the need for wires, as illustrated in Figure 2.14(b). In this arrangement, the front-side busbar of each cell, which would otherwise cause shading losses and reduce the active area, is positioned along the cell's edge and overlapped by the rear busbar of the neighboring cell. This design removes the inactive spaces and gaps present in conventional modules, allowing the active area of each subsequent cell to fill what would otherwise be unutilized space.[124, 125] In other words, shingle modules have a greater active area, enabling them to achieve higher efficiencies than conventional modules.

In Chapter 7, the evolution of small-scale 80 µm cells into modules is compared with that of thicker 135 µm cells, examining the impact of processes like laser cutting and the performance changes (especially the V_{OC} and the V_{MPP}) as the number of interconnected cells increases. These small-scale modules have been particularly valuable for direct integration with electrochemical cells at the lab scale, where meeting specific voltage requirements is crucial for achieving high solar-to-fuel efficiency.

3. Experimental details

3.1. Silicon Heterojunction Solar Cell Fabrication

In this section, the experimental procedures involved in the fabrication of SHJ solar cells used in this thesis are described, with Figure 3.1 displaying the process flow. Initially, the wafers are thinned, textured, and cleaned using a wetbench process before the deposition of the amorphous intrinsic and doped layers through the Plasma-enhanced chemical vapor deposition (PECVD) technique. Then, ITO layers are sputtered onto the surfaces using a magnetron sputtering device, followed by the screen printing of silver contact grids on both sides of the wafer to produce bifacial cells. Although the cell fabrication process typically ends at this stage, in Chapter 5, further steps are taken to improve light trapping within the cells. For instance, the electron beam evaporation method is employed to deposit MgF_2 on the front side, acting as an anti-reflection layer, and on the rear side to support back reflection with the full back Ag, which is also done using the magnetron sputtering process.

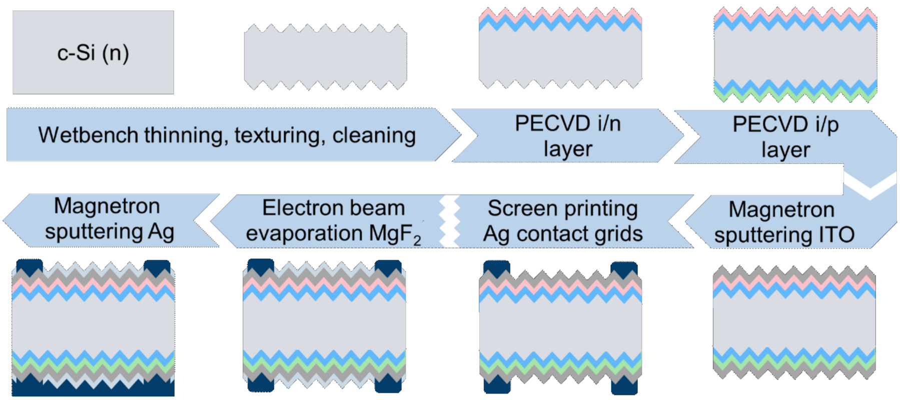

Figure 3.1: Process flow for the fabrication of silicon heterojunction solar cells

Experimental details

Wetbench Process

The initial stage in the preparation of wafers prior to deposition is the wetbench process. For the purposes of this thesis, monocrystalline Czochralski-grown M2 and M2+ n-type ⟨100⟩ silicon wafers with resistivities ranging from 1 to 3 Ωcm, procured from LONGi, were utilized. The wetbench process entails three primary steps: thinning, texturing, and cleaning of the Si wafers. Following each step, the wafers are rinsed with deionized water using a quick dump rinser (QDR) and left to air dry. Initially, the wafers are thinned using a saw damage removal (SDR) process, which entails immersing them in a dilute KOH solution. To achieve wafers of varying thicknesses, the SDR time was adjusted. The etching rate during the thinning process was assessed by analyzing the weight loss of the wafers. During the development stage of the wafer thinning experiment (which is not included in this thesis), three methods were employed to measure the wafer thickness: calculating it from the wafer weight, using cross-sectional scanning electron microscopy (SEM), and measuring it mechanically at the LOANA solar simulator. The uniformity of wafer etching was determined using cross-sectional SEM. The thinning process appeared to be highly uniform, with a variation in thickness of only 2 µm for the thinnest wafers. Following calibration, the thickness of the wafer was routinely estimated by calculating it from the wafer weight. After thinning, the wafers are textured using anisotropic etching with dilute KOH and an additive called cellTex ultraTN from ICB GmbH & Co. KG. Next, the wafers were treated in a solution of dilute HCl with ozone gas. Finally, the wafers are cleaned in a mixture of HF, HCl, O_3, and H_2O, rinsed, and left to dry. Ideally, the wafers are then immediately transferred to the PECVD system for the thin film depositions to prevent formation of oxide films on the wafer surfaces.

Plasma-enhanced chemical vapour deposition

Plasma-Enhanced chemical vapor deposition (PECVD) is a commonly utilized method for producing high-quality, thin films on substrates at a lower temperature than traditional chemical vapor deposition (CVD) processes. The PECVD generally entails injecting a mixture of precursor gases into a vacuum chamber with a substrate present. Then, using a radio frequency generator is utilized to ignite plasma in the gas mixture, which breaks down the precursor molecules into reactive components. These species can then interact and settle on the substrate to create a film.[126] Figure 3.2 shows a schematic representation of the AK 1000 Inline PECVD device used for this thesis.

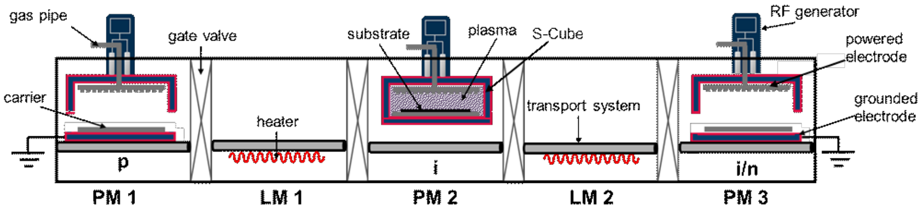

Figure 3.2: Schematic top view of the AK 1000 Inline PECVD system

The PECVD device consists of five chambers which includes three process modules (PM 1, PM 2 and PM 3) and two loading modules (LM 1 and LM 2). The substrates are loaded and unloaded in and out of the device through LM 1 and LM 2. Each chamber has the capacity of depositing on nine M2 size wafers at a time. In the process chambers, the process gases are introduced through a gas pipe and the gas distribution is integrated with the upper electrode which is powered by the radio frequency generator. The substrates are placed in the lower electrode which is grounded. Both electrodes are maintained at a temperature of 200 °C. To facilitate the plasma process, the substrate electrode is raised and brought into contact with the upper chamber, creating a separate plasma discharge chamber called the S-Cube as shown in PM 2.[127] This chamber is evacuated by a separate backing pump, while the vacuum pressure is regulated by a butterfly valve.

The solar cells used in this thesis employ wafers that undergo the following process. Initially, the wafers are loaded onto LM 2 and transported to PM 3, where intrinsic and n-doped a-Si:H are deposited sequentially. Following this, the wafers are returned to LM 2, flipped, and then transported to PM 2 for the deposition of the rear-side i-layer. Lastly, the wafers are transported to PM1 via LM 1, where p-doped a-Si:H is deposited. The process gases for the intrinsic a-Si:H layer are hydrogen (H_2) and silane (SiH_4). To achieve the n-doped and p-doped layers, phosphine (PH_3) and diborane (B_2H_6) are admixed to the intrinsic gases respectively.

Experimental details

Magnetron sputtering

Magnetron sputtering is a deposition technique that utilizes a gaseous plasma, generated and confined near a solid target containing the material to be deposited. The plasma's energetic ions erode the target's surface, causing the emission of atoms that travel and settle on a substrate to form a thin film. During the standard procedure of sputtering deposition, the chamber is initially evacuated to a high vacuum state for the purpose of minimizing the partial pressures of all background gases and possible impurities. Upon attaining the base pressure, an inert gas like argon is introduced into the chamber, and a pressure control system is employed to sustain the overall pressure.[128]

The cathode is typically situated directly behind the target while the anode is connected to the chamber and serves as electrical ground. To generate plasma, a high voltage is applied between the cathode and the anode and this results in the acceleration of electrons away from the cathode. These electrons then collide with the atoms of the sputtering gas and result in an electrostatic repulsion which displaces electrons from their atom, thereby ionizing the sputtering gas. The positively charged ions in the plasma are then attracted to the negatively charged target at a high velocity, leading to the erosion of the target surface and the release of atoms. Consequently, the liberated atoms with sufficient kinetic energy travel and settle on a substrate to create a thin film. To enclose the electrons within the plasma, a strong magnetic field is utilized during the sputtering process.[128]

For the purposes of this thesis, the magnetron sputtering process was used in the deposition of ITO and the full back Ag contact. The ITO films were deposited using a cylindrical target composed of 97:3 wt.% In_2O_3:SnO_2 target with a substrate temperature of 200 ^{o}C while 100% Ag target was used to sputter the full back Ag contact at 25 ^{o}C.

Screen printing

The most common method for applying metal contacts onto the surface of c-Si solar cells is the screen printing process.[129] This technique involves using a patterned or screen to print a metal paste, in this case, Ag, onto the c-Si wafer. The screen comprises a structured emulsion mask layer on top of a finely woven steel mesh that has been stretched and secured by a metal frame. The emulsion mask layer is structured in a way that creates the desired contact pattern on the solar cells through the openings.[130]

To initiate the process, the wafer is placed on the printing table and secured in place. The screen is positioned directly above the wafer, and the paste is applied onto the screen using a flood blade, which fills the mesh evenly. A squeegee is used to press paste through the open areas of the mesh screen, which results in the pattern of the mesh being transferred onto the sample. To achieve low lateral grid resistance without additional shadowing, the cell's front side undergoes a double print which increases finger height. Figure 3.3 shows the screen printing designs used in this thesis. Following the screen printing process, the cells are typically dried for 10 minutes at 150 °C. Subsequently, cells with Design A were annealed at 170 °C for 40 minutes, while the Design B cells for mini modules were annealed at 200 °C. The higher annealing temperature for the latter cells is to ensure better adhesion of the Ag paste, which allows for firm soldering of the shingle cells. After the annealing process, the cells are allowed to cool down and then flipped for printing on the other side.

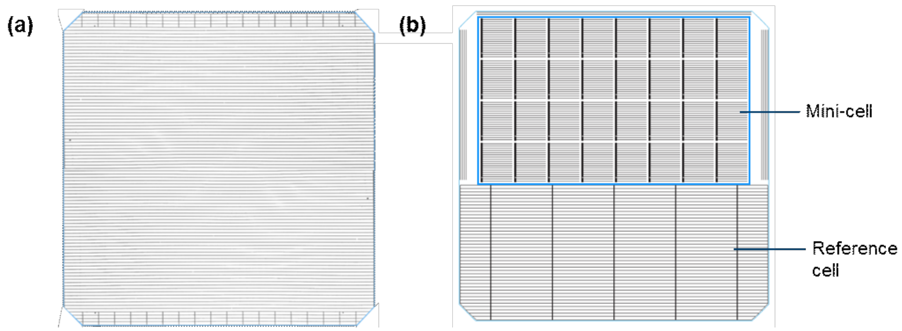

Figure 3.3: Screen-printed front-side metallization layouts for (a) Design A: full-size SHJ solar cells and (b) Design B: segmented mini-cell layout designed for shingle module integration.

The reference cell in Design B was employed for single cell studies in Chapter 4 while the minicells were used for tilt angle, indoor LED (Chapter 6) and minimodules studies (Chapter 7). The Design A was used for the studies of SHJ solar cells for Pero-Si tandem applications in Chapter 5. The minicell design consists of 32 mini cells which are cut using the laser cutter and then soldered to produce shingle cells. More information on this will be discussed in Section 3.2. The reference area consisting of 5 busbars is used as a reference to the mini cells to estimate the losses involved in the laser cutting process.

Electron beam evaporation

Electron beam evaporation is a technique for physical vapor deposition that involves the bombardment of a target material with an electron beam generated by an electron gun consisting of charged tungsten filament in a high vacuum chamber. When this occurs, the atoms from the target material vaporize and then form a precipitate that coats everything in the vacuum chamber, including the substrate material forming a thin film.[131] In this thesis, electron beam evaporation was applied to deposit magnesium fluoride (MgF_2) layer on both sides of already screen-printed cells to act as an anti-reflection coating (ARC) and support layer for back reflection. To prevent any negative impact on the cell's electrical properties, the metal contacts at the sides of the cell are covered during the deposition process, thus ensuring that the MgF_2 does not have any adverse effect on the cell's performance.

Light soaking technique

Light soaking in solar cells involves exposing the cell to prolonged, continuous illumination to enhance or stabilize its performance. In SHJ solar cells, light soaking is used to enhance passivation at the silicon interface and boost carrier transport properties. The process is split into two effects: heating effect and light effect. The heating effect works on improving the conductivity of the TCO layer while the light effect works on improving the passivation quality of the amorphous silicon layers. More detailed discussion on this process can be found in Ref. [132].

The light soaking system is made up of a chamber containing a heating table that can contain 4 M2 cells per batch. An automatic rail system is used to position and move the cells to the preheated chamber. To maintain good thermal contact, the cells are suctioned firmly on the table using a vacuum pump connected to the heating table. The process temperature is set and can be synchronized over the illumination and the heating table by air circulation. To maintain a consistent temperature on the cells throughout the process, a pyrometer is utilized to monitor the cells' temperature. An LED panel is used as a light source and to prevent overheating of the LED, a water cooler is used to maintain its temperature below 30 °C. The chamber walls are mounted with mirrors to prevent scattering losses. For the purposes of this thesis, after screen printing and the Ag full-back sputtering, the cells were treated to a simultaneous light-soaking and annealing process at an intensity of 55 kW/m^2 and at a temperature of 190 ^oC for 90 seconds. The effects of this process on the performance of the solar cells can be found in Chapter 5.

3.2. Minimodule Fabrication

To produce minimodules, the cells with the screen-printing design shown in Figure 3.3(b) are cut using a picosecond laser cutting machine. Thereafter, the individual cells are characterized and the cells with similar electrical properties are soldered together using adhesive solder paste to form shingle modules. In this section, the fabrication processes of the shingle modules are discussed.

Laser-Cutting Process

In this work, the Ultrashort Pulse InnoSlab Laser from the PX series by Edgewave was used. This laser operates at a wavelength of 532 nm. Several parameters are important in optimizing the laser-cutting process, namely, the percentage power, pulse-repetition frequency, cutting speed and the number of repetitions. The power which governs the intensity of the laser beam is determined by the total optical energy produced per second. The pulse-repetition frequency (f_{pulse}) is the number of pulses per second that hit the sample's surface, and it is controlled by adjusting the frequency at which a gate - which can allow or block the laser - is opened and closed. The cutting speed (ν) measures how fast the laser moves across the surface of the solar cell while the number of repetitions (n) is how many times the laser beam passes over the same spot. All these parameters affect the cutting depth and the smoothness of the edges of the cut cells. The effect of these parameters on cutting 80 µm and 135 µm cells are discussed in Chapter 7.

Shingle modules preparation

The soldering process of silicon mini shingle modules produced in this thesis uses a low-temperature solder alloy composed of Tin, Bismuth, and Silver (Sn42Bi57Ag1). This solder melts and facilitates bonding at a temperature range of 160°C to 180°C. The low soldering temperature is particularly important for silicon heterojunction cells, which require low-temperature processes to preserve the amorphous silicon layers. For the busbar-to-busbar interconnection, the paste was applied only to the front side of each silicon cell and placed in the soldering machine. The next cell was then carefully positioned so that its rear busbar connected precisely with the front busbar of the previous cell, which had already been coated with the paste.

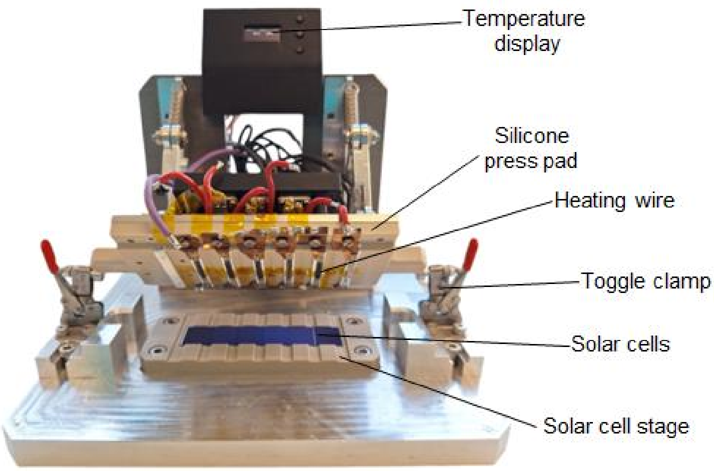

Figure 3.4: Custom-designed soldering machine used for producing shingle mini-modules, featuring temperature-controlled heating elements, silicone press pad, and toggle clamps for precise alignment and secure interconnection of overlapping solar cells.

The soldering machine was designed for precise alignment and controlled heating, as shown in Figure 3.4. Its lower stage consists of a silicone cell holder, which aligns the rear busbar of one cell perfectly with the front busbar of the adjacent cell. The upper part features a silicone pressing pad with embedded heating wires, positioned to apply heat exclusively to the busbar area. A toggle clamp secures the upper press pad to the lower stage, maintaining alignment and consistent pressure during soldering. To supply heat to the soldering machine, a DC power supply was used. The soldering current was gradually increased until the temperature of the heating wires reached about 180°C to 200°C. This temperature was then maintained for about 20 seconds to ensure the heat transfer between the cells was sufficient to melt the solder paste and create a strong, reliable joint between the cells.

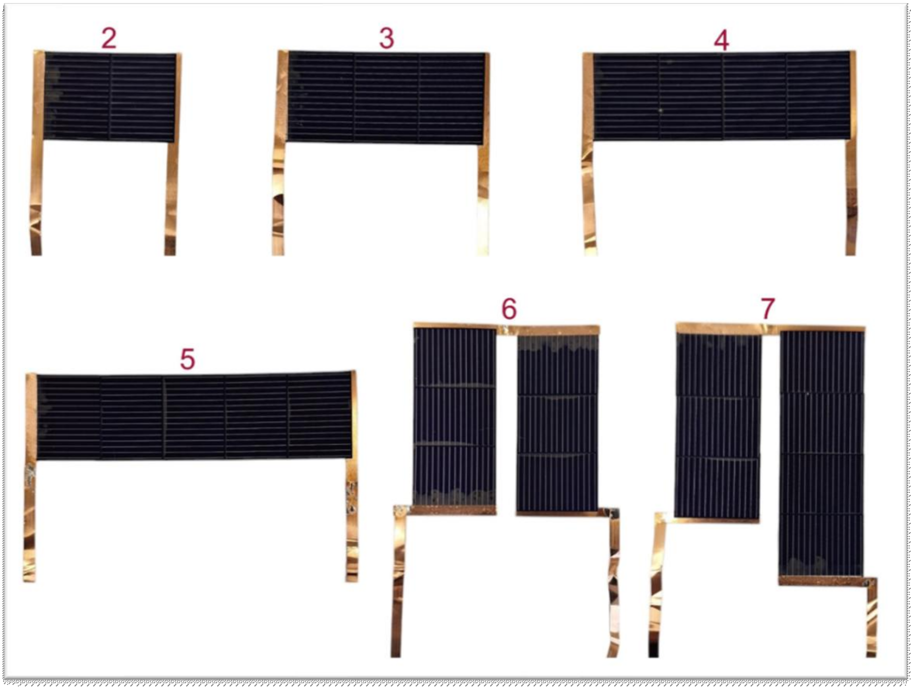

Figure 3.5: Images of representative modules showing the 2-, 3-, 4-, 5-, 6-, 7- cell modules configurations produced.

Using this method, 2-, 3-, 4-, 5-, 6-, 7- cell modules of 80 and 135 µm thicknesses were prepared. The copper wires were soldered separately to the front busbar of the outermost cell and the rear busbar to the innermost cell to enable external connections. The 6-cell modules were created by soldering two 3-cell modules together in series using copper wires, while the 7-cell modules were formed by connecting one 3-cell module and one 4-cell module in series. This configuration was used to reduce the effect of light inhomogeneity, which is more pronounced away from the center of the solar simulator stage, during measurements. Figure 3.5 shows the representative cells of all configurations used in this thesis.

3.3. Solar Cell and Module Characterization

Photoconductance Measurement

Photoconductance lifetime tester WCT 120 by Sinton Instruments is a widely accepted tool for assessing the quality of crystalline silicon wafers used in solar cell manufacturing. By evaluating the charge carrier dynamics of silicon solar cells early in the production process, the device offers valuable insights into the potential efficiency of solar cells. During a measurement, the Si wafer is placed on a stage with an induction coil embedded underneath, which generates a radio-frequency electromagnetic field coupled to the wafer. An infrared light pulse generates excess charge carriers (Δn) within the wafer and the recombination of these carriers causes a decay in photoconductance which is detected by the device.

The Sinton WC-120 system offers two primary measurement modes: quasi-steady-state and transient. In the quasi-steady-state mode, the sample is exposed to a prolonged light pulse, ensuring that the excess minority carrier density remains nearly constant over time. Under these conditions, the generation and recombination rates are equal. In quasi-steady-state conditions, the generation rate is equal to the recombination rate, and hence, Equation (2.4) in Section 2.2.2 becomes

$$\tau_{eff} = \frac{\Delta n}{G(t)} \tag{3.1}$$

For accurate quasi-steady-state measurements, the flash lamp's decay constant must be at least ten times longer than the excess minority carrier lifetime. Therefore, this method is restricted to samples with τ_{eff} less than 200 µs and is not suitable for the high-quality Si wafers used in this thesis.

In this thesis, the transient method which allows for wafer with τ_{eff} greater than 200 µs was used to obtain the effective lifetime. In this case, $G(t) = 0$ since the decay recorded occurs after the flash has been turned off and the system is no longer in steady state. Hence, Equation (2.4) reduces to

$$\tau_{eff} = \frac{-\Delta n}{\frac{d(\Delta n)}{dt}} \tag{3.2}$$

From the measured lifetime and excess carrier concentration, additional relevant parameters, including the surface recombination velocity and implied I-V characteristics, were extracted using the relevant relations described in Section 2.2.2.

Current density – Voltage (JV) Characteristics

In this thesis, two different solar simulators were used for characterizing the solar cells due to considerations of simulator compatibility with the size and contacts of the solar cells. For the cells discussed in Chapters 4 and 5, respectively, the LOANA solar cell analysis system from PV-Tools GmbH with a Wavelabs Sinus 220 light source was utilized. To analyze the mini cells and shingle modules under both indoor LED and AM1.5G conditions discussed in Chapters 6 and 7, a solar simulator manufactured by Wacom (SunSim2) was utilized.

Using the LOANA solar simulator, three distinct modes of current-voltage (JV) measurements were employed—dark-*JV*, J_{SC}-V_{OC}, and light-*JV*—each tailored to analyze specific parameters of silicon heterojunction (SHJ) solar cells. Dark-*JV* measurements were conducted to determine the shunt resistance (R_{SH}) in the absence of illumination and to derive information about the two saturation currents (J_{01} and J_{02}). This mode is crucial for understanding the diode characteristics and leakage currents of the solar cells, providing insight into the intrinsic electrical behavior without the influence of photo-generated carriers. J_{SC}-V_{OC} measurements were performed at varying light intensities to obtain the short-circuit current (J_{SC}) and open-circuit voltage (V_{OC}) values, which were subsequently plotted to generate a *JV* curve. This method leverages the fact that V_{OC} and J_{SC} are not influenced by series resistance (R_S) at values less than 10 Ωcm^2.[133] Consequently, the J_{SC}-V_{OC} mode is instrumental in determining the pseudo-fill factor (*pFF*) of the V_{OC} solar cell. The pseudo-fill factor represents the fill factor (*FF*) the cell would exhibit if series resistance effects were negligible. Light-*JV* measurements were utilized to evaluate key performance parameters of the solar cells under standard illumination conditions. This mode allows for the direct determination of J_{SC}, V_{OC}, *FF*, and overall cell efficiency (η). The light-*JV* characteristics reflect the real-world operational performance of the solar cells, incorporating the effects of both series and shunt resistances, and providing a comprehensive assessment of the cell's efficiency.

To investigate the performance of SHJ solar cells as bottom cells in perovskite-silicon tandem configurations, a custom light setup was developed to replicate the spectral conditions experienced by the bottom cell. This was achieved by generating a perovskite-filtered spectrum based on semi-transparent perovskite transmission data from Zhang et al.[109]. The transmission data was modified to a consistent 95% transmission rate between 800 nm and 1200 nm as shown in Figure 3.6. This adjusted transmittance spectrum was then multiplied by global irradiance values corresponding to each wavelength of light. The resulting spectrum was then reprogrammed into the LOANA system by finely tuning the intensity of LEDs emitting light at different wavelengths, ensuring that the emitted spectrum replicated the desired perovskite transmission profile.

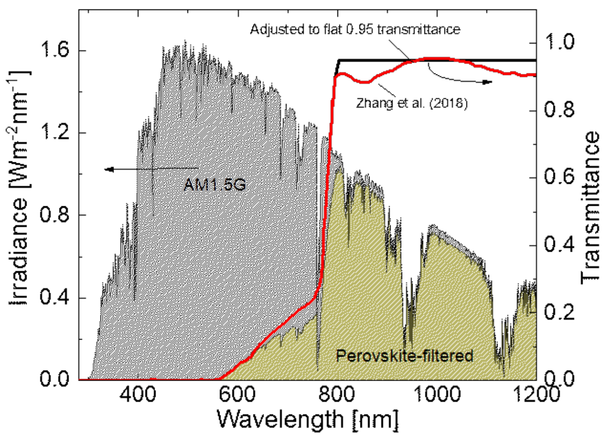

Figure 3.6: Perovskite-filtered spectrum obtained as a product of the solar spectrum and the transmittance of perovskite solar cell reported by Zhang et al.[109] and adjusted to 95% transmittance from 800 nm to 1200 nm

The mini cell and shingle modules used in Chapters 6 and 7 were tested under AM1.5G solar illumination using a class-A sun simulator manufactured by Wacom, which utilized a combination of xenon and halogen light sources. For the LED indoor tests, the experimental setup remained similar, except that the light source was replaced with an Osram 5.5W LED spotlight emitting "cool white" light at 4000 K. This light source was positioned at a calibrated 20 cm away from the sample stage. Prior to each measurement session, the intensity and spectral characteristics of the LED were carefully measured using a spectral analyzer. Each measurement began at least 15 minutes after turning on the LED bulb to ensure stable operation and reliable, consistent results throughout the testing process. For measurements at different light intensities, neutral density filters sized 20 × 20 cm were used.

Quantum Efficiency and Reflectance

In this thesis, two different systems were used to measure the external quantum efficiency EQE and reflectance R of the cells due to size and contact compatibility. For the cells used in Chapter 5, the LOANA system from PV-Tools GmbH was used while the Grating Monochromator Quantum Efficiency (GM.QE) setup for the single cell modules measured in Chapter 6. Before measuring the cells, a reference photodetector with a known spectral response is used to calibrate the system. This step ensures that the light intensity at each wavelength is accurately known. During measurements the solar cells are set under short-circuit conditions and illuminated. Using a diffraction grating monochromator, the wavelength of the incident light is varied. A bias light, which simulates the intensity of light at 1-sun is used which allows the solar cell to maintain a consistent electrical response throughout the measurement. The monochromator alternates between illuminating the solar cell with monochromatic light and interrupting it with the brighter bias light. This modulation allows the system to distinguish between the current generated specifically by the monochromatic light and any background or baseline current produced under steady-state conditions with the bias light.

Photoluminescence

Photoluminescence (PL) is a powerful, non-invasive technique that enables the detection of specific impurities in semiconductors and offers spatially resolved insights into the quality of solar cells. Since it does not require physical contact or cell encapsulation, PL can be applied throughout various stages of the solar cell fabrication process. In this method, the sample is illuminated with a light source which is typically a laser with photon energy exceeding the material's band gap. This excitation generates excess electron-hole pairs, which can recombine either radiatively or non-radiatively. The radiative recombination of these carriers results in the emission of photons, primarily in the near-infrared for crystalline silicon. The resulting PL image typically appears as a grayscale or false-color intensity map, where bright regions indicate high radiative recombination corresponding to areas with longer minority carrier lifetimes and better material quality. In contrast, darker regions represent non-radiative recombination sites such as surface damage, impurities, or processing defects. For instance, darkened edges in the image may signal increased edge recombination due to laser cutting damage or poor passivation.

For the PL experiments in this work, a Princeton Instruments NIRvana 640 InGaAs camera was used to detect near-infrared luminescence emitted by the solar cells. The camera was fitted with a 1050 nm band-pass filter with a full width at half maximum (FWHM) of 30 nm to effectively block scattered light from the 808 nm excitation laser. An integration time of 10 milliseconds was used to collect sufficient signal while avoiding saturation. To enhance image quality, a background image captured under identical conditions without illumination was subtracted from each measurement. This ensured the removal of thermal and sensor noise from the final PL images.

4. Wafer Thickness Effect on SHJ Solar Cells

In this chapter, the experimental results on the impact of wafer thickness on the performance of SHJ solar cells are discussed. Here, several SHJ solar cells of thicknesses ranging from 60 to 170 µm were prepared as discussed in the previous chapter. To isolate and identify losses, the solar cells were investigated at different stages of preparation. In the first section of this chapter, the lifetime studies of the sample wafers after passivation layer deposition but before ITO deposition were discussed. In the next section, the study's focus was on analyzing and comparing the impact of wafer thickness on the solar cell parameters before and after the metallization process. Specifically, the study examined the gains and losses associated with different wafer thicknesses. Finally, the performance of representative cells of different thicknesses at different tilt angles was discussed. This investigation sheds light on how wafer thickness and orientation relative to sunlight affects the performance of the solar cells. Some of the results presented in this chapter have been published in ref.[134]

4.1. Effect of wafer thickness on excess carrier lifetime

Figure 4.1 shows a plot of the effective carrier lifetime, τ_{eff} against the excess carrier density, Δn reconstructed from lifetime measurements. The colored lines represent the lifetime curves for representative Si wafers of 80, 100, 130 and 170 µm thickness with resistivity of approximately 1 Ωcm. The white dots labelled "MPP" represent the τ_{eff} and Δn points where the implied power from the implied *JV* curve generated from the measurement is maximum while the white dots labelled "iV_{OC}" represent the τ_{eff} and Δn points where the iV_{OC} is at 1 sun. The dashed lines represent the Auger lifetime limit curves based on models by Kerr-Cuevas [12], Richter [85], and Veith-Wolf [11]. From the plot, the influence of surface recombination is clearly visible at low injection levels as τ_{eff} reduces with decreased thickness for a broad range of the excess carrier density, Δn, which is most pronounced at Δn below 5×10^{15} cm^{-3}. At low injection levels, τ_{eff} is limited by SRH recombination mostly at the surfaces. With the reduction of wafer thickness, the surface recombination gains significance and thereby reducing τ_{eff} as the volume of the Si bulk is reduced and imperfect surfaces get closer to each other. At higher injection conditions (Δn > 10^{16} cm^{-3}), the effect of Auger recombination takes over and the influence of the wafer thickness becomes less significant.

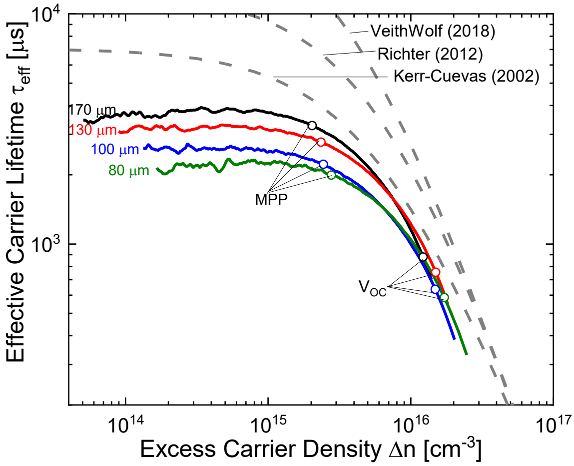

Figure 4.1: Effective carrier lifetime τ_{eff} vs excess carrier density Δn at different thicknesses (80 – 170 μm with measured resistivity approximately 1 Ωcm. The dashed lines represent the Auger lifetime limit from different models at 1 Ωcm.[11, 12, 85]

Using the PV lighthouse recombination calculator,[135] simulations of the Auger-limited lifetime were performed using the bandgap narrowing parametrization by Schenk,[89] dopant ionization model by Altermatt et al.,[136] and radiative recombination model by Trupke et al.[137] The results of simulations also presented in Figure 4.1 for models by Kerr-Cuevas,[12] Richter[85] and Veith-Wolf.[11] show that the experimental lifetime is well below the Auger limit at low carrier density where SRH recombination dominates. The simulated values of the τ_{eff} approaches the experimental values at higher carrier density, however there are still noticeable differences in values and slopes between the experimental data and simulation. The current device apparently requires a more detailed modelling to account for the carrier density distribution. In all four lifetime curves, the points of the one-sun implied V_{OC} are deep in the "Auger regime" – the high carrier density region where Auger recombination plays a dominating role. Here, it is expected that the theoretical predictions[10-12, 21, 85, 92] based on Auger recombination limit are most relevant for the experimental data. At the same time, it can be seen in Figure 4.1 that the implied *FF* (MPP) points of all thicknesses are deep in the carrier density range dominated by SRH recombination, therefore, the predictions made with Auger limit are less relevant for the fill factor. In other words, the implied V_{OC} in high quality SHJ solar cell precursors is very close to the fundamental Auger limit while the *iFF* is to a large extent limited by the quality of the wafer passivation.

An alternative way to present the transition between SRH and Auger recombination regimes is to calculate the differential ideality factor n_{id}^{diff} using Equation (2.25). Figure 4.2 presents the differential ideality factor from both experimental measurements and simulations, enabling a direct comparison between the two. The simulation was performed by calculating the implied open-circuit voltage iV_{OC} and corresponding n_{id}^{diff} as a function of generation rate, using the approach described in Section 2.3.2. To ensure meaningful comparison with the measured data, the effective minority carrier lifetime used in the simulation for each wafer thickness was matched to the corresponding measured effective lifetime, namely τ_{eff}= 3.7 ms for the 170 µm wafer and τ_{eff} = 2.2 ms for the 80 µm wafer. The simulation also assumed a wafer dopant concentration N_D of 1.56 x 10^{15} cm^{-3}, corresponding to the base doping level of the wafers used in this study. The Auger recombination coefficients, C_n and C_p were adopted from the empirical parameterization by Black and Macdonald[138]. The key input parameters utilized in the simulation are summarized in Table 4.1.

Although the simulated curves in Figure 4.2 do not align quantitatively with the measured data, they capture the general shape and the transitions in recombination behavior across different injection levels. The mismatch likely results from the simplified assumptions made in the simulation, such as treating the wafer as a uniformly doped bulk with constant lifetime and not including the layered structure of the actual SHJ precursors. Still, the simulation offers meaningful qualitative insights. One noticeable feature is the systematic shift in iV_{OC} between the different wafer thicknesses, both in the measured and simulated data. This shift is a direct consequence of the wafer thickness effect: thinner wafers exhibit higher iV_{OC}, as their reduced volume results in higher excess carrier density and larger quasi-Fermi level splitting at a given illumination level.

Table 4.1: Simulation parameters used for modeling differential ideality factor

Parameter	**Value**
C_n	1.56×10^{-30} cm^6s^{-1} [138]
C_p	5.54×10^{-31} cm^6s^{-1} [138]
N_D	1.6×10^{15} cm^{-3}
$\tau_{n,p}$ (170 µm)	3.7 ms
$\tau_{n,p}$ (80 µm)	2.2 ms

At lower injection levels, n_{id}^{diff} from measured data exhibit significant scatter and noise compared to the smooth simulated curves. This is a well-known limitation of the QSSPC-based differential ideality factor extraction. At low injection, the signal-to-noise ratio in photoconductance measurements deteriorates due to the low excess carrier concentration, resulting in greater measurement uncertainty.[139] In addition, the numerical derivative $\frac{\mathrm{d}iV_{OC}}{\mathrm{d}ln(\varphi)}$ becomes highly sensitive to small fluctuations in the signal, further amplifying noise in n_{id}^{diff} under these conditions.

In the SRH-dominated regime, the simulated n_{id}^{diff} curves show slightly higher values compared to the experimental data. As mentioned earlier, one possible explanation for this discrepancy is the difference in material structure between the simulated and actual wafers. The simulations are based on single-crystalline wafers with uniform doping, whereas the SHJ precursors used in the measurements include both passivated and doped layers (intrinsic and doped a-Si:H layers).

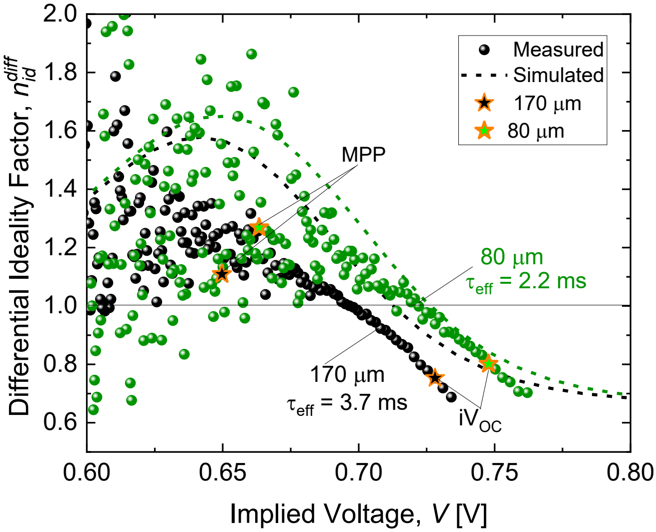

Figure 4.2: Measured and simulated differential ideality factor, n_{id}^{diff} as a function of voltage, V for 80 µm and 170 µm wafers, indicating the maximum power point and open circuit voltage.

At high injection levels, where Auger recombination dominates, the simulated n_{id}^{diff} curves show the expected convergence toward a universal trend, driven solely by intrinsic Auger recombination, which depends only on the carrier density. In contrast, the experimental curves for different wafer thicknesses do not fully converge to the same dependence at high voltage. This indicates that in practical SHJ precursors, additional effects beyond intrinsic Auger recombination are present.

Regarding the positions of key operating points, the region near the iV_{OC} at 1 sun typically around 0.73–0.76 V for these wafers, corresponds to the high injection Auger-dominated regime, where the measured n_{id}^{diff} values remain below 1. In contrast, the implied fill factor (MPP) region lies at intermediate voltages where measured n_{id}^{diff} is in the range of approximately 1.2–1.4, consistent with a regime still influenced by SRH recombination. The presence of SRH recombination near the MPP highlights that in practical SHJ devices, the fill factor remains limited by recombination processes beyond the fundamental Auger limit.

These observations confirm that while Auger recombination dominates at high injection, the real device behavior is influenced by additional factors not captured in simple Auger-limited models. Zero-dimensional predictions of the Auger limit are therefore insufficient to fully describe the realistic behavior of SHJ devices. Further work is needed to incorporate these effects into more advanced modeling approaches in order to better understand and approach the practical performance limits of SHJ solar cells.

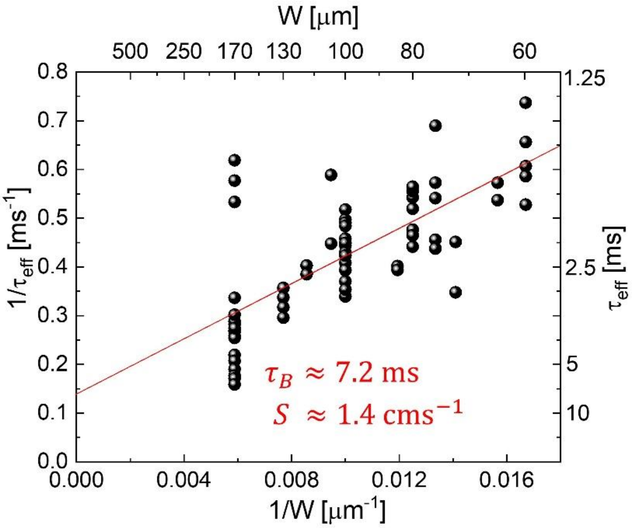

Figure 4.3: Inverse effective lifetime vs inverse wafer thickness. The bulk lifetime and the surface recombination velocity, S are determined from the intercept on $1/\,\tau_{eff}$ axis and the slope of the fitted red line, respectively.

To determine the contributions of bulk and surface recombination in the cells, the inverse effective lifetime $1/\tau_{eff}$ was plotted against the inverse wafer thickness $1/W$, as illustrated in Figure 4.3 and described by relationship described in Equation (2.5). The actual wafer thickness is displayed on the top x-axis for easier data interpretation. The effective lifetime values utilized for this plot are representative of τ_{eff} values at excess carrier density, Δn of 1×10^{15} cm^{-3}. The plot shows a significant scatter in lifetime for each given wafer thickness which indicates some variability in the bulk wafer quality. However, it is evident that a decrease in wafer thickness leads to a decrease in the effective lifetime of the wafer. With a linear fit to the data presented, a bulk lifetime τ_B of approximately 7.2 ms and a surface recombination velocity S of approximately 1.4 cm s^{-1} were determined from the intercept on $1/\tau_{eff}$ axis and the slope of the fitted red line, respectively. Considering that the bulk lifetime is a factor of 2-3 higher than the total effective lifetime, it can be concluded that at the injection level which is near the maximum power point as demonstrated in Figure 4.1, the recombination in SHJ solar cells is dominated by surface SRH recombination.

So far, the analysis was based on photoconductance lifetime measurements on the solar cell precursors. The following section explores the development of solar cell parameters at key preparation stages all the way up to the final solar cell.

4.2. Effect of wafer thickness on cell parameters

4.2.1. Open circuit voltage

To achieve a high V_{OC}, it is essential to initially provide a high excess charge carrier density, which results in a high quasi-Fermi level splitting of the electrons and holes. Secondly, a high contact selectivity, which is the ability of the contact to accept one type of charge carriers over the other, is needed to extract these charge carriers at their corresponding terminals. Figure 4.4 shows a plot of the implied open circuit iV_{OC} and open circuit voltage V_{OC} of several SHJ solar cells plotted with respect to the wafer thickness W ranging from 60 to 170 µm and wafer resistivities ranging from 1 to 3 Ωcm. The theoretical V_{OC} limits at these resistivities are also plotted as the two solid black lines in the graph [10].

The implied open circuit voltage iV_{OC} gives the upper limit of the expected open circuit voltage of the manufactured solar cell and the values were calculated out of the effective lifetime data under 1-sun conditions. The iV_{OC} points shown were obtained after the deposition of the amorphous intrinsic and doped layers but before the deposition of the ITO. The trend of the iV_{OC} follows the theoretical predictions and increases with reduction of wafer thickness with some absolute values of iV_{OC} getting very close to the theoretical limit. For a 60 µm wafer with a resistivity of 2.2 Ωcm, a high iV_{OC} value of 766 mV was recorded, which is remarkably close to the V_{OC} limit of 3 Ωcm c-Si cells modeled by Richter et al.[10] After ITO depositions, very little losses in the iV_{OC} values were observed (not shown). However, a substantial voltage drop was observed for the actual V_{OC} values obtained after the solar cells were finalized with screen printed contacts. This drop was especially significant at wafer thicknesses lower than 64 μm.

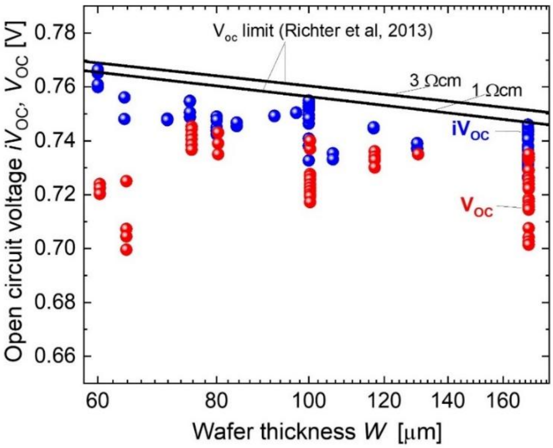

Figure 4.4: Implied open circuit iV_{OC} and open circuit voltage V_{OC} plotted with respect to the wafer thickness W. The measured samples have resistivities ranging from 1 to 3 Ωcm. The solid black lines represent theoretical limits for Si wafers with 1 Ωcm and 3 Ωcm resistivities according to parametrization by Richter et al.[10]

Among several mechanisms reported in the literature as listed by Dumbrell et al.,[140] the most relevant for SHJ solar cell technology is related to the contact shadowing.[140-142] The light shadowing from the front contact leads to inhomogeneous generation of photocurrent which results in internal currents from the open regions with high generation to the shadowed regions under the metal contacts. The related voltage drop then is observed as the difference between iV_{OC} and externally measured V_{OC}. This shadowing effect is reported to be of particular significance in front junction solar cells.[140-143] In the rear junction solar cells studied in this work, the significance of this effect needs additional confirmation. Finally, part of the difference between iV_{OC} and V_{OC} can be explained by the imperfect selective function of the doped layers – carrier selectivity of the contacts[144-146] especially in the high voltage case of thinned wafers. The reduction of externally measured V_{OC} compared to the iV_{OC} i.e. the internal chemical potential of electron-hole pairs, naturally becomes more significant as the wafers are getting thinner and that therefore issues with carrier selectivity of the contacts must be settled in order to preserve the gain in quasi-Fermi level splitting in thinner wafers. An alternative explanation is that at such low thicknesses, there is a higher possibility of wafer damage during metallization process which may also result in this drop on V_{OC}.[147, 148] A similar voltage loss behavior was obtained by Sai et al., for wafer thicknesses less than 70 µm.[149]

4.2.2. Fill factor

Figure 4.5 shows a plot of the implied fill factor *iFF*, pseudo fill factor *pFF* and the fill factor *FF* of the same cells with respect to the wafer thickness. In predictions by Richter et al., as shown by the solid black lines, a slight increase in fill factor with reduced thickness is expected for the studied wafer thickness range.[10] However, as it has been shown in Section 4.1, the implied fill factor (*iFF*) is predominantly governed by SRH recombination at the interfaces and theoretical predictions[10, 11, 92] are of little relevance here. Not surprisingly, the results in Figure 4.5 show a trend opposite to the theoretical predictions – *iFF* slightly decreases with the wafer thickness reduction. Unlike the iV_{OC}, the *iFF* is limited by the SRH recombination dominated by the surface defects and not Auger recombination. This result is consistent with the experimental results obtained by Richter et al.[150] To approach intrinsic limits especially for thinner wafers, significant improvements of passivation of the wafer surfaces is needed. Similar to the iV_{OC} after ITO depositions, very little change in *iFF* values were observed for all wafers (not shown).

After the finalization of the solar cells, the pseudo *FF* (*pFF*) out of J_{SC}-V_{OC} measurement and final *FF* from IV measurements are estimated. The *pFF* represents the diode *FF* without the effect of series and shunt resistance. The drop from *iFF* to *pFF* is smaller in the case of the reference wafer thickness (170 µm) and increases as the wafer thickness is reduced. Similar to V_{OC}, this increased drop from *iFF* to *pFF* for thinner wafers could be as a result of increased effect of contact shadowing[140-142], carrier selectivity of contacts[144-146] and possibly defects caused during the metallization process.[147, 148] The final *FF* values for all wafer thicknesses drops from the *pFF* due to the effect of series resistance.

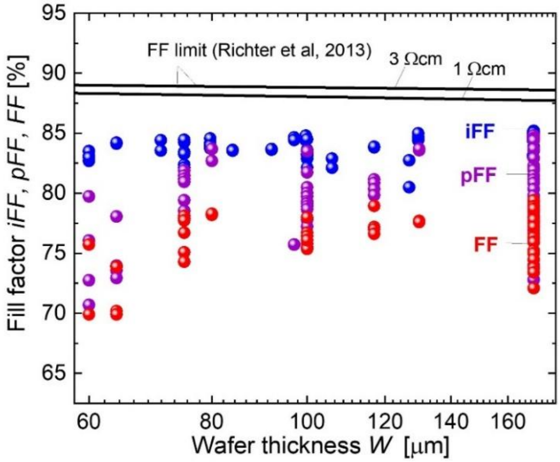

Figure 4.5: Implied fill factor *iFF*, pseudo fill factor *pFF* and fill factor *FF* plotted with respect to the wafer thickness W. The measured samples have resistivities ranging from 1 to 3 Ωcm. The solid black lines represent theoretical limits for Si wafers with 1 Ωcm and 3 Ωcm resistivities according to parametrization by Richter et al.[10]

4.2.3. Short-circuit current density

The short-circuit current density J_{SC} is strongly dependent on the optical properties of the functional layers of the solar cell, including the thickness of the Si wafer. Figure 4.6 shows the J_{SC} values of the cells of different thicknesses with the solid black line representing the theoretical limits based on the Lambertian scattering model which assumes the maximum optical path length enhancement within the cell.[79] There is a significant difference between the theoretical limit and the measured short-circuit current densities which is related to the rather optimistic Lambertian scattering usually implied in the models as well as reflection and shadowing caused by the front metal contact in real solar cells. In addition to these, noticeable J_{SC} losses are also related to the parasitic absorption of some of the light by the passivation and doped layers on the front side of the SHJ solar cells.

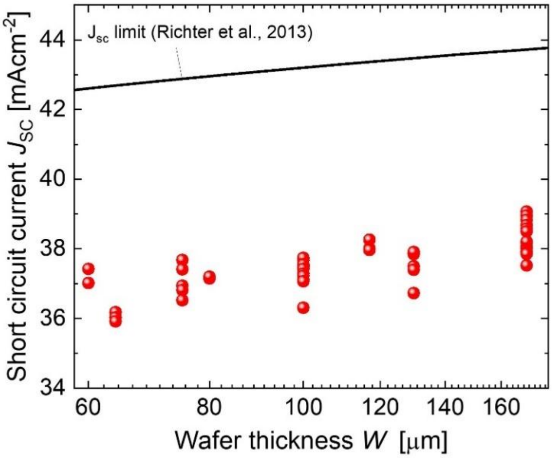

Figure 4.6: Short-circuit current density J_{SC} plotted with respect to the wafer thickness W. The solid black lines represent the J_{SC} theoretical limits for Si wafers parametrization by Richter et al. [10] based on Lambertian scattering model[79]

However, despite the large difference between measured values and theoretical predictions, the trend of measured J_{SC}, which decreases as wafer thickness decreases, is consistent with theoretical predictions. The decrease at the lower thicknesses is a direct result of reduced absorption in the long light wavelength region due to reduced optical path length in the solar cells. To improve the J_{SC} in thinner cells several light trapping strategies such as back reflectors and anti-reflection coatings need to be employed. In the next chapter further discussions on J_{SC} enhancement are explored.

4.2.4. Efficiency

Figure 4.7 shows the final efficiency of the cells at different wafer thicknesses. The trade-off between the decrease in J_{SC} values and the increase in V_{OC} with reduced wafer thickness results in a broad maximum of efficiency. Richter et al., predicted a maximum efficiency at about 110 µm thickness with minimal loss between 60 to 170 µm.[10] The measured results in Figure 4.7 show a similar range of efficiency values between 75 to 170 µm with the best cell efficiency of 22.3 % (V_{OC} = 745 mV, J_{SC} = 37.43 mA cm^{-1} and FF = 80%) obtained at 75 µm although there is no direct link between the work of Richter and the present results due to the significant influence of SRH recombination on the *FF* of the experimental solar cells.

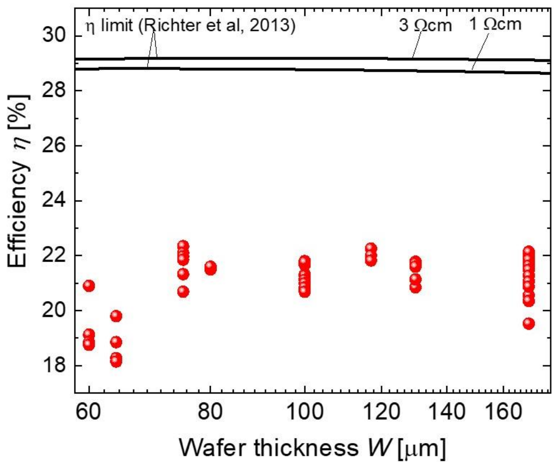

Figure 4.7: Efficiency η plotted with respect to the wafer thickness W. The measured samples have resistivities ranging from 1 to 3 Ωcm. The solid black lines represent theoretical limits for Si wafers with 1 Ωcm and 3 Ωcm resistivities according to parametrization by Richter et al.[10]

Considering the scatter in the data and flat trends, no optimum thickness can be identified. Instead, it can be seen that the wafer thickness can be varied over a significant range without compromising efficiency. Harrison et el., also reports a broad range of high efficiency for solar cell thicknesses between 90 to 160 µm.[147] At lower thicknesses, the decrease in J_{SC} and the possibility of higher defectivity dominate the increased V_{OC}, which results in a decrease in efficiency. With improved surface passivation and higher carrier selectivity of the contacts, there is potential for even higher efficiency in thinner wafers. However, with the existing passivation technology, it is clear that it is possible to reduce by half the thickness of the standard wafers majorly used in the manufacturing of silicon solar cells with no loss and possibly gain in efficiency values.

4.3. Tilt angle performance

Moving beyond the normal AM1.5G standard, it is interesting to explore how solar cells of varying thicknesses perform under different angles of incident solar radiation. This allows for a better understanding of how these cells behave in such scenarios. To perform this experiment, single 21mm by 17 mm mini cells described in screen printing section of Chapter 3 were used to ensure acceptable homogeneity of incident light at different angles. For ease of contacting, copper bands were soldered onto the front and rear busbars of the cells like in the standard module preparation. The cells of different thicknesses were placed on a rotatable stage in the solar simulator. Starting from a zero-degree tilt angle which represents a flat horizontal surface, the stage was tilted to one side and each measurement taken at 15^{o} tilt angle intervals.

Figure 4.8 shows the plots of the different solar cell parameters of cells of different thickness with respect to the tilt angle. In Figure 4.8(a), the measured V_{OC} is shown alongside calculated values that account for the logarithmic dependence of V_{OC} on J_{SC}. Specifically, the calculated curves use the relation:

$$\Delta V = \frac{kT}{q} \ln\left(\frac{J_{SC}(\theta°)}{J_{SC}(0°)}\right) \tag{4.1}$$

where $J_{SC}(\theta°)$ is the short-circuit current density at a given tilt angle and $J_{SC}(0°)$ is the reference value at normal incidence. This approximation isolates the contribution of reduced photogeneration on V_{OC}, illustrating that much of the voltage drop observed with increasing tilt can be attributed to reduced carrier generation rather than intrinsic recombination losses. The close match between measured and calculated highlights the dominant role of illumination intensity in determining V_{OC} at varying angles. However, the measured V_{OC} remains slightly lower than the calculated J_{SC}-dependent values, particularly at higher tilt angles. This discrepancy can be explained by additional real-world effects not captured in the simplified model. First, as tilt angle increases and irradiance decreases, the cells enter a low-injection regime where Shockley-Read-Hall (SRH) recombination becomes more prominent, especially at the surfaces. Additionally, shunt resistance effects are more impactful under these low-light conditions, as leakage currents through shunt paths become relatively more significant and suppress the open-circuit voltage.

The fill factor (*FF*) in Figure 4.8(b) does not exhibit a clear dependence on wafer thickness and tilt angle. This lack of correlation may stem from the complex interplay of dependencies (V_{OC}, J_{SC}, V_{MPP}, and J_{MPP}), which can lead to varying degrees of influence. The major effect is observed in Figure 4.8(c) which shows that at tilt angles greater than 30^{o}, J_{SC} values for all cells converge and wafer thickness effect on J_{SC} becomes of less importance. This effect is directly translated into the overall efficiency of the cells in Figure 4.8(d) which also shows a convergence towards higher tilt angles. The direct implication of this is that although losses in J_{SC} are observed for thinner cells under AM1.5, these losses are of less importance on the field at different angles of incidence without solar trackers.

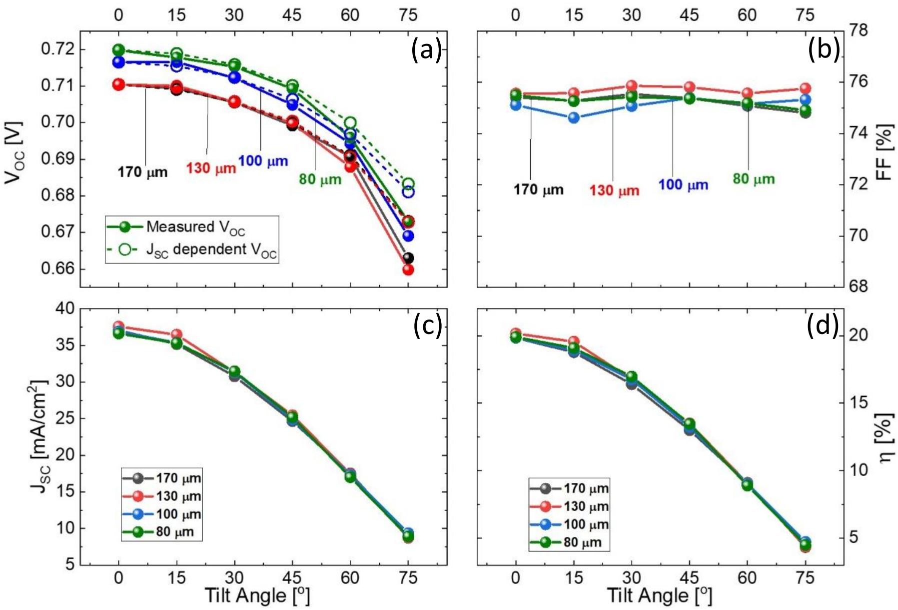

Figure 4.8: a) open circuit voltage V_{OC}; b) fill factor FF; c) short circuit current density J_{SC} and d) efficiency η plotted with respect to the tilt angle of 1-cell minimodules of different wafer thicknesses W (80, 100, 130 and 170 μm) as indicated on the graph.

4.4. Summary

In this chapter, the effect of Si wafer thickness on the performance of silicon heterojunction solar cells was investigated experimentally. Experimental trends were compared to the recent theoretical predictions of the efficiency limit in Si solar cells determined by the Auger recombination. Lifetime measurements revealed that despite the high-quality passivation in SHJ solar cells the carrier lifetime at carrier density below 5×10^{15} cm^{-3} is dominated by the surface recombination which becomes more significant as the wafer gets thinner. A reduction of wafer thickness leads to the reduction of the effective carrier lifetime. The points of 1-sun *iFF* for all studied solar cell precursors are dominated by the surface passivation, thus reduction of wafer thickness leads to the gradual reduction of *iFF* as opposed to the Auger limit predictions.

At higher excess carrier density, all solar cell precursors show transition to the Auger dominated regime which is supported by the differential ideality factor approaching characteristic value of 2/3. The 1-sun iV_{OC} for all studied solar cells belong to the Auger dominated region. Therefore, experimental iV_{OC} closely reproduces theoretical trends and best values are very close to the theoretical Auger limit. Overall, solar cell precursors show that maximum power point of modern SHJ solar cells is still strongly affected by the surface recombination and this effect is stronger in thinner wafers. Approaching fundamental limits of *iFF* will take even further passivation improvement. On the other hand, iV_{OC} is to a large extent Auger limited in highly passivated SHJ solar cells and is very close to the theoretical limit.

As the solar cells are finalized, both *FF* and V_{OC} show noticeable loss which increases with thickness reduction even excluding effects of parasitic resistances. This loss is attributed to contact shadowing and imperfect selectivity of the contacts which is critical in high voltage SHJ solar cells on thin wafers. Short-circuit current predictably reduces with thickness reduction due to weaker absorption in the long wavelength region. The short-circuit current density J_{SC} follows the theoretically predicted trend while absolute values are significantly lower than the limit based on Lambertian scattering, which leaves significant space for optimization.

Even though some challenging improvements have to be made to attain fundamental limits, the solar cells of various thicknesses show high efficiency. A broad range of high efficiency was observed for thicknesses ranging from 75 to 170 μm with a maximum of 22.3% obtained at 75 μm. This result shows the opportunity to reduce the wafer thickness down to approx. 75 μm without noticeable reduction in of efficiency. A further reduction of the wafer thickness would take additional improvement in the passivation quality, contact selectivity, and eventually light trapping.

The chapter concludes by addressing the performance of representative cells of different thicknesses at various tilt angles. This part of the investigation sheds light on how wafer thickness and orientation relative to sunlight affects the performance of the solar cells. It can be observed that at tilt angles greater than 30°, the J_{SC}, and by extension the efficiency, of solar cells with different thicknesses converge. This implies that while thinner cells exhibit losses in J_{SC} under AM1.5 conditions, these losses become less significant in real-life field applications without solar tracking devices at certain sun inclinations.

5. Thin SHJ solar cells as bottom cells in Pero-Si tandems

Large-scale production of Pero-Si tandems in the future is expected to use Si wafers thinner than 100 µm for both economic and sustainability reasons. Based on this projection, in this chapter, the performance of SHJ cells on 80 µm thick wafers under bottom cell conditions in Pero-Si tandem was examined and compared to those on the more common 135 µm thick wafers. This study consists of two sections dedicated to *passivation* and *light management*. In the first section, the passivation layer thickness effect on the performance of SHJ cells prepared on 80 µm thick wafers in comparison to 135 µm thick reference were studied. These cells will be referred to as "80 µm cells" and "135 µm cells", respectively, for the sake of brevity. First the 80 µm and 135 µm cells are compared under AM1.5G standard test conditions. Then, these cells are studied under perovskite-filtered spectrum - the spectrum a bottom cell would experience in Pero-Si tandem under AM1.5G standard test conditions. Additionally, to resolve any spectrum-specific influence on the operation of the SHJ cells measurements done under the "Perovskite-filtered" spectrum were compared to the measurements under attenuated AM1.5G spectrum so that the cells received same total photon flux in both cases. In the second section, the application of one-dimensional back reflectors and the MgF_2 anti-reflection coating were addressed to improve light trapping in SHJ bottom cells based on the thin and reference wafers with different thickness of the passivation layer from the first part of the study. Some of the results presented in this chapter have been published in ref.[151].

5.1. Passivation Layer Thickness Variation

In this section, the effect of passivation layer thickness on 80 µm and 135 µm SHJ solar cells under AM1.5G, attenuated AM1.5G, and perovskite-filtered spectra were studied. The structure of the SHJ solar cell is schematically presented in Figure 5.1(a). Each passivation layer on both sides of the wafer consists of two films of intrinsic hydrogenated amorphous silicon. The first layer (i1) is a rapidly deposited porous buffer layer which prevents epitaxial crystallization on the interface and a denser second layer (i2) is deposited to make up the actual passivation layer[68]. Only the i2 layer thickness is varied in this study by tripling the deposition time on the front side and/or doubling the deposition time on the rear side as shown in the table in Figure 5.1(b). For the sake of brevity, the cells will be addressed as follows: cells with the reference i-layer thickness on both sides will be referred to as "standard cells," those with a thicker i-layer only on the p-side as "p-side cells," those with a thicker i-layer only on the n-side as "n-side cells," and those with a thicker i-layer on both sides as "both sides cells."

(a)

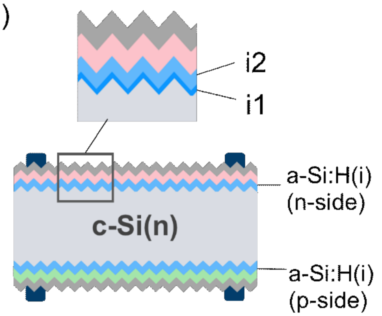

(b)

Rear / Front	Baseline	2 x i2
Baseline	**standard**	**p-side**
3 x i2	**n-side**	**both sides**

Figure 5.1: (a) Silicon heterojunction solar cells schematic showing the two intrinsic amorphous silicon passivation layers; (b) passivation layer thickness variations on the front and / or rear side studied.

The performance of the 80 µm and 135 µm cells with the different passivation layer thickness combinations before light curing and annealing is summarized in Figure 5.2. As already observed in the Chapter 4, Figure 5.2(a) shows that under AM1.5G the solar cells made on thinner wafers produce higher open-circuit voltage (V_{OC}) compared to the thicker cells[134, 152] because of increased excess charge carrier concentration in thinner wafers[10, 134, 152]. The lower implied fill factor (i*FF*) in thin cells in Figure 5.2(b) is attributed to increased impact of the surface recombination and reduced short-circuit current density (J_{SC}) in Figure 5.2(c) is a result of reduced IR light absorption in thinner wafers. Under AM1.5G, the 80 µm cells with standard passivation gain approximately 4.4 mV in V_{OC} over the 135 µm cells of the same passivation and lose about 0.37 mA/cm^2 in J_{SC}.

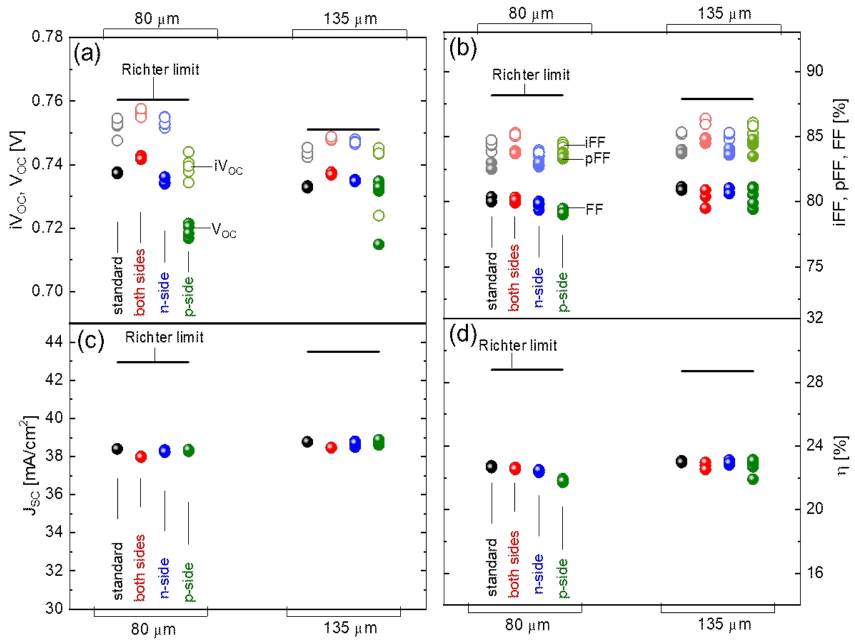

Figure 5.2: (a) Implied open circuit iV_{OC} and open-circuit voltage V_{OC}; (b) i*FF*, p*FF*, and *FF*; (c) short-circuit current density J_{SC}; and (d) efficiency η plotted for the different passivation layer variations for wafer thicknesses of 135 and 80 µm under AM1.5G spectrum and before light soaking and annealing process. Solid black lines represent the theoretical limit[10].

From the passivation layer thickness point of view, as expected, the highest iV_{OC} of 758 mV and i*FF* of 86.4% were obtained for the "both sides" cells. This is attributed to the reduced surface recombination on both interfaces passivated with thicker amorphous silicon layers. However, for the 80 µm cells, lower iV_{OC} and V_{OC} were observed for the "n-side" and "p-side" cells than the "standard" cells which is inconsistent with the expectations of cells with thicker passivation. The reason for this is not fully understood, but at the moment, it is attributed to batch-to-batch variability in the wafer thinning process. Similar drops between iV_{OC} and V_{OC} (approx. 0.18 mV for 80 µm and 0.11 mV for 135 µm cell thickness) in all samples, suggest similar contact recombination loss irrespective of the passivation layer thickness. In general, increasing the passivation thickness on either side of the solar cell is expected to increase series resistance loss. This can be seen in Figure 5.2(b) where on average, the difference between pseudo-*FF* (p*FF*) and *FF* is smallest for the standard cells (2.7%$_{abs}$) which have the thinnest passivation layers amongst all cell variants. Interestingly, a higher p*FF* to *FF* loss is observed for the both sides (4.0%$_{abs}$) and the p-side (4.1%$_{abs}$) cells than the n-side cells (3.2%$_{abs}$) which indicates that thicker passivation layer at the n/i/p junction contributes stronger to series resistance than at the n/i/n interface.

With thicker passivation on both sides, an additional 4.7 mV in V_{OC} is gained for the 80 µm cells over the 80 µm cells with standard passivation. However, this gain in V_{OC} is counterbalanced by an additional J_{SC} loss of about 0.40 mA/cm^2 which results in a slightly lower final efficiency for both sides variant (22.7%) compared to the standard variant (22.8%) for the 80 µm cells. At this cell development stage, the best 135 µm cell efficiency is approximately 0.5%$_{abs}$ greater than the best 80 µm cell. Overall, as might be expected, there is no advantage of the thicker passivating layer under AM1.5G irradiance, and thinner wafers show a mild drop in efficiency. At the next stage, the full set of samples presented in Figure 5.2 has been exposed to the light soaking (LS) and subsequent annealing.

5.1.1. Light soaking and annealing effect

Hydrogenated amorphous silicon is prone to the creation of additional defect states under light exposure. This effect, known as the Staebler-Wronski effect[153] is detrimental for efficiency in thin film Si solar cells[153] and has been reported for light-soaked i/c-Si/i interface structures[154]. However SHJ cells with doped amorphous Si layers deposited on either side on contrary have been reported to gain in passivation quality after light exposure[154]. In Figure 5.3, the results of the full set of samples before and after light soaking (LS) and annealing are compared. All samples show increase in V_{OC} after the LS and annealing with the most gain of up to 22.2 mV in the p-side 80 µm cells which had lowest V_{OC} values before LS treatment. The "both sides" cells show the highest V_{OC} of 747 mV in 80 µm cells and 741 mV in 135 µm cells. The gain in V_{OC} after LS and annealing is approximately 5.3 mV for 80 µm and 4.8 mV for 135 µm cells (lowest in these cells among the whole sample set). It is speculated that as these cells approaching an Auger-recombination-dominated regime, where further increases in V_{OC} are becoming more challenging, as has been demonstrated earlier [134]. Similarly, for the p*FF* in Figure 5.3(b), the least gains ranging from 0.4 to 0.7%$_{abs}$ are observed for both sides cells of 80 µm thickness.

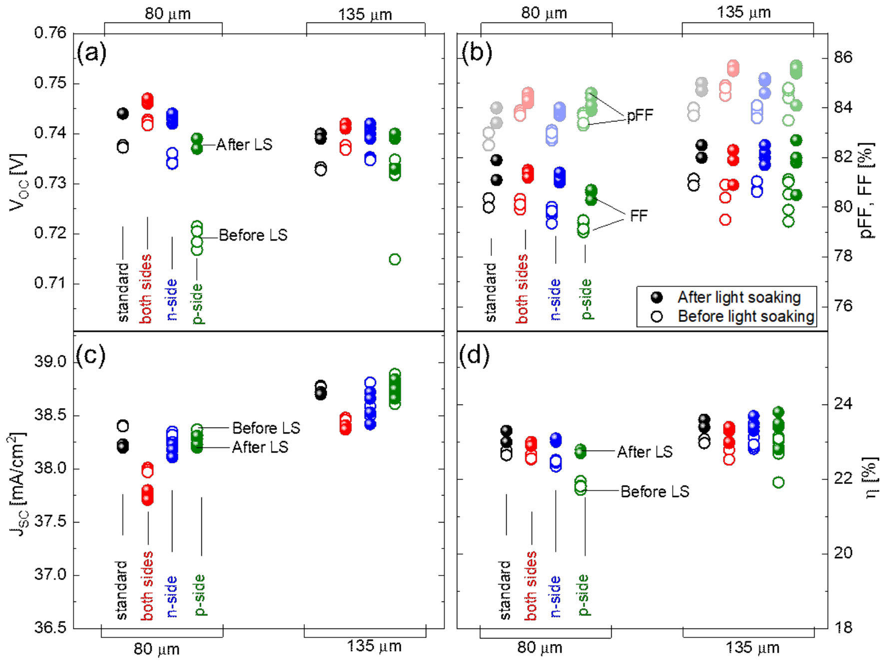

Figure 5.3: (a) Open-circuit voltage V_{OC}; (b) pseudo fill factor p*FF* and fill factor *FF*; (c) short-circuit current density J_{SC}; and (d) efficiency η plotted for the different passivation layer variations for wafer thicknesses of 135 and 80 µm under AM1.5G spectrum. All values measured before and after light soaking and annealing.

For all cell types and thicknesses, the LS and annealing improves *FF* (up to 1.9%$_{abs}$) stronger than the p*FF* (max. 1.3 %$_{abs}$), which indicates improvements not only in the passivation but also in the conductivity of the cells. While the light soaking process has little to no effect on the J_{SC} of the 135 µm cells in Figure 5.3(c), a slight loss in J_{SC} is observed for the thinner cells. Overall gains in V_{OC} and *FF* result in efficiency gain for all cell types with the most gain of 0.98 %$_{abs}$ and 0.88 %$_{abs}$ observed for the p-side variants of 80 µm and 135 µm, respectively. At this point, under the AM1.5G irradiance, the best 80 µm cell with an efficiency of 23.3 % is the cell with standard passivation while the best 135 µm cell with an efficiency of 23.8 % is the cell with thicker passivation on p-side.

5.1.2. Intensity dependence

After the standard test conditions, the operating conditions in the Pero-Si tandems are approached by first addressing the effect of irradiance. Figure 5.4 shows the dependencies of the photovoltaic parameters on irradiance for representative standard and both sides cell types prepared on 135 and 80 µm thick wafers. In Figure 5.4(a) the dependence of V_{OC} on irradiance is presented. The "both sides" thicker passivation cells show consistently higher V_{OC} on reference and thin wafers. The V_{OC} dependencies show a gradual change in slope from steeper at low intensity to flatter at high intensity. The thin wafer cells have somewhat steeper dependencies as compared to the standard wafer counterparts. The gain in V_{OC} attained in thin wafer cells is highest at one sun and reduces with reduction of intensity. Nonetheless, at 0.44 suns, which is the expected light intensity under the perovskite-filtered spectrum, the 80 µm cells still show 3-5 mV higher V_{OC} compared to the 135 µm reference.

Figure 5.4(b) shows dependencies of *FF* on irradiance. From a wafer thickness perspective, the thinner wafer lose approximately $1\%_{abs}$ of *FF* for the whole range of irradiance as compared to the reference cells. This is due to the stronger impact of the SRH surface recombination in thinner cells[134]. From the perspective of the passivation layer thickness, despite the two variations (standard and both sides) having similar values under 1 sun irradiance, a clear gain in fill factor is observed for the both-sides variant at lower intensities, clearly showing the effects of improved passivation which has been masked by the series resistance under one sun. Here, the example of the *FF* gain achieved thanks to relaxed series resistance constrains in SHJ cell in perovskite shadow can be seen.

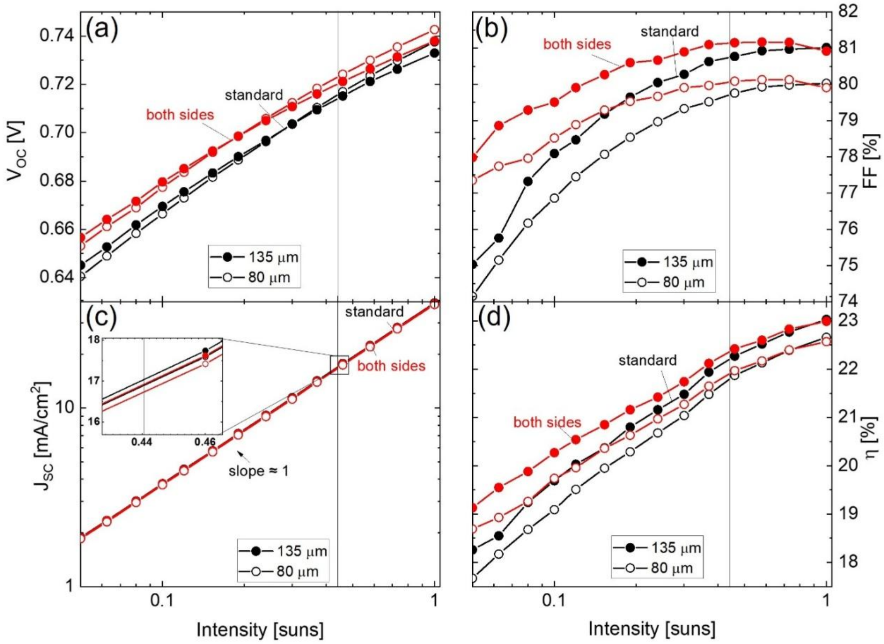

Figure 5.4: Intensity dependence of (a) open circuit voltage, V_{OC}; (b) fill factor, FF; (c) short circuit current density, J_{SC}; and (d) efficiency, η plotted for standard and both sides variations and for wafer thicknesses of 135 and 80 µm.

Figure 5.4(c) shows a very consistent linear dependence of J_{SC} on the irradiance for all cells with a slope approximately equal to 1. At this light intensity, the J_{SC} for cells with thicker passivation on both sides remain slightly less than that of the cells with standard passivation thickness, however, under perovskite-filtered spectrum, no additional losses are expected due to thicker passivation on the front side. Despite being slightly lower under AM1.5G, the final efficiency with respect to incident light intensity in Figure 5.4(d) shows higher values for the cells with thicker passivation on both sides than the standard cells with differences of 0.1%$_{abs}$ for 80 µm and 0.15%$_{abs}$ for 135 µm cells at the studied light intensity. It is important to note that here, the efficiencies were calculated using:

$$\eta = \frac{J_{SC} \times V_{OC} \times FF}{P_{in}} \tag{5.1}$$

where P_{in} here represents the input power at each light intensity.

5.1.3. Performance under perovskite-filtered spectrum

In this section, all cells are compared under the target Perovskite-filtered spectrum and the results are presented in Figure 5.5. To study possible spectral related effects, the performance of the cells under the perovskite-filtered spectrum to the measurements under AM1.5G spectrum attenuated are compared to the same photon flux (0.44 suns). In this case, all efficiencies were calculated using P_{in} at AM1.5G (100 mW/cm^2) to simulate the actual contribution as the bottom cell in a perovkite/silicon tandem . Figure 5.6 shows the different spectra used for this study and also the EQE plots of representative 80 and 135 µm cells.

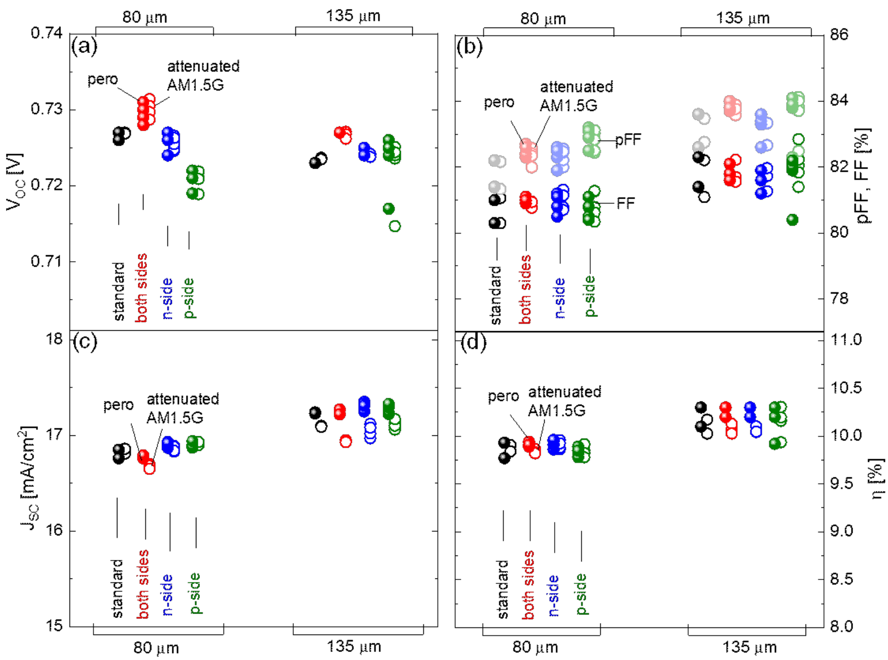

Figure 5.5: (a) Implied open circuit iV_{OC} and open-circuit voltage V_{OC}; (b) i*FF*, p*FF*, and *FF*; (c) short-circuit current density J_{SC}; and (d) efficiency η plotted for the different passivation layer variations for wafer thicknesses of 80 and 135 µm under perovskite-filtered spectrum and under AM1.5G spectrum at the same intensity.

It can be seen in Figure 5.5(a) and (b) that both attenuated and perovskite-filtered spectra result in same V_{OC}, p*FF*, and *FF*. Therefore, it can be concluded that significant modification of the spectrum does not have any effect on the V_{OC} and *FF*. This fact is of interest to streamline further development of the SHJ bottom cells for tandem applications. The primary optimization loop for the V_{OC} and *FF* in these cells can utilize simple attenuation of the typical solar simulator irradiance without modification of the spectrum or building actual tandem cells.

For the 135 µm cells, a slight increase in J_{SC} of approx. 0.33 mA/cm^2 is observed in Figure 5.5(c) under the perovskite-filtered spectrum in comparison to the attenuated AM1.5G. Here, the reduced effect parasitic absorption of the short wavelength light is observed under Perovskite-filtered spectrum. For the 80 µm cells however, little to no gain in J_{SC} is noted. This is most likely as a result of two counterbalancing effects taking place in this case. On the one hand, the losses in the short wavelength region are absent so there is a net gain in current. On the other hand, the J_{SC} loss due to the transmission losses is magnified in the near infra-red range. This is because for same photon flux, the Perovskite-filtered spectrum has a higher spectral density in the near infrared region than the attenuated AM1.5G as can be seen in Figure 5.6. A reduction in EQE in 80 µm cells is presented in Figure 5.6 as well. Final efficiencies presented in Figure 5.5(d) do not show any definite trend among all passivation layer variants. There is an average loss of approx. 0.35%$_{abs}$ when wafer thickness is reduced from 135 µm to 80 µm.

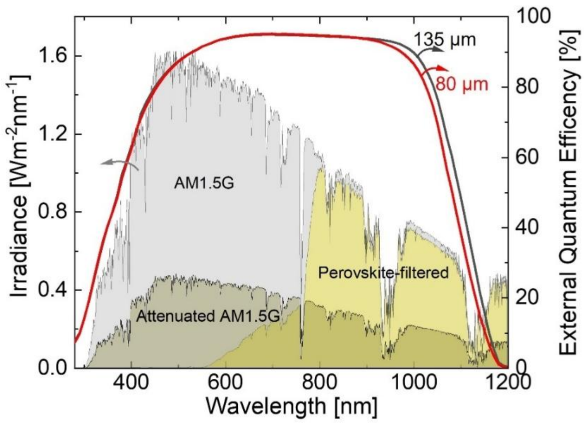

Figure 5.6: Attenuated AM1.5G and perovskite-filtered irradiance spectra at the same intensity and EQE plots showing differences in infrared light absorption for 80 µm and 135 µm cells.

This result looks optimistic for the thin-wafer bottom solar cells. It can be seen that a major wafer thickness reduction of 40% turns to only approx. 0.35%$_{abs}$ loss in the bottom cell efficiency. This makes the application of 80 μm wafers viable for the Pero-Si tandems in future. Based on the passivation study, relaxed optimization conditions to the optical absorption in the thin film Si stack allows increase of the passivation layer thickness with related gain in passivation quality. As this study covered only a little fraction of all stack optimization options, more potential is expected to be discovered in future studies. As the major difference between 135 μm and thin 80 μm cells is in the near IR absorption loss, the next section elaborates on this topic.

5.2. Light management

In this section, the issue of the photocurrent loss in the near-infrared absorption region in thin wafer Si solar cells[10, 134] is addressed with two strategies. Firstly, light trapping options are considered to reduce the transmission of infrared light through the rear side. While a variety of advanced architectures exist for efficient light trapping[30, 155-158], simple solutions such as optimized one-dimensional back reflector (BR) are preferrable for large scale production. Full back Ag layer deposited directly on indium tin oxide (ITO) at the rear side is a common one-dimensional back reflector option, however, there have been reports of parasitic plasmonic absorption at the interface between TCOs and metals.[68, 77] To mitigate this, an additional interlayer of a low refractive index dielectric material such as MgF_2 is used.[68] The second strategy to minimize the infrared absorption loss in thin wafers is the deposition of an anti-reflection coating on the front side with thickness optimized to promote the transmittance of infra-red light to the bottom cell. For example MgF_2 is considered a suitable material for anti-reflection not only for SHJ solar cells[76] but also in perovskite/silicon tandems[159]. While the MgF_2 coating may perform differently when deposited directly on the SHJ front side, the perovskite front side, or even in the case of encapsulation with another material, the possibility of improving infrared light absorption in thin SHJ bottom cells via antireflective coating optimization is only demonstrated here.

5.2.1. Back reflector optimization

To optimize the back reflector, several BR stacks of ITO/Ag and ITO/MgF_2/Ag with different thicknesses of ITO were tested on reference 135 μm cells. The cells were first measured using a black chuck before the deposition of the stacked BR layers to obtain the relative difference. The relative difference in short-circuit current was calculated as the percentage ratio of the J_{SC} difference before and after BR deposition (ΔJ_{SC}) to the J_{SC} value before BR deposition. Figure 5.7 illustrates the relative difference in J_{SC} for various BR stacks. The results indicate that BR stacks lacking MgF_2 generally exhibit lower relative differences. For instance, the ITO (140 nm) + Ag (200 nm) stack shows an average ΔJ_{SC} of 0.30 mA/cm^2, whereas the ITO (140 nm) + MgF_2 (160 nm) + Ag (200 nm) stack achieved an average ΔJ_{SC} of 0.46 mA/cm^2.

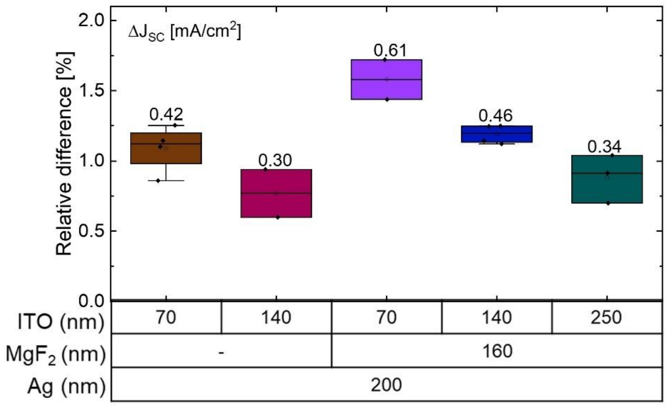

Figure 5.7: Plot of relative difference in J_{SC} for various cells with different back reflector thickness combinations. Numbers in the plot indicate the average absolute J_{SC} gain in mA/cm^2.

The highest ΔJ_{SC} without MgF_2 is observed with the ITO (70 nm) + Ag (200 nm) stack, which shows an average difference of 0.42 mA/cm^2. In contrast, the best performing BR stack, comprising ITO (70 nm), MgF_2 (160 nm), and Ag (200 nm), achieved a ΔJ_{SC} of 0.61 mA/cm^2 (approximately 1.5% relative difference). This demonstrates that the inclusion of MgF_2 in the stack significantly enhances J_{SC} by reducing losses due plasmonic absorption, aligning with earlier findings[23]. Additionally, thicker ITO layers resulted in lower ΔJ_{SC} due to increased greater parasitic absorption loss.

5.2.2. Impact of back reflector and anti-reflection coating on J_{SC}

In this section, the best performing BR stack (ITO 70 nm + MgF_2 160 nm + Ag 200 nm) in Figure 5.7 was deposited in all samples studied in Section 5.1. Subsequently, the samples were all finalized with MgF_2 anti-reflection coating (ARC). The J_{SC} performance of the cells before BR, after BR, and after ARC are presented in Figure 5.8. The left graph Figure 5.8(a) presents the J_{SC} values measured under AM1.5G, and the right graph Figure 5.8(b) presents the J_{SC} values measured under the perovskite-filtered spectrum. A significant improvement in J_{SC} for all cell types under both AM1.5G and perovskite-filtered spectrum is observed due to the effect of the BR and the ARC.

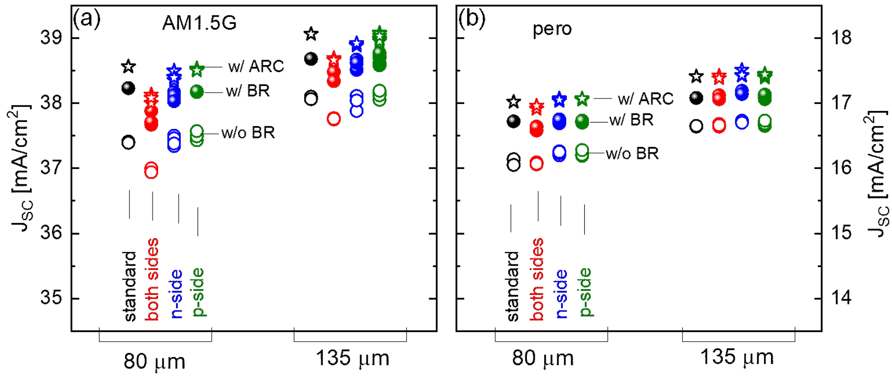

Figure 5.8: Short circuit current density with and without ITO/MgF_2/Ag back reflector and after MgF_2 ARC for the various cell variations under (a) AM1.5G and (b) perovskite-filtered spectra.

To get a more detailed view on the effect of both back reflector and antireflective coating, the differential J_{SC} gain is presented in Figure 5.9. The left graph Figure 5.9(a) presents data on J_{SC} gain after the deposition of BR while the right graph Figure 5.9(b) presents the J_{SC} gain attained at the next step after ARC deposition. As it can be expected most gain in J_{SC} after BR application is attained in the cells with most near IR losses, namely the 80µm solar cells gain up to 0.88 mA/cm^2 under AM1.5G and up to 0.58 mA/cm^2 under the Perovskite-filtered spectrum after the application of BR. In the same respective cases, the 135 µm cells gain 0.73 mA/cm^2 and 0.52 mA/cm^2. It seems to be practically feasible to reduce the difference in J_{SC} between the 80 µm and 135 µm cells even further with more advanced back reflectors.

After MgF_2 ARC deposition, no distinct trend is observed as presented in Figure 5.9(b). All cells gain on average approx. 0.3 mA/cm^2 for both spectra because applied the ARC is designed to perform best in the long wavelength range which is approx. same for both spectra. The ARC applied in the experiment was effective at the air/cell interface, and further ARC optimization may be required for monolithic PeroSi tandems. In total, in the cells with thicker passivation layer on both sides, total J_{SC} gains of up to 1.2 mA/cm^2 and 0.9 mA/cm^2 were obtained under AM1.5G spectrum for 80 µm and 135 µm wafers, respectively.

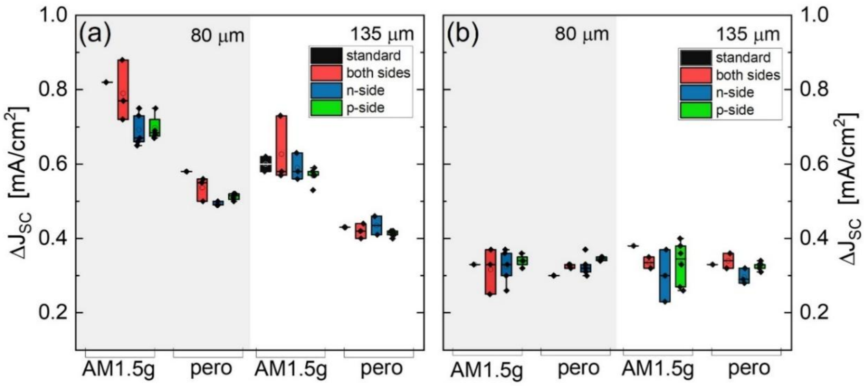

Figure 5.9: Short circuit current density difference (a) with and without ITO/MgF_2/Ag back reflector and (b) before and after MgF_2 ARC for the various cell variations under AM1.5G and perovskite-filtered spectra.

The external quantum efficiency (EQE) and absorptance (1-Ref) spectra for representative 80 µm cells are summarized in Figure 5.10. The different variants of passivation layer thicknesses presented in Figure 5.10(a) show mostly variations in the short wavelength region. Thicker passivation layer increases parasitic absorption loss in the wavelength region between 350 and 600nm. It can be seen that on the infrared region, the EQEs and the 1-Ref spectra of all cells are not affected by the variations in the passivating layers in this work. Therefore, under the PeroSi tandem conditions, the differences in J_{SC} between the different passivation variations are minimal.

From a light management perspective in Figure 5.10(b), for the cell without back reflector, “1-Ref” is high in the 1100 – 1200 nm range despite having the lowest EQE in the infra-red region. This is due to the high transmission loss on the rear side. The introduction of a back reflector enhances the absorption of long wavelength light. This improvement can be observed in the enhanced EQE curve which initiates at approximately 900 nm wavelength.

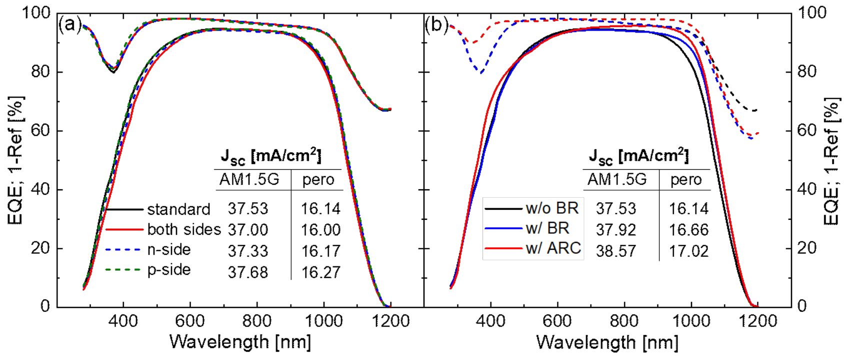

Figure 5.10: External quantum efficiency and 1-Reflectance of SHJ solar cells for (a) 80 µm cells with the different passivation thickness variations and without BR and ARC and (b) 80 µm standard passivation cell without BR, with MgF_2/Ag back BR and after MgF_2 ARC.

After the deposition of MgF_2 ARC, further improvement in EQE is observed in the UV region between 340 nm and 480 nm and in the near IR region between 700 nm and 1040 nm. As previously mentioned, it is important to note that the MgF_2 coating may perform differently when deposited directly on the perovskite front side or even in the case of encapsulation with another material.

5.3. Summary

In this chapter, the applicability of thin wafer based SHJ solar cells as bottom cells in perovskite-silicon tandem cells was studied. The study addressed two crucial issues regarding thin SHJ solar cells: surface passivation, and light management. The consequences of thicker passivating layers in SHJ solar cells were researched to assess the potential for passivation improvement. In addition, the effect of a technologically relevant one-dimensional ITO/MgF_2/Ag back reflector and MgF_2 antireflective coating on light management was analyzed. For consistency, all cells were characterized using standard test conditions with AM1.5G irradiance, attenuated AM1.5G irradiance, and with Perovskite-filtered spectrum. The latter is the spectrum that a bottom cell would encounter in a Pero-Si tandem configuration.

Thin SHJ solar cells as bottom cells in Pero-Si tandems

As can be expected under AM1.5G standard measurements, a thicker passivating layer does not confer any particular advantage, and thinner wafers show a slight decline in efficiency. While thicker passivation layers lead to an increase in series resistance and parasitic absorption, they also improve passivation, resulting in a peak V_{OC} of 747 mV in 80 µm cells and 741 mV in 135 µm cells. The best 80 µm cell of this study had an efficiency of 23.3 % while the best 135 µm cell had an efficiency of 23.8 %. Under lower light intensity equivalent to the conditions at the bottom cell, a significant enhancement in fill factor is observed with the thicker passivation layer. This is due to better passivation and reduced impact of the series resistance. To investigate the potential spectral effects on V_{OC} and *FF*, the study compared cells measured under a perovskite-filtered spectrum to those measured under the AM1.5G spectrum that was attenuated to the same photon flux (0.44 suns). Both spectra result in the relatively same V_{OC}, p*FF*, and *FF*. This can facilitate the main optimization loop for V_{OC} and *FF* in bottom cells by simply attenuating the standard solar simulator irradiance without modifying the spectrum. Under the Perovskite-filtered spectrum, the results indicate a favorable outcome for the SHJ cells with thinner wafers. Despite reducing the wafer thickness by 40%, there is only a minimal decrease of approximately 0.35$\%_{abs}$ in the bottom cell efficiency, even without the implementation of anti-reflection or back reflector measures. These findings suggest that adopting 80 µm wafers is a viable approach for developing mass-produced Pero-Si tandems.

The implementation of an ITO/MgF_2/Ag back reflector and a MgF_2 anti-reflection coating can notably reduce the variation between 80 µm and 135 µm cells. In this work, the use of a back reflector leads to a J_{SC} increase of up to 0.58 mA/cm^2 for 80 µm solar cells under the Perovskite-filtered spectrum while 135 µm cells exhibit a gain of 0.52 mA/cm^2. In addition, the application of the anti-reflection coating results in an average increase of approximately 0.3 mA/cm^2 across all cells. In total, the study exhibits a rise of 0.9 mA/cm^2 in short-circuit current density at 80 µm under the perovskite-filtered spectrum due to enhanced light management.

In conclusion, this study shows that a significant decrease in wafer thickness in SHJ bottom cells for the Pero-Si tandems leads to only a minor decline in power conversion efficiency. Further optimization studies can be done by modifying the perovskite-filtered spectrum modelled as reduction in the thickness of the perovskite top cell and thereby, increasing the J_{SC} in the SHJ bottom cell which will particularly be beneficial in 4-terminal configurations.

6. Thin SHJ solar cells for indoor applications

Solar cells can be used as indoor light harvesters for low power intensive stand-alone devices such as the internet of things, wireless sensors etc. The light intensity in a well-lit classroom or office is usually lies between 250 to 500 lux which is by several orders less than the typical outdoor conditions.[160] Also, the spectrum of artificial lighting is more concentrated in the visible light region than for the solar spectrum which is spread out from the UV to the IR region. The different light properties result in significantly different requirements to solar cell absorber material. For Si it means that much thinner wafers are required to absorb the available spectrum efficiently. In this chapter, the experimental performance of solar cells with varying thicknesses under indoor conditions is discussed briefly. The impact of different cell thicknesses (80 µm, 100 µm, 130 µm, and 170 µm) on the open circuit voltage, fill factor, and efficiency is analyzed under both sunlight and LED illumination. For the sake of homogeneity of the incident light especially at such low intensities and compatibility with measuring device, single mini cells with external copper contacts as described in Section 4.3 were used. Some of the results presented in this chapter have been published in ref.[134]

6.1. Performance under low light and LED

Figure 6.1 shows the effect of the thickness of the silicon wafers on the external quantum efficiency of the solar cell and with respect to normalized LED and sun irradiance. There is a slight shift in the IR to lower wavelengths as the thickness of the solar cell is reduced. This leads to a reduction of the short-circuit current density under solar illumination as already observed and discussed in Section 4.2.3. There is also a slight difference in the short wavelength region between the reference 170 μm cells and the thinner cells which is likely related to the difference in surface texture between the reference and thinned wafers.

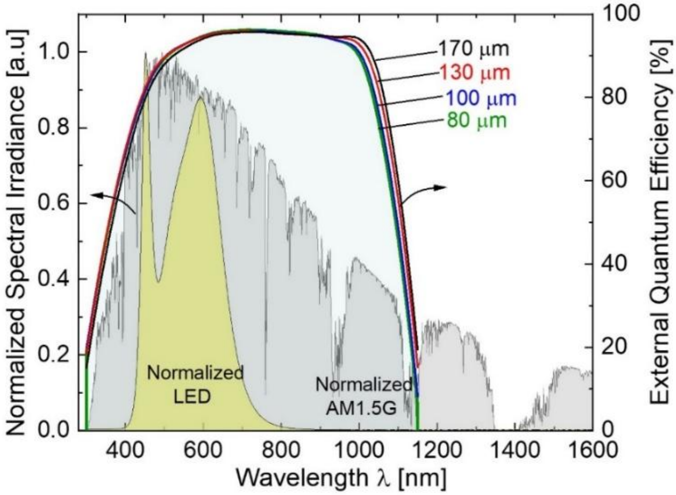

Figure 6.1: Normalized spectral irradiance of solar simulator and LED and the external quantum efficiency (EQE) of SHJ solar cells at different thicknesses.

Under LED illumination, there is no expected loss in current at high wavelengths because no photons are produced by the LED at the infrared region. In fact, from the EQE and J_{SC} point of view, since narrower EQEs are expected as the cell thickness reduces, much thinner wafers can be used without any optical loss under LED. Additionally, since a reduction in wafer thickness leads to an increase in voltage, it is possible to improve the solar cell efficiency under LED by producing ultrathin silicon solar cells with no incurred optical losses. Bahrami-Yekta et al, predicts an optimum thickness of 1.8 μm for LED light harvesting as opposed to 109 μm under solar illumination.[118] Since achieving such thickness in c-Si typically requires costly bottom-up methods like epitaxial growth, it's crucial to explore the use of practical thin c-Si solar cells made with conventional, widely-used manufacturing techniques.

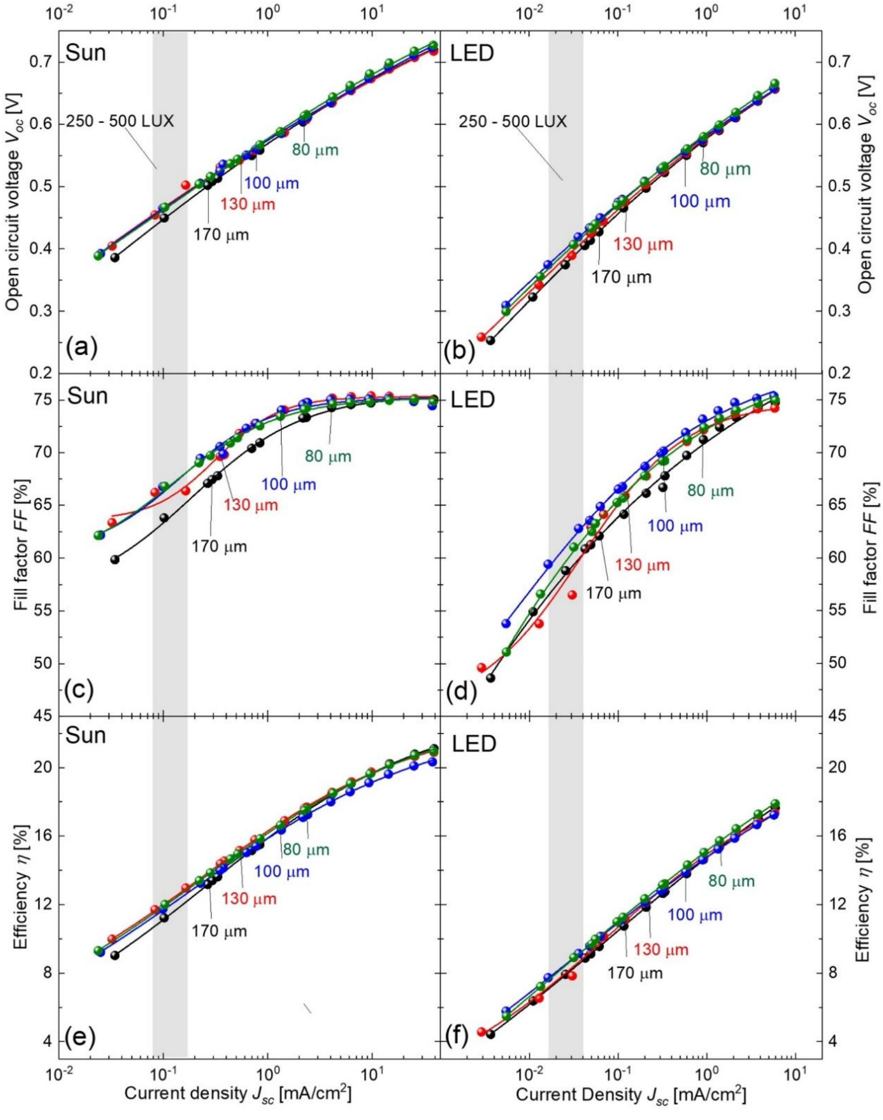

Figure 6.2: The open-circuit voltage V_{OC} ((a) and (b)); fill factor FF ((c) and (d)) and efficiency η ((e) and (f)) for one solar cell SHJ solar modules of different thicknesses in different illumination intensities under the simulated sun and LED light sources, respectively. The solid lines represent the fit for data points for each wafer thickness. The shaded areas represent the intensity for typical indoor lighting (250 – 500 LUX).

Thin SHJ solar cells for indoor applications

Figure 6.2 shows the V_{OC}, *FF* and efficiency η at the different light intensities (J_{SC}) under simulated sun and LED lighting for 80, 100, 130 and 170 µm SHJ solar cells. The shaded areas represent the region where the light intensity ranges from 250 – 500 LUX which is the typical lighting for a bright office.

There is an expected general decrease in photovoltaic parameters as the intensity of light is reduced as can be seen in Figure 6.2. At higher light intensity, very little difference in V_{OC} is observed between the different wafer thicknesses under sun and LED illumination. However, towards lower intensities, a slightly steeper drop in V_{OC} is noticed for thicker wafers. The *FF* values obtained at 1 sun in Figure 6.2(c) are low compared to values recorded in Figure 4.5 likely due to perimeter recombination losses which increases for smaller sized solar cells.[161] Under sun illumination, an initial decrease in intensity leads to a slight increase *FF* due to reduced effects of series resistance. A further decrease in intensity results in a sharp decrease in the fill factor values which is likely due to shunt resistance effects for small scale solar cells. Under LED illumination in Figure 6.2(d), the initial series resistance effect at high intensity is not observed, as the light intensity is lower than that of the sun. The shunt resistance effect is evident for all cells, with thicker cells performing worse than the 80 and 100 µm cells. This contrasts with Figure 5.4(b), where thicker cells show a higher fill factor. Thicker cells have a higher edge-to-cell ratio, which leads to more pronounced edge recombination in smaller cells (21 x 17 mm^2) compared to larger ones (156 x 156 mm^2). This supports the argument for using thinner cells in indoor applications, where smaller cell areas are most likely to be used. There is a slightly higher overall efficiency for the 80 and 100 µm cells especially in LED low light conditions as shown in Figure 6.2(f). This suggests that further decrease in solar cell thickness could lead to better performance for indoor applications.

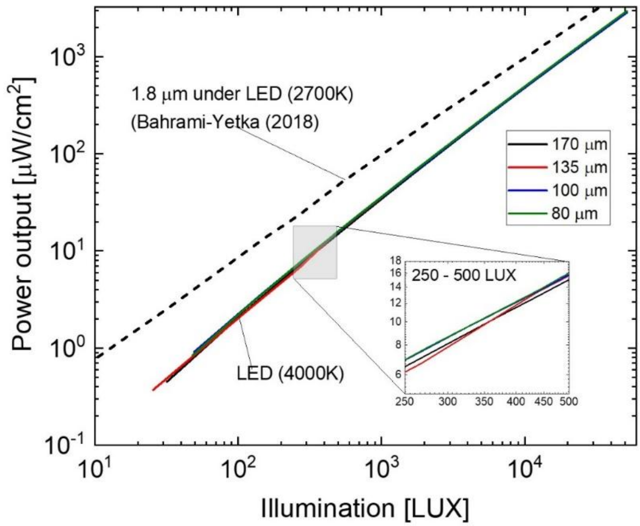

Figure 6.3: Power output vs. illumination intensity in LUX for the different SHJ solar cell thicknesses under 4000k LED lighting. Dashed line shows the maximum expected power output for a solar cell of optimal thickness 1.8 μm under LED (2700k) as calculated in ref.[118]

Figure 6.3 illustrates the relationship between illumination intensity in LUX and the power output μW/cm² for solar cells of varying thicknesses (80 μm, 100 μm, 135 μm, and 170 μm) under 4000K LED lighting. A clear linear relationship between illumination intensity and power output across all thicknesses is observed with the lines for different thicknesses being closely aligned. The inset, which zooms in on the indoor illumination range (250-500 LUX), however, shows a slightly higher power output for the 80 and 100 μm cells. The dashed line representing the maximum expected power output for a 1.8 μm solar cell, which is predicted to be the optimum thickness for indoor performance at 250 LUX under LED 2700K [118]. Even though the difference in color temperature result in slightly differing spectral characteristics, this comparison is conducted primarily to provide a general estimate of the deviation of the power output at different LUX levels of the studied wafer thickness from theoretical calculations at optimum thickness. The results show a relatively much higher power output for the predicted 1.8 μm cell compared to the studied cells. At 250 LUX, the 1.8 μm cell generates 22 μW/cm² of power, while the 80 μm cell produces 6.97 μW/cm², resulting in a difference of approximately 15 μW/cm². At 500 LUX, the difference between their power outputs increases to about 32 μW/cm². Despite this difference, the 80 μm cell may offer benefits in terms of easier integration with microelectronics and IoT devices due to its less fragility and the advantage of using an already established production process.

6.2. Summary

Solar cells can effectively harvest indoor light for low-power devices like IoT sensors, where illumination typically ranges from 250 to 500 LUX – much lower than outdoor levels. The spectrum of artificial light is more concentrated in the visible region, which makes thinner silicon wafers more desirable for efficient absorption. Experimental analysis of SHJ solar cells with thicknesses of 80 µm, 100 µm, 130 µm, and 170 µm under both solar and LED illumination revealed in general better open-circuit voltage, fill factor, and efficiency for 80 and 100 µm cells. Under lower light intensities, thinner cells generally exhibit slightly better efficiency, though the thicker cells show a higher short-circuit current density in higher light conditions. Although the 80 µm cells produce lower power output compared to the theoretically optimum 1.8 µm cell, they offer practical benefits due to their durability. However, thin-film solar cells, such as those based on amorphous silicon, perovskites, and organic materials, are better suited for indoor applications due to their wider bandgaps, which align more effectively with the spectra of LED and other indoor lighting.

7. Thin SHJ shingled mini modules

This chapter explores the development and optimization of mini-modules constructed from thin-wafer SHJ solar cells, with a focus on the transition from cell to module performance. Particular attention is given to the impact of wafer thickness on shingle mini-module performance and the potential for voltage adjustments in series-connected configurations, which are of interest in direct coupling with electrochemical devices at the lab scale.[160, 162] Small cells with thicknesses of 80 µm and 135 µm are utilized in the construction of shingle minimodules. In the first section of this chapter, the laser cutting parameters are optimized to reduce edge recombination especially I thinner cells which are more prone to microcracks. In the second part, the design of the contact grids on already existing cells is optimized to with focus on improving light absorption and reducing series resistance for better cell efficiency. In the final section, these improvements are then applied to the assembly of mini modules, where cells are soldered in configurations of 2, 3, 4, 5, 6, and 7 cells. The performance differences between the 80 µm and 135 µm thick modules are analyzed to assess the effect of cell thickness on the solar module parameters.

7.1. Laser-cutting optimization

The impact of laser cutting parameters on solar cell performance is crucial for optimizing efficiency, particularly in varying cell thicknesses. In this section, the influence of two different laser cutting parameter sets, ParA and ParB, on the performance of 80 µm and 135 µm thick solar cells was investigated. Table 7.1 shows the details of the laser cutting parameters for ParA and ParB, including cutting speed, laser power, pulse frequency, and the number of repetitions. Laser parameters ParA is the standard laser cutting parameter set in our lab for 135 µm solar cells which utilizes relatively high power, moderate speed, and a standard number of repetitions to ensure clean and precise cuts, particularly for thicker cells. In contrast, laser parameters ParB was designed with lower power, higher speed, and significantly more repetitions, with the aim of reducing edge damage and improving cut quality, especially in thinner cells which are more susceptible to damage.

Table 7.1: Laser cutting parameters

	Par A (standard)	**Par B**
Power [%]	65	55
Pulse-repetition frequency [MHz]	1	1
Speed [m/s]	0.20	1.00
Number of repetitions	15	200

Figure 7.1 shows the full wafer contact design with the specific areas that were cut using these parameters: the blue-outlined section was cut with laser cutting parameters, ParA, while the red-outlined section was cut with laser cutting parameters, ParB. Both parameter sets were applied to the same solar cells to allow for a direct comparison of their effects on key solar cell parameters.

Thin SHJ shingled mini modules

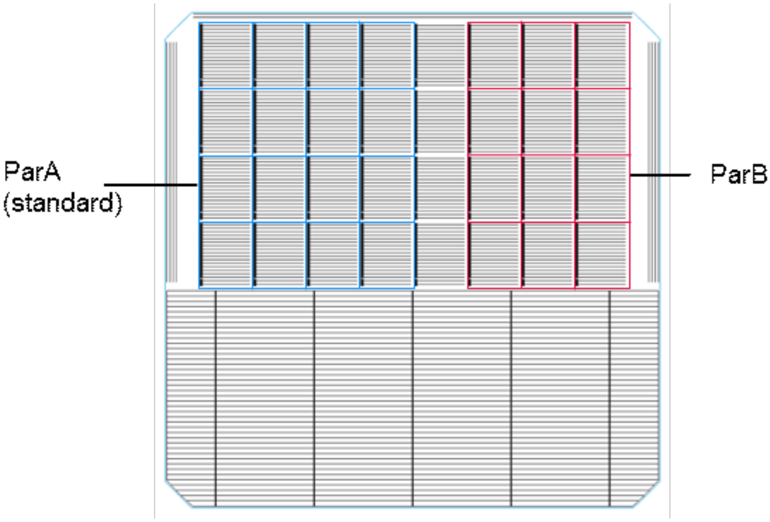

Figure 7.1: Schematic of the full wafer layout showing mini-cell segments used to compare the effects of two laser cutting parameter sets (ParA and ParB). The blue-outlined section (columns 1–4) was cut using the standard lab parameters (ParA), while the red-outlined section (columns 6–9) was cut using the modified parameters (ParB) optimized for thinner cells.

The performance of the solar cells after the cuts are presented in Figure 7.2. Laser cutting parameters, ParB demonstrated superior performance across several key solar cell parameters compared to ParA. Higher V_{OC} values were observed for both 80 µm and 135 µm cells with ParB, indicating that the combination of lower power, higher speed, and more repetitions effectively reduced edge defect-assisted recombination compared to ParA. This improvement in V_{OC} suggests a more efficient cutting process with fewer defects. Additionally, the *FF* improved with ParB, particularly for the 80 µm cells, due to increased shunt resistance which was notably lower with ParA. This enhanced shunt resistance with ParB contributed to better overall performance in the 80 µm cells.

Conversely, a reduction in J_{SC} was observed with laser cutting parameters, ParB for both cell thicknesses, indicating a potential trade-off between edge recombination and charge collection efficiency. The exact reason for the J_{SC} loss remains unclear. Interestingly, there was no significant effect on series resistance for either cell thickness with ParB. While there was no substantial improvement in overall efficiency for the 135 µm cells with ParB, significant gains were noted in the 80 µm cells. As a result, laser cutting parameters, ParB was selected for the cutting of cells used in the subsequent experimental sections.

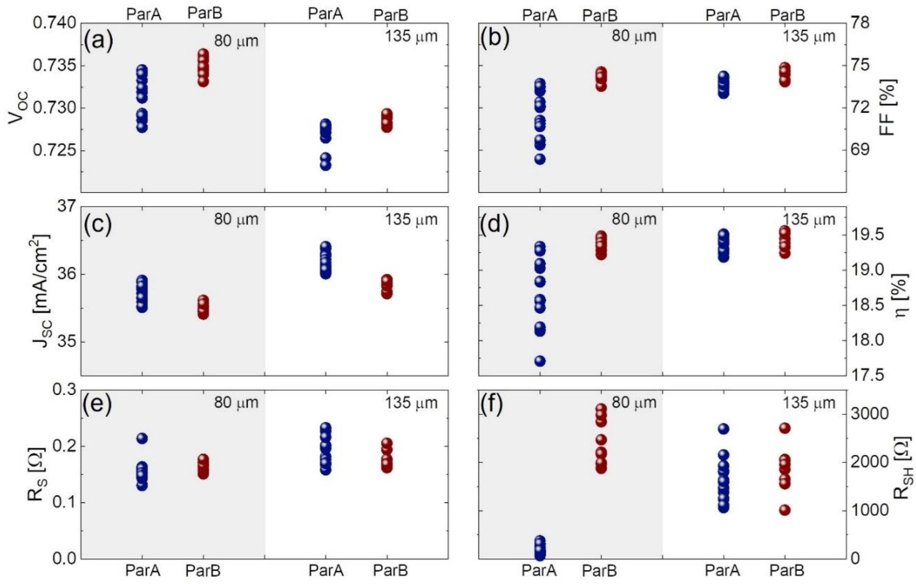

Figure 7.2: Effect of laser cutting parameters on solar cell performance for 80 µm and 135 µm wafers. Subplots show (a) open-circuit voltage, (b) fill factor, (c) short-circuit current density, (d) efficiency, (e) series resistance, and (f) shunt resistance for cells cut with parA(blue) and parB (red).

To further validate the electrical measurements, Figure 7.3 shows photoluminescence (PL) images of representative 80 µm and 135 µm SHJ solar cells cut using ParA and ParB. For each thickness, the left cell was cut with ParA and the right with ParB. The red arrows indicate regions of increased non-radiative recombination observed at the edges of cells cut with parameter A, likely due to laser-induced microcracks. In contrast, the 80 µm and 135 µm cells cut with ParB exhibit a more uniform PL intensity distribution, indicating less damage and better carrier lifetime near the edges.

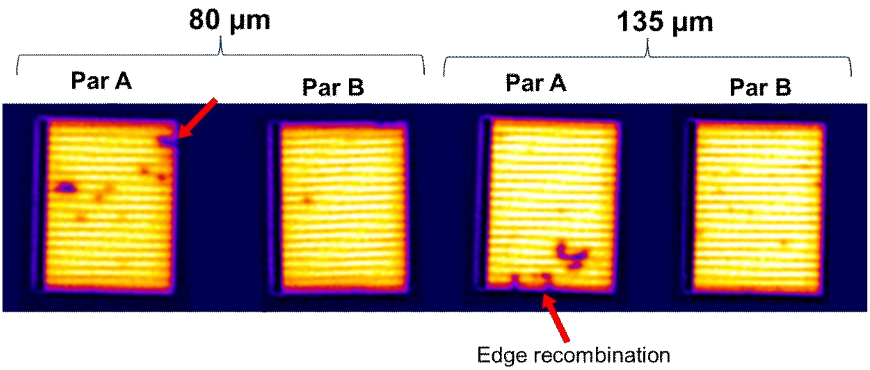

Figure 7.3: Photoluminescence images of representative 80 µm and 135 µm SHJ solar cells cut with laser parameters A and B, showing increased edge recombination in the cells cut with parameter A.

7.2. Optimization of metallization pattern for mini modules

In the design of small-sized cells, minimizing influences arising from contact shading and series resistance is essential to improving device efficiency. To address these challenges, a series of targeted modifications was made to the contact grid structure. The mini cells in this study are engineered for use in shingle modules, featuring a distinct busbar arrangement – positioned on the left side of the front and on the right side of the rear when viewed from the front. An optimization of the contact grids to maximize light absorption and minimize resistive losses is needed to optimize efficiency. Table 7.2 shows the modifications made on the cell grid design.

Table 7.2: Mini cell contact dimension modifications

	Front side		**Back side**	
	Grid design 1 (Reference)	Grid design 2	Grid design 1 (Reference)	Grid design 2
Number of fingers	18	15	18	18
Busbar thickness [mm]	1.00	0.70	1.00	0.70
Finger length [mm]	15.00	15.00	15.00	14.30
Cell dimension [mm^2]	17 x 21	16.5 x 21	17 x 21	16.5 x 21

For a clearer illustration of the design modifications, Figure 7.4 presents the schematic comparison between the original and modified contact grid layouts. The redesign of the front-side contact grid focused on two critical areas: the number of fingers and the busbar thickness. In the new design, the number of fingers was reduced from 18 (grid 1) to 15 (grid 2). Additionally, the busbar thickness was reduced from 1.00 mm to 0.70 mm. This reduction was intended to enhance light absorption by decreasing the shadowing effect caused by the fingers and busbar. With less fingers and thinner busbars, more light can reach the active area of the cell, potentially increasing J_{SC}. In addition, since the front contact shadowing leads to inhomogeneous generation of photocurrent, losses due to internal currents from the open regions with high generation to the shadowed regions under the metal contacts will be minimized.

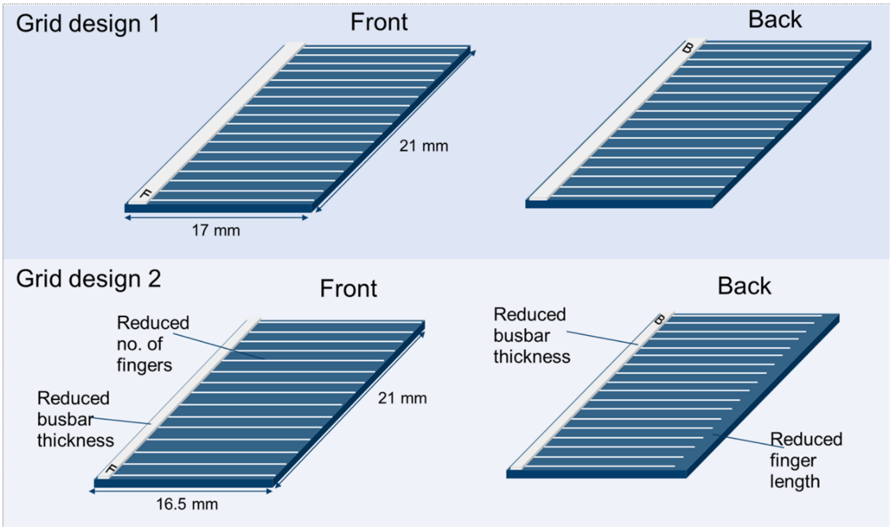

Figure 7.4: Schematic representation of the modification in contact grid design. Compared to the standard layout in grid design 1, grid design 2 features reduced busbar thickness, fewer front-side fingers, and shorter back-side fingers.

On the rear side, the length of the fingers was shortened from 15.00 mm (grid 1) to 14.30 mm (grid 2). This change was strategically implemented to prevent the fingers from extending into the area directly beneath the front-side busbar, where minimal charge carrier generation occurs. By reducing the unnecessary length of the fingers, series resistance is minimized, thereby improving overall cell efficiency. Finally, the width of the cells was reduced from 17 mm to 16.5 mm in the new design to fit the new busbar/finger dimensions.

Figure 7.5 shows the impact of the design changes on several critical solar cell parameters. The open-circuit voltage showed little to no improvements with the new grid design (grid 2) as seen in Figure 7.5(a). For the fill factor, a slight improvement most likely related to reduced series resistance with the new grid design was observed for both cell thicknesses, as depicted in Figure 7.5(b) where in both cases, a 2%$_{abs}$ increase between best cells is observed.

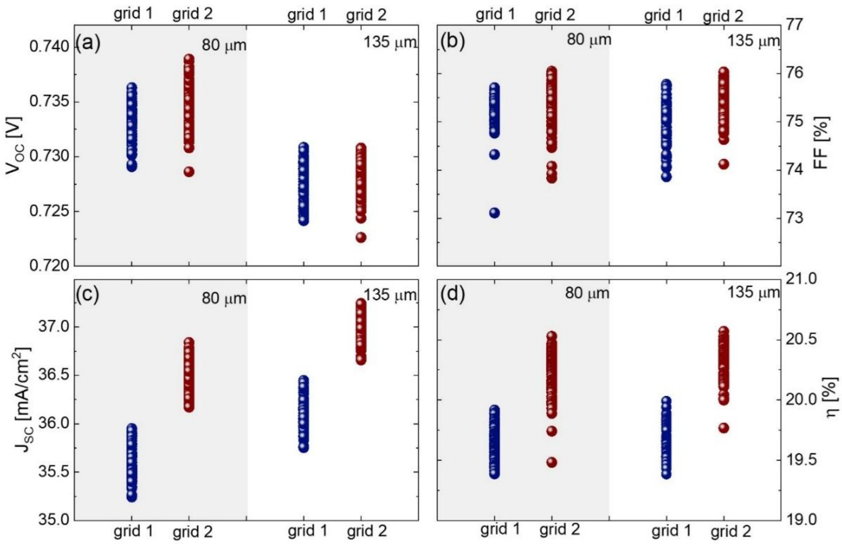

Figure 7.5: (a) Open-circuit voltage V_{OC}; (b) Fill factor *FF*; (c) short-circuit current density J_{SC}; and (d) efficiency η plotted for previous (grid 1) and new (grid 2) contact grid dimensions on cells of 80 and 135 µm wafer thicknesses.

Due to the decreased shadowing from fewer fingers and thinner busbars which allowed more light absorption, a remarkable increase in J_{SC} was also observed for both cell thicknesses in Figure 7.5(c). For the 135 µm cells, J_{SC} increased from 36.24 mA/cm^2 to around 37.16 mA/cm^2 while for the 80 µm cells, J_{SC} increased from 35.95 mA/cm^2 to around 36.79 mA/cm^2 for the best cells. The combined effects of increased charge carrier generation, lower series resistance, and enhanced light absorption resulted in higher conversion efficiencies for both cell thicknesses as shown Figure 7.5(d), where an increase of up to 0.6%$_{abs}$ was observed between best cells.

7.3. Shingled mini modules performance

Figure 7.6 shows the IV characteristics of the best performing modules made with 80 µm and 135 µm thick wafers, across configurations with 2 to 7 cells connected in series. As the number of cells increases, both the V_{OC} increases steadily, as expected, since more cells in series result in a higher overall voltage. In contrast, the I_{SC} remains nearly constant for the modules with the same wafer thickness, as the same current flows through all the cells in series. Comparing the two wafer thicknesses, the 135 µm wafers, as expected, produce slightly higher J_{SC} values due to improved light absorption. However, the V_{OC} for most module configurations remains similar between the two thicknesses. This suggests that any potential voltage gain from thinner wafers at the cell level is easily offset at the module level, likely due to additional recombination introduced during the soldering process.

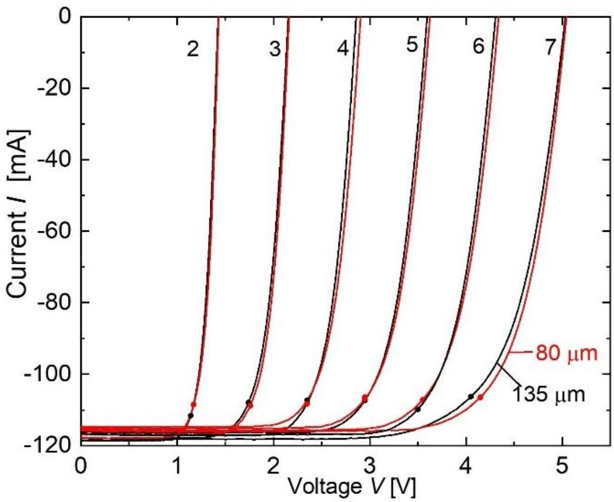

Figure 7.6: IV characteristics of the best performing 2-, 3-, 4-, 5-, 6-, and 7-cell modules with 80 µm (red) and 135 µm (black) wafer thicknesses. Red and black dots represent the maximum power points for the 80 and 135 µm modules, respectively

Figure 7.7 shows the effect of wafer thickness and module configuration on various solar cell parameters. As seen in Figure 7.7(a), there is very little difference between the V_{OC} and V_{MPP} of the 80 µm and 135 µm modules across all configurations. A uniform increase in V_{OC} of approximately 0.72 V and in V_{MPP} of approximately 0.60 V is observed as the number of cells increases. This consistent behavior leads to a higher deviation between V_{OC} and V_{MPP} as the number of cells increases. A relatively stable fill factor (*FF*) across cell configurations is observed in Figure 7.7(b), exhibiting only minor variations between the two wafer thicknesses. These variations are directly linked to the series resistance (R_S), which is influenced by the soldering process and shown in Figure 7.7(e).

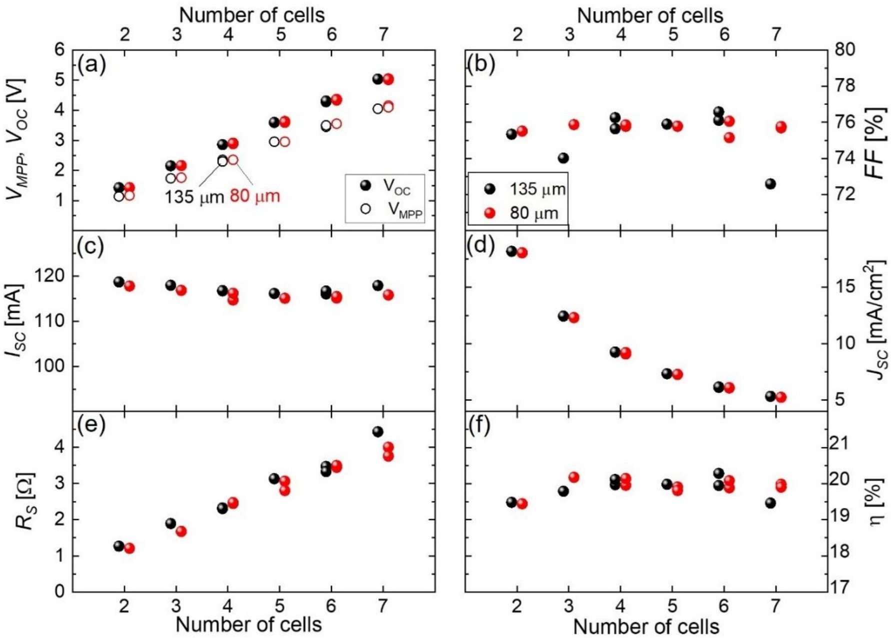

Figure 7.7: (a) Open-circuit voltage V_{OC} and maximum power point voltage V_{MPP}; (b) Fill factor *FF*; (c) short-circuit current I_{SC}; (d) short-circuit current density J_{SC}; (e) series resistance R_S and (f) efficiency η of modules of 2 to 7 number of cells with 80 µm and 135 µm wafer thickness.

As already observed in Figure 7.6, a relatively stable I_{SC} is observed across all module configurations as expected in series connected modules while a slightly lower I_{SC} is observed for the modules with thinner cells. This difference becomes even less significant when normalized to surface area, as shown by the J_{SC} in Figure 7.7(d). There is a consistent increase in R_S with the number of cells, which is observed in Figure 7.7(e) for both 135 µm and 80 µm wafers. This is expected due to the additional resistive losses introduced by interconnecting more cells. Final efficiency values in Figure 7.7(f) show no clear dependence on wafer thickness or the number of cells. This suggests that the impact of increased series resistance and potential additional recombination during the soldering process overshadows the intrinsic differences caused by wafer thickness. Thus, at the module level, thinner cells offer the advantage of material savings without compromising overall performance compared to thicker cells.

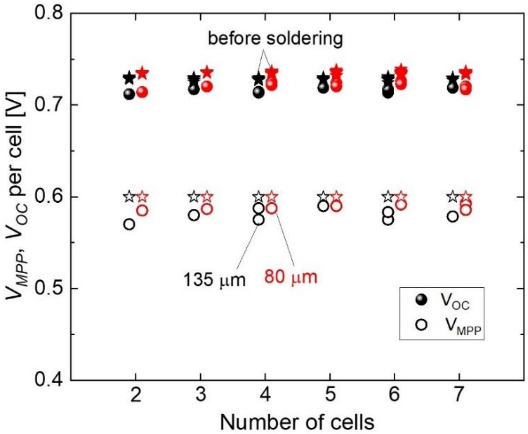

Figure 7.8: Open circuit voltage V_{OC} and voltage at maximum power point V_{MPP} per cell of the 80 µm and 135 µm cells / modules before (star) and after soldering (circle).

Figure 7.8 illustrates the V_{OC} and V_{MPP} of modules on a per-cell basis, calculated by dividing the total module voltage by the number of cells. These values are compared to the V_{OC} and V_{MPP} of individual cells before soldering. The V_{OC} and V_{MPP} of the individual cells before soldering are noticeably higher than the per-cell voltages of the soldered modules, highlighting the introduction of additional loss mechanisms, such as increased recombination and resistive losses, during the soldering process.

Regarding wafer thickness, the thinner 80 µm cells exhibit a higher V_{OC} both before and after soldering compared to the thicker 135 µm cells. This trend, while subtle at the module level as seen in Figure 7.7(a), becomes more pronounced when analyzed on a per-cell basis. Interestingly, the V_{MPP} of the individual cells before soldering is identical for both wafer thicknesses, despite the thinner cells having a higher Voc. This can be attributed to higher surface recombination on thinner cells, which is more prominent near the maximum power point (MPP) region, as discussed in Chapter 4. The per-cell V_{MPP}, however, becomes higher for the thinner 80 µm cells compared to the thicker cells after soldering. This shift suggests that the soldering process may have a more favorable impact on thinner cells, potentially due to lower resistive losses or better adaptation to the interconnection process.

7.4. Summary

In this chapter, the development and optimization of mini modules, focusing on the the influence of wafer thickness (80 µm vs. 135 µm) on the evolution of performance from individual cells to assembled modules were discussed. The laser cutting parameters were optimized to accommodate thinner cells without accruing losses for the thicker cells. Comparing two parameter sets, ParA and ParB, the latter proved more effective for 80 µm cells by using lower cutting power, higher speed, and increased repetitions. These adjustments led to higher V_{OC} and FF, attributed to reduced edge defects and increased shunt resistance.

Contact grid designs were also revised to improve efficiency by minimizing shading and resistive losses. The redesigned grid featured fewer fingers, thinner busbars, and optimized finger lengths, enhancing light absorption, reducing series resistance, and improving overall performance. The optimized design resulted in significant increases in V_{OC}, J_{SC}, and conversion efficiency, with the improvements being particularly pronounced for 80 µm cells.

The performance of shingle mini-modules with 80 µm and 135 µm wafer thicknesses was evaluated across 2 to 7-cell configurations. Increasing the number of cells consistently raised the V_{OC} while maintaining a stable J_{SC}. Thicker 135 µm wafers exhibited slightly higher J_{SC} due to better light absorption, but V_{OC} differences between the wafer thicknesses were minimal, suggesting recombination losses during soldering offset potential voltage gains of thinner wafers. Series resistance (R_S) increased with the number of cells, influenced by interconnection losses, while FF and efficiency remained relatively stable across configurations. On a per-cell basis, thinner 80 µm cells exhibited higher V_{OC} both before and after soldering, while the V_{MPP} was identical for cells of both wafer thicknesses before soldering. After soldering, however, modules made from thinner cells showed a higher V_{MPP}, indicating that the soldering process is more favorable for thinner cells, likely due to reduced resistive losses or improved interconnection efficiency. Overall, thinner wafers provide material savings without compromising module performance compared to thicker wafer.

8. Summary and Outlook

The urgency of addressing climate change has accelerated the global transition from fossil fuels to renewable energy sources, with photovoltaics (PV) emerging as the fastest-growing technology in this field. By 2023, PV systems accounted for three-quarters of newly installed renewable energy systems, highlighting their central role in meeting global climate goals. Among various PV technologies, crystalline silicon (c-Si) solar cells dominate the market due to their high efficiency, with silicon heterojunction (SHJ) solar cells demonstrating particularly great promise. The need for sustainable energy solutions necessitates strategies to reduce material usage, lower costs, and enhance the energy return on investment (ERoI). One such strategy involves reducing the thickness of silicon wafers, which are theoretically predicted to achieve high efficiencies. It becomes essential to experimentally investigate the viability of thin SHJ solar cells compared to their thicker counterparts and evaluate their performance across diverse scenarios. For example, given the ongoing transition toward perovskite/silicon tandem configurations, understanding the performance of thin SHJ cells as bottom cells is particularly important. Furthermore, assessing the potential of these thin cells under low light and LED illumination is essential for exploring their applications in indoor conditions. Finally, evaluating their performance evolution when soldered and integrated into modules is necessary to ensure their viability in practical applications.

A summary of the main results from each section is presented below, beginning with the effects of wafer thinning on single-junction SHJ solar cells, followed by their performance in various utilization scenarios.

Wafer thickness effect on:

Single junction SHJ solar cells: For this study**,** several SHJ solar cells of thicknesses ranging from 60 to 170 µm were prepared and analyzed. Carrier lifetime measurements showed that surface recombination dominates at lower carrier densities, particularly in thinner wafers, leading to reduced effective lifetime and gradual reductions in *iFF*. However, at higher carrier densities, solar cells transition to Auger recombination dominance, with implied open-circuit voltage iV_{OC} closely approaching theoretical limits. Finalized solar cells exhibited notable losses in *FF* and V_{OC} with reduced thickness due to contact shadowing and imperfect contact selectivity, while the J_{SC} decreased as expected from weaker long-wavelength absorption. Despite these challenges, high efficiencies were achieved across a thickness range of 75 - 170 µm, with a maximum efficiency of 22.3% at 75 µm, demonstrating the feasibility of wafer thinning without significant efficiency loss.

Tilt angle: Similar Voc dependence on tilt angle was observed, decreasing with decreased charge concentration resulting from reduced photon concentration at higher angles. While *FF* showed no clear correlation with thickness or tilt angle, J_{SC} and efficiency converged at angles above 30°, minimizing wafer thickness effects. The results indicate that J_{SC} losses in thinner cells under standard conditions are less significant in field conditions without solar trackers.

SHJ solar cells as bottom cells in PeroSi tandems: In this study, the performance of SHJ cells on 80 µm and 135 µm thick wafers as bottom cells in perovskite-silicon tandems was examined and compared to their performance under the standard AM1.5G. The analysis focused on two key aspects: passivation and light management.

- **Passivation:** The effect of enhanced passivation was investigated by increasing the passivation thickness on the front, rear, and both sides of SHJ solar cells. These modified cell variants were compared to those with the standard passivation thickness, which was optimized for standard light conditions. Under AM1.5G standard conditions, SHJ cells on 80 µm wafers showed a slight lower efficiency compared to 135 µm wafers, with peak efficiencies of 23.3% and 23.8%, respectively. While thicker passivation layers improved V_{OC}, implied and pseudo *FF*, they also increased series resistance and parasitic absorption, leading to losses in final *FF* and J_{SC}. However, under bottom cell conditions in tandems, series resistance effects are minimized. Measurements under perovskite-filtered spectrum and attenuated AM1.5G spectrum showed a higher J_{SC} under bottom cell conditions, indicating the effect of reduced parasitic absorption in the absence of short wavelength light. However, similar results for V_{OC}, *pFF*, and *FF* were obtained, indicating no spectral effects on these parameters. In terms of wafer thickness under the new spectrum, J_{SC} remained slightly lower in 80 µm cells due to higher transmission losses in infrared light. Despite a 40% wafer thickness reduction, efficiency dropped minimally (0.35%abs) under the perovskite-filtered spectrum, even without advanced light management.

- **Light management:** This study demonstrated that applying an ITO/MgF_2/Ag back reflector and a MgF_2 anti-reflection coating can reduce the J_{SC} gap between 80 µm and 135 µm SHJ solar cells. The most gain in J_{SC} after BR application is observed in the cells with the most near-IR losses, particularly the 80 µm cells, which gain up to 0.88 mA/cm² under AM1.5G and 0.58 mA/cm² under the perovskite-filtered spectrum. The 135 µm cells gain 0.73 mA/cm² and 0.52 mA/cm², respectively. After ARC deposition, all cells show an average gain of approximately 0.3 mA/cm² for both spectra.

SHJ solar cells in indoor conditions: The performance of SHJ solar cells of varying thicknesses (80 µm, 100 µm, 130 µm, and 170 µm) under low light and LED illumination was studied, specifically for indoor applications such as IoT devices. Indoor lighting, which typically ranges from 250 to 500 lux, requires solar cells with thinner wafers for better light absorption. The results showed that thinner cells (80 µm and 100 µm) generally perform better, with higher efficiency under lower light intensities compared to thicker cells. However, the power output for the studied cells is lower than the theoretically optimal 1.8 µm thickness for LED light harvesting. Thin-film solar cells, such as those made from amorphous silicon, perovskites, and organic materials, are more suitable for indoor use due to their wider bandgaps, which align better with artificial light spectra.

Mini modules fabrication and performance: The development and optimization of mini-modules made from thin-wafer SHJ solar cells is explored in this study, with a particular focus on how wafer thickness influences performance at both the cell and module levels. The study highlights the influence of laser cutting parameters, optimization of cell design, and the performance of shingle mini-modules constructed with 80 µm and 135 µm thick cells.

- **Laser cutting parameters:** The study investigated two laser cutting parameter sets (ParA and ParB) to optimize the cutting process for thinner cells. ParB, using lower power (55% vs. 65%), higher speed (1.00 m/s vs. 0.20 m/s), and more repetitions (200 vs. 15), significantly improved cell performance, particularly for 80 µm cells. ParB achieved higher V_{OC} and *FF* for both 80 µm and 135 µm cells compared to ParA. For 80 µm cells, ParA exhibited a broad range of low shunt resistance, while ParB stabilized it at higher, uniform values, leading to better *FF*. Although ParB caused a slight reduction in J_{SC} for both thicknesses, the improvements in V_{OC} and *FF* outweighed the loss, resulting in higher overall efficiencies for cells processed with ParB.

- **Cell Design Optimization:** The contact grid design for the cells was optimized to minimize shading and series resistance. The optimized design reduced the number of fingers from 18 to 15, and the busbar thickness was reduced from 1.00 mm to 0.70 mm to reduce optical losses due to shading. On the rear side, the finger length was also reduced from 15 mm to 14.3mm to reduce series resistance. For the 80 µm cells, the V_{OC} increased only slightly from 0.736 V to 0.739 V. The fill factor (FF) showed a 2% absolute increase between the best cells for both thicknesses. Additionally, J_{SC} increased significantly, with 80 µm cells showing an increase from 35.95 mA/cm² to 36.79 mA/cm², and 135 µm cells showing an increase from 36.24 mA/cm² to 37.16 mA/cm². The resulting efficiency improved by up to 0.6%$_{abs}$ for both thicknesses.

- **Mini Module Performance:** The performance of mini-modules made from 80 µm and 135 µm thick wafers was tested in configurations with 2 to 7 cells in series. As the number of cells increased, the voltages steadily increased, with a 0.72 V increase in V_{OC} and a 0.60 V increase in V_{MPP} observed across all configurations. While slightly lower J_{SC} was observed for the modules with 80 µm cells, the final efficiency (η) remained stable, with no clear dependence on wafer thickness or the number of cells, indicating that soldering losses and additional recombination during the process overshadowed the intrinsic differences between wafer thicknesses. The results suggest that thinner cells provide material savings without significant loss in module performance compared to thicker cells.

While the general effects of wafer thickness on solar cell performance are well understood, specific considerations remain critical for advancing this technology. One key challenge is stability, as thin wafers (<100 µm) are inherently fragile, making them prone to breakage during processing and handling. Optimized wafer handling techniques, including innovations in non-contact methods and soft handling systems, are necessary to ensure minimal losses in the production process. This stability challenge must be addressed to enable reliable and cost-effective manufacturing of thin-wafer cells.

Another important aspect requiring further research is the upscaling of <100 µm cells into larger module configurations. While small-scale modules in this thesis demonstrate promising efficiency, the metallization and encapsulation of these thin cells in larger modules pose challenges. Exploring innovative encapsulation materials and methods that provide mechanical support while maintaining high optical and electrical performance will be crucial. Additionally, for configurations like half-cut cells, further optimization of laser cutting techniques is needed to ensure precision and minimize defects, which can otherwise degrade cell performance. Addressing these aspects will be vital for realizing the commercial viability of thin-wafer solar cells in larger-scale applications

In the context of utilizing these cells as bottom cells, several optimization opportunities arise due to the absence of front-side parasitic absorption. For instance, the thickness of various layers within SHJ cells, such as the doped layers or the transparent conductive oxide (TCO), can be further optimized to enhance both contact selectivity and electrical conductivity. Additionally, alternative passivation layers, such as oxides, present promising avenues for exploration. To further improve the J_{SC} in thin wafers, implementing interdigitated back contact designs could be investigated, as they eliminate front-side contact shadowing.

Finally, to fully quantify the benefits (or losses) involved in transitioning towards thinner wafers, an in-depth cost analysis should be carried out. This analysis should take into account material savings, potential changes in manufacturing complexity, yield losses associated with handling thinner wafers, and the impact on cell efficiency and module performance. Additionally, considerations such as equipment modification costs, scalability of production, and long-term reliability of the thinner wafers should be factored into the evaluation. Such a comprehensive assessment would provide valuable insights into the economic viability of adopting ultra-thin wafer technologies.

A. Symbols and abbreviations

$\boldsymbol{A}$	Absorptance
$\boldsymbol{B}$	Radiative recombination coefficient
$\boldsymbol{C_n}$	Auger recombination coefficient for electrons
$\boldsymbol{C_p}$	Auger recombination coefficient for holes
$\boldsymbol{E_C}$	Conduction band edge
$\boldsymbol{E_F}$	Fermi energy level
$\boldsymbol{E_{FN}}$	Quasi-Fermi level for electrons
$\boldsymbol{E_{FP}}$	Quasi-Fermi level for holes
$\boldsymbol{E_T}$	Trap energy level
$\boldsymbol{E_V}$	Valence band edge
$\boldsymbol{G(t)}$	Carrier generation rate
$\boldsymbol{I_{SC}}$	Short-circuit current
$\boldsymbol{I_{MPP}}$	Current at maximum power point
$\boldsymbol{J}$	Current density
$\boldsymbol{J_{SC}}$	Short-circuit current density
$\boldsymbol{J_{MPP}}$	Current density at maximum power point
$\boldsymbol{J_{01}}$	Saturation current density of the first diode
$\boldsymbol{J_{02}}$	Saturation current density of the second diode
$\boldsymbol{J_L}$	Photogenerated current density
$\boldsymbol{J_{ph}}$	Photocurrent density
$\boldsymbol{J_{rec}}$	Recombination current density
$\boldsymbol{iJ}$	Implied current density
$\boldsymbol{iJ_{SC}}$	Implied short-circuit current density
$\boldsymbol{iJ_{MPP}}$	Implied current density at maximum power point
$\boldsymbol{P_{in}}$	Input power density

Symbols and abbreviations

P_{MPP}	Maximum power density
R	Reflectance
R_S	Series resistance
R_{SH}	Shunt resistance
R_{intr}	Intrinsic recombination rate
R_{rad}	Radiative recombination rate
R_{SRH}	Shockley–Read–Hall recombination rate
S	Surface recombination velocity
σ_n	Electron recombination cross-section
σ_p	Hole recombination cross-section
T	Temperature
V	Voltage
V_{OC}	Open-circuit voltage
V_{MPP}	Voltage at maximum power point
W	Wafer thickness
Δn	Excess carrier concentration
η	Power conversion efficiency
λ	Wavelength
τ_{Auger}	Auger recombination lifetime
τ_b	Bulk carrier lifetime
τ_{eff}	Effective carrier lifetime
τ_{intr}	Intrinsic carrier lifetime
τ_{rad}	Radiative recombination lifetime
n	Electron concentration
n_i	Intrinsic carrier concentration
n_{id}	Ideality factor
N_A	Acceptor dopant concentration
N_D	Donor dopant concentration
p	Hole concentration
k_B	Boltzmann constant
φ	Luminous flux
a-Si:H	Hydrogenated amorphous silicon
c-Si	Crystalline silicon

Symbols and abbreviations

CdTe	Cadmium telluride
CIGS	Copper indium gallium selenide
MgF_2	Magnesium fluoride
In_2O_3	Indium oxide
SnO_2	Tin oxide
ZnO	Zinc oxide
H_2	Hydrogen
SiH_4	Silane
PH_3	Phosphine
B_2H_6	Diborane
HCl	Hydrochloric acid
HF	Hydrofluoric acid
H_2O	Water
O_3	Ozone
SF_6/O_2	Sulfur hexafluoride/oxygen
$Sn_{42}Bi_{57}Ag_1$	Tin–bismuth–silver solder alloy
AM1.5G	Air Mass 1.5 Global
ARC	Anti-reflection coating
AZO	Aluminium-doped zinc oxide
BGN	Band gap narrowing
CIE	Commission Internationale de l'Éclairage
CVD	Chemical vapor deposition
DC	Direct current
DLARC	Double-layer anti-reflection coating
EQE	External quantum efficiency
ERoI	Energy return on investment
ETC	Effectively transparent contacts
FCA	Free carrier absorption
FF	Fill factor
FWHM	Full width at half maximum
GM.QE	Grating Monochromator Quantum Efficiency
IBC	Interdigitated back contact
IoT	Internet of Things

IQE	Internal quantum efficiency
IR	Infrared
IRENA	International Renewable Energy Agency
ITO	Indium tin oxide
IV	Current–voltage
JV	Current density–voltage
LED	Light-emitting diode
LID	Light-induced degradation
LOANA	Solar cell analysis system
MPP	Maximum power point
PECVD	Plasma-enhanced chemical vapor deposition
PERC	Passivated emitter and rear cell
PL	Photoluminescence
PM	Process module
PV	Photovoltaics
QE	Quantum efficiency
QDR	Quick dump rinser
QSSPC	Quasi-steady-state photoconductance
SDR	Saw damage removal
SEM	Scanning electron microscopy
SHJ	Silicon heterojunction
SRH	Shockley–Read–Hall
TCO	Transparent conductive oxide
UV	Ultraviolet

B. List of Publications

1. **Chime, U.**, Duan, W., Lambertz, A., Bittkau, K., Lauterbach, V., Ding, K., Rau, U., Merdzhanova, T. and Astakhov, O. (2024) *'Thin silicon heterojunction solar cells in perovskite shadow: Bottom cell prospective'*, Solar Energy Materials and Solar Cells, 270, 112813.
2. **Chime, U.**, Wolf, L., Buga, V., Weigand, D., Gad, A., Köhler, J., Lambertz, A., Duan, W., Ding, K., Merdzhanova, T., Rau, U and Astakhov, O. (2022) *'How Thin Practical Silicon Heterojunction Solar Cells Could Be? Experimental Study under 1 Sun and under Indoor Illumination'*, Solar RRL, 6(1), 2100594.
3. Shcherbachenko, S., Astakhov, O., **Chime, U.**, Kin, L.-C., Ding, K., Pieters, B., Rau, U., Figgemeier, E. and Merdzhanova, T. (2023) *'Efficient Power Coupling in Directly Connected Photovoltaic-Battery Module'*, Solar RRL, 7(3), 2200857.
4. Ampelli, C., Giusi, D., Miceli, M., Merdzhanova, T., Smirnov, V., **Chime, U.**, Astakhov, O., Martín, A. J., Veenstra, F. L. P. and Pineda, F. A. G. (2023) *'An artificial leaf device built with earth-abundant materials for combined H 2 production and storage as formate with efficiency> 10%'*, Energy & Environmental Science, 16(4), 1644-1661.

C. Curriculum Vitae

29.05.2026	Doctoral Examination for Dr. rer. nat. RWTH Aachen University, Germany
2020–2025	Doctoral Researcher Forschungszentrum Jülich GmbH Institute of Energy Materials and Devices – Photovoltaics (IMD-3) RWTH Aachen University, Germany
2012–2013	Master of Science in Renewable Energy Engineering Heriot-Watt University, Edinburgh, United Kingdom
2005–2010	Bachelor of Science in Physics and Astronomy University of Nigeria, Nsukka, Nigeria
1998-2004	Federal Government College, Enugu, Nigeria West African Senior School Certificate Examination (WASSCE)

References

[1] International Energy Agency *Renewables 2023: Analysis and forecast to 2028*, 2023.

[2] COP28, IRENA, and GRA, *Tripling renewable power and doubling energy efficiency by 2030: Crucial steps towards 1.5°C*, , International Renewable Energy Agency, Abu Dhabi., 2023.

[3] J. Ramanujam, D. M. Bishop, T. K. Todorov, O. Gunawan, J. Rath, R. Nekovei, E. Artegiani, and A. Romeo, "Flexible CIGS, CdTe and a-Si: H based thin film solar cells: A review," *Progress in Materials Science,* vol. 110, pp. 100619, 2020.

[4] P. Zhu, C. Chen, J. Dai, Y. Zhang, R. Mao, S. Chen, J. Huang, and J. Zhu, "Toward the commercialization of perovskite solar modules," *Advanced Materials,* vol. 36, no. 15, pp. 2307357, 2024.

[5] S. R. Golroudbary, M. Lundström, and B. P. Wilson, "Analogical environmental cost assessment of silicon flows used in solar panels by the US and China," *Scientific Reports,* vol. 14, no. 1, pp. 9538, 2024.

[6] M. Hermle, F. Feldmann, M. Bivour, J. C. Goldschmidt, and S. W. Glunz, "Passivating contacts and tandem concepts: Approaches for the highest silicon-based solar cell efficiencies," *Applied Physics Reviews,* vol. 7, no. 2, 2020.

[7] G. M. Wilson, M. Al-Jassim, W. K. Metzger, S. W. Glunz, P. Verlinden, G. Xiong, L. M. Mansfield, B. J. Stanbery, K. Zhu, and Y. Yan, "The 2020 photovoltaic technologies roadmap," *Journal of Physics D: Applied Physics,* vol. 53, no. 49, pp. 493001, 2020.

[8] LONGi. "LONGi Sets New World-Record for Silicon Solar Cell Efficiency, Launching 2nd Generation Ultra-Efficient BC-Based Module," 08/07/2024); https://www.longi.com/en/news/longi-hi-mo9-bc-world-record/.

[9] Fraunhofer Institute for Solar Energy Systems "Photovoltaics Report," 04/05, 2023; https://www.ise.fraunhofer.de/content/dam/ise/de/documents/publications/studies/Photovoltaics-Report.pdf.

[10] A. Richter, M. Hermle, and S. W. Glunz, "Reassessment of the limiting efficiency for crystalline silicon solar cells," *IEEE journal of photovoltaics,* vol. 3, no. 4, pp. 1184-1191, 2013.

[11] B. A. Veith-Wolf, S. Schäfer, R. Brendel, and J. Schmidt, "Reassessment of intrinsic lifetime limit in n-type crystalline silicon and implication on maximum solar cell efficiency," *Solar Energy Materials and Solar Cells,* vol. 186, pp. 194-199, 2018.

[12] M. J. Kerr, and A. Cuevas, "General parameterization of Auger recombination in crystalline silicon," *Journal of Applied Physics,* vol. 91, no. 4, pp. 2473-2480, 2002.

[13] European Commission "European Critical Raw Materials Act," March 21, 2023; https://single-market-economy.ec.europa.eu/publications/european-critical-raw-materials-act_en.

[14] L. Carton, R. Riva, D. Nelias, M. Fourmeau, F. Coustier, and A. Chabli, "Comparative analysis of mechanical strength of diamond-sawn silicon wafers depending on saw mark orientation, crystalline nature and thickness," *Solar Energy Materials and Solar Cells,* vol. 201, pp. 110068, 2019/10/01/, 2019.

[15] R. Rao, L. Mathew, D. Sarkar, S. Smith, S. Saha, R. Garcia, R. Stout, A. Gurmu, M. Ainom, and E. Onyegam, "A low cost kerfless thin crystalline Si solar cell technology." pp. 001837-001840.

[16] J. H. Petermann, D. Zielke, J. Schmidt, F. Haase, E. G. Rojas, and R. Brendel, "19%-efficient and 43 µm-thick crystalline Si solar cell from layer transfer using porous silicon," *Progress in Photovoltaics: Research and Applications,* vol. 20, no. 1, pp. 1-5, 2012.

[17] C. W. Chen, R. Hao, V. D. Upadhyaya, T. Ravi, and A. Rohatgi, "Development of high-efficiency large-area screen-printed solar cells on direct kerfless epitaxially grown monocrystalline Si wafer and structure," *Progress in Photovoltaics: Research and Applications,* vol. 24, no. 8, pp. 1133-1141, 2016.

[18] Y. Li, X. Ru, M. Yang, Y. Zheng, S. Yin, C. Hong, F. Peng, M. Qu, C. Xue, and J. Lu, "Flexible silicon solar cells with high power-to-weight ratios," *Nature,* vol. 626, no. 7997, pp. 105-110, 2024.

[19] A. K. Shukla, K. Sudhakar, and P. Baredar, “Recent advancement in BIPV product technologies: A review,” *Energy and Buildings,* vol. 140, pp. 188-195, 2017.

[20] Y. Ohshita, K. Onishi, R. Yokogawa, T. Nishihara, T. Kamioka, K. Nakamura, T. Kawatsu, T. Nagai, N. Yamada, and Y. Miyashita, "Ultra-Thin Lightweight Bendable Crystalline Si Solar Cells for Solar Vehicles." pp. 1131-1134.

[21] L. C. Andreani, A. Bozzola, P. Kowalczewski, M. Liscidini, and L. Redorici, “Silicon solar cells: toward the efficiency limits,” *Advances in Physics: X,* vol. 4, no. 1, pp. 1548305, 2019.

[22] A. Augusto, E. Looney, C. Del Canizo, S. G. Bowden, and T. Buonassisi, “Thin silicon solar cells: Pathway to cost-effective and defect-tolerant cell design,” *Energy Procedia,* vol. 124, pp. 706-711, 2017.

[23] A. Razzaq, T. G. Allen, W. Liu, Z. Liu, and S. De Wolf, “Silicon heterojunction solar cells: Techno-economic assessment and opportunities,” *Joule,* vol. 6, no. 3, pp. 514-542, 2022.

[24] J. L. Gray, "The Physics of the Solar Cell," *Handbook of Photovoltaic Science and Engineering*, pp. 61-112, 2003.

[25] J. Chen, "Semiconductor Solar Cells," *Physics of Solar Energy*, pp. 177-210, 2011.

[26] P. Wurfel, "Semiconductors," *Physics of Solar Cells*, pp. 37-84, 2005.

[27] A. Smets, Jäger, K., Isabella, O., Swaaj, R.V. and Zeman, M, *Solar Energy: The Physics and Engineering of Photovoltaic Conversion Technologies and Systems*, England: UIT Cambridge Ltd., 2016.

[28] J. Chen, "PN-Junctions," *Physics of Solar Energy*, pp. 161-176: John Wiley & Sons, Inc., 2011.

[29] L. Zhe, “Optical loss analysis of silicon wafer based solar cells and modules,” National University of Singapore (Singapore), 2016.

[30] R. Saive, “Light trapping in thin silicon solar cells: A review on fundamentals and technologies,” *Progress in Photovoltaics: Research and Applications,* vol. 29, no. 10, pp. 1125-1137, 2021.

[31] K. Yoshikawa, H. Kawasaki, W. Yoshida, T. Irie, K. Konishi, K. Nakano, T. Uto, D. Adachi, M. Kanematsu, and H. Uzu, “Silicon heterojunction solar cell with interdigitated back contacts for a photoconversion efficiency over 26%,” *Nature energy,* vol. 2, no. 5, pp. 1-8, 2017.

[32] J.-F. Guillemoles, T. Kirchartz, D. Cahen, and U. Rau, "Guide for the perplexed to the Shockley–Queisser model for solar cells," *Nature photonics,* vol. 13, no. 8, pp. 501-505, 2019.

[33] M. Futscher, and B. Ehrler, "Efficiency limit of Perovskite/Si tandem solar cells. ACS Energy Lett 1: 863–868," 2016.

[34] B. M. Kayes, L. Zhang, R. Twist, I.-K. Ding, and G. S. Higashi, "Flexible thin-film tandem solar cells with> 30% efficiency," *IEEE Journal of Photovoltaics,* vol. 4, no. 2, pp. 729-733, 2014.

[35] T. P. White, N. N. Lal, and K. R. Catchpole, "Tandem solar cells based on high-efficiency c-Si bottom cells: top cell requirements for> 30% efficiency," *IEEE Journal of Photovoltaics,* vol. 4, no. 1, pp. 208-214, 2013.

[36] H. Heidarzadeh, A. Rostami, and M. Dolatyari, "Management of losses (thermalization-transmission) in the Si-QDs inside 3C–SiC to design an ultra-high-efficiency solar cell," *Materials Science in Semiconductor Processing,* vol. 109, pp. 104936, 2020.

[37] B. S. Richards, A. Ivaturi, S. K. MacDougall, and J. Marques-Hueso, "Up-and down-conversion materials for photovoltaic devices." pp. 11-18.

[38] Y. Zhang, X. Jia, S. Liu, B. Zhang, K. Lin, J. Zhang, and G. Conibeer, "A review on thermalization mechanisms and prospect absorber materials for the hot carrier solar cells," *Solar Energy Materials and Solar Cells,* vol. 225, pp. 111073, 2021.

[39] M. Diantoro, T. Suprayogi, A. Hidayat, A. Taufiq, A. Fuad, and R. Suryana, "Shockley's Equation Fit Analyses for Solar Cell Parameters from I-V Curves," *International Journal of Photoenergy,* vol. 2018, no. 1, pp. 9214820, 2018.

[40] G. E. Bunea, K. E. Wilson, Y. Meydbray, M. P. Campbell, and D. M. De Ceuster, "Low light performance of mono-crystalline silicon solar cells." pp. 1312-1314.

[41] S. Suckow, T. M. Pletzer, and H. Kurz, "Fast and reliable calculation of the two-diode model without simplifications," *Progress in photovoltaics: research and applications,* vol. 22, no. 4, pp. 494-501, 2014.

[42] A. Sproul, "Dimensionless solution of the equation describing the effect of surface recombination on carrier decay in semiconductors," *Journal of Applied Physics,* vol. 76, no. 5, pp. 2851-2854, 1994.

[43] W. Shockley, and W. T. Read, “Statistics of the Recombinations of Holes and Electrons,” *Physical Review,* vol. 87, no. 5, pp. 835-842, 1952.

[44] R. N. Hall, “Electron-Hole Recombination in Germanium,” *Physical Review,* vol. 87, no. 2, pp. 387-387, 1952.

[45] R. Stangl, M. Kriegel, and M. Schmidt, "AFORS-HET, Version 2.2, a numerical computer program for simulation of heterojunction solar cells and measurements." pp. 1350-1353.

[46] R. Müller, P. Kanschat, S. Von Aichberger, K. Lips, and W. Fuhs, “Identification of transport and recombination paths in homo-and heterojunction silicon solar cells by electrically detected magnetic resonance,” *Journal of Non-Crystalline Solids,* vol. 266, pp. 1124-1128, 2000.

[47] T. Kirchartz, F. Deledalle, P. S. Tuladhar, J. R. Durrant, and J. Nelson, “On the differences between dark and light ideality factor in polymer: fullerene solar cells,” *The Journal of Physical Chemistry Letters,* vol. 4, no. 14, pp. 2371-2376, 2013.

[48] R. A. Sinton, A. Cuevas, and M. Stuckings, "Quasi-steady-state photoconductance, a new method for solar cell material and device characterization." pp. 457-460.

[49] W. Fuhs, K. Niemann, and J. Stuke, "Heterojunctions of amorphous silicon and silicon single crystals." pp. 345-350.

[50] J. Pankove, and M. Tarng, “Amorphous silicon as a passivant for crystalline silicon,” *Applied Physics Letters,* vol. 34, no. 2, pp. 156-157, 1979.

[51] Y. Hamakawa, K. Fujimoto, K. Okuda, Y. Kashima, S. Nonomura, and H. Okamoto, “New types of high efficiency solar cells based on a-Si,” *Applied Physics Letters,* vol. 43, no. 7, pp. 644-646, 1983.

[52] H. Matsuura, A. Matsuda, H. Okushi, T. Okuno, and K. Tanaka, “Metal-semiconductor junctions and amorphous-crystalline heterojunctions using B-doped hydrogenated amorphous silicon,” *Applied physics letters,* vol. 45, no. 4, pp. 433-435, 1984.

[53] M. Tanaka, M. Taguchi, T. Matsuyama, T. Sawada, S. Tsuda, S. Nakano, H. Hanafusa, and Y. Kuwano, “Development of new a-Si/c-Si heterojunction solar cells: ACJ-HIT (artificially constructed junction-heterojunction with intrinsic thin-layer),” *Japanese journal of applied physics,* vol. 31, no. 11R, pp. 3518, 1992.

[54] M. Tanaka, S. Okamoto, S. Tsuge, and S. Kiyama, "Development of HIT solar cells with more than 21% conversion efficiency and commercialization of highest performance HIT modules." pp. 955-958.

[55] L. Korte, E. Conrad, H. Angermann, R. Stangl, and M. Schmidt, "Advances in a-Si: H/c-Si heterojunction solar cell fabrication and characterization," *Solar Energy Materials and Solar Cells,* vol. 93, no. 6-7, pp. 905-910, 2009.

[56] K. Yamamoto, K. Yoshikawa, H. Uzu, and D. Adachi, "High-efficiency heterojunction crystalline Si solar cells," *Japanese Journal of Applied Physics,* vol. 57, no. 8S3, pp. 08RB20, 2018, 2018.

[57] D. Adachi, J. L. Hernández, and K. Yamamoto, "Impact of carrier recombination on fill factor for large area heterojunction crystalline silicon solar cell with 25.1% efficiency," *Applied Physics Letters,* vol. 107, no. 23, 2015.

[58] A. Descoeudres, Z. C. Holman, L. Barraud, S. Morel, S. De Wolf, and C. Ballif, "> 21% efficient silicon heterojunction solar cells on n-and p-type wafers compared," *IEEE Journal of Photovoltaics,* vol. 3, no. 1, pp. 83-89, 2012.

[59] T. Niewelt, J. Schön, W. Warta, S. W. Glunz, and M. C. Schubert, "Degradation of crystalline silicon due to boron–oxygen defects," *IEEE Journal of Photovoltaics,* vol. 7, no. 1, pp. 383-398, 2016.

[60] D. Macdonald, and L. Geerligs, "Recombination activity of interstitial iron and other transition metal point defects in p-and n-type crystalline silicon," *Applied Physics Letters,* vol. 85, no. 18, pp. 4061-4063, 2004.

[61] M. Moreno, D. Murias, J. Martínez, C. Reyes-Betanzo, A. Torres, R. Ambrosio, P. Rosales, P. R. i Cabarrocas, and M. Escobar, "A comparative study of wet and dry texturing processes of c-Si wafers for the fabrication of solar cells," *Solar Energy,* vol. 101, pp. 182-191, 2014.

[62] S. P. Muduli, and P. Kale, "State-of-the-art passivation strategies of c-Si for photovoltaic applications: A review," *Materials Science in Semiconductor Processing,* vol. 154, pp. 107202, 2023.

[63] R. S. Bonilla, and P. R. Wilshaw, "A technique for field effect surface passivation for silicon solar cells," *Applied Physics Letters,* vol. 104, no. 23, 2014.

[64] S. De Wolf, A. Descoeudres, Z. C. Holman, and C. Ballif, "High-efficiency silicon heterojunction solar cells: A review," *green,* vol. 2, no. 1, pp. 7-24, 2012, 2012.

[65] J.-W. A. Schüttauf, K. H. van der Werf, I. M. Kielen, W. G. van Sark, J. K. Rath, and R. E. Schropp, "Excellent crystalline silicon surface passivation by amorphous silicon irrespective of the technique used for chemical vapor deposition," *Applied physics letters,* vol. 98, no. 15, 2011.

[66] J. Panigrahi, and V. K. Komarala, "Progress on the intrinsic a-Si: H films for interface passivation of silicon heterojunction solar cells: A review," *Journal of Non-Crystalline Solids,* vol. 574, pp. 121166, 2021.

[67] A. Kanevce, and W. K. Metzger, "The role of amorphous silicon and tunneling in heterojunction with intrinsic thin layer (HIT) solar cells," *Journal of Applied Physics,* vol. 105, no. 9, pp. 094507, 2009.

[68] W. Duan, A. Lambertz, K. Bittkau, D. Qiu, K. Qiu, U. Rau, and K. Ding, "A route towards high-efficiency silicon heterojunction solar cells," *Progress in Photovoltaics: Research and Applications,* vol. 30, no. 4, pp. 384-392, 2022.

[69] H. A. Gatz, D. Koushik, J. K. Rath, W. M. Kessels, and R. E. Schropp, "Atomic layer deposited ZnO: B as transparent conductive oxide for increased short circuit current density in silicon heterojunction solar cells," *Energy procedia,* vol. 92, pp. 624-632, 2016.

[70] Y. Kuang, B. Macco, B. Karasulu, C. K. Ande, P. C. Bronsveld, M. A. Verheijen, Y. Wu, W. M. Kessels, and R. E. Schropp, "Towards the implementation of atomic layer deposited In2O3: H in silicon heterojunction solar cells," *Solar Energy Materials and Solar Cells,* vol. 163, pp. 43-50, 2017.

[71] Q. Tang, W. Duan, A. Lambertz, K. Bittkau, M. A. Yaqin, Y. Zhao, K. Zhang, Q. Yang, D. Qiu, and F. Gunkel, "> 85% indium reduction for high-efficiency silicon heterojunction solar cells with aluminum-doped zinc oxide contacts," *Solar Energy Materials and Solar Cells,* vol. 251, pp. 112120, 2023.

[72] G. T. Chavan, Y. Kim, M. Q. Khokhar, S. Q. Hussain, E.-C. Cho, J. Yi, Z. Ahmad, P. Rosaiah, and C.-W. Jeon, "A brief review of transparent conducting oxides (TCO): the influence of different deposition techniques on the efficiency of solar cells," *Nanomaterials,* vol. 13, no. 7, pp. 1226, 2023.

[73] S. Li, M. Pomaska, A. Lambertz, W. Duan, K. Bittkau, D. Qiu, Z. Yao, M. Luysberg, P. Steuter, and M. Köhler, "Transparent-conductive-oxide-free front contacts for

high-efficiency silicon heterojunction solar cells," *Joule,* vol. 5, no. 6, pp. 1535-1547, 2021.

[74] G. D. Obikoya, A. Soman, U. K. Das, and S. S. Hegedus, "Role of back-side indium tin oxide on the degradation mechanism of silicon heterojunction solar cells." pp. 0570-0573.

[75] B. O'Sullivan, T. Bearda, S. Nadupalli, R. Labie, K. Baert, I. Gordon, and J. Poortmans, "Process-Induced Degradation of SiO_2 and a-Si: H Passivation Layers for Photovoltaic Applications," *IEEE Journal of Photovoltaics,* vol. 4, no. 5, pp. 1197-1203, 2014.

[76] A. Eberst, A. Zamchiy, K. Qiu, P. Winkel, H. T. Gebrewold, A. Lambertz, W. Duan, S. Li, K. Bittkau, and T. Kirchartz, "Optical Optimization Potential of Transparent-Passivated Contacts in Silicon Solar Cells," *Solar RRL,* vol. 6, no. 6, pp. 2101050, 2022.

[77] F.-J. Haug, T. Söderström, O. Cubero, V. Terrazzoni-Daudrix, and C. Ballif, "Plasmonic absorption in textured silver back reflectors of thin film solar cells," *Journal of Applied Physics,* vol. 104, no. 6, 2008.

[78] R. Brendel, and H. Queisser, "On the thickness dependence of open circuit voltages of pn junction solar cells," *Solar energy materials and solar cells,* vol. 29, no. 4, pp. 397-401, 1993.

[79] E. Yablonovitch, "Statistical ray optics," *JOSA,* vol. 72, no. 7, pp. 899-907, 1982.

[80] W. Shockley, and H. J. Queisser, "Detailed balance limit of efficiency of p-n junction solar cells," *Journal of applied physics,* vol. 32, no. 3, pp. 510-519, 1961.

[81] M. A. Green, "Limits on the open-circuit voltage and efficiency of silicon solar cells imposed by intrinsic Auger processes," *IEEE Transactions on electron devices,* vol. 31, no. 5, pp. 671-678, 1984.

[82] T. Tiedje, E. Yablonovitch, G. D. Cody, and B. G. Brooks, "Limiting efficiency of silicon solar cells," *IEEE Transactions on electron devices,* vol. 31, no. 5, pp. 711-716, 1984.

[83] M. J. Kerr, A. Cuevas, and P. Campbell, "Limiting efficiency of crystalline silicon solar cells due to Coulomb-enhanced Auger recombination," *Progress in Photovoltaics: Research and Applications,* vol. 11, no. 2, pp. 97-104, 2003.

[84] P. Altermatt, F. Geelhaar, T. Trupke, X. Dai, A. Neisser, and E. Daub, "Injection dependence of spontaneous radiative recombination in crystalline silicon: Experimental verification and theoretical analysis," *Applied physics letters,* vol. 88, no. 26, pp. 261901, 2006.

[85] A. Richter, S. W. Glunz, F. Werner, J. Schmidt, and A. Cuevas, "Improved quantitative description of Auger recombination in crystalline silicon," *Physical review B,* vol. 86, no. 16, pp. 165202, 2012.

[86] International Electrotechnical Commission "Photovoltaic devices—Part 3: measurement principles for terrestrial photovoltaic (PV) solar devices with reference spectral irradiance data," *IEC 60904–3 ed2*, 2008.

[87] M. A. Green, "Self-consistent optical parameters of intrinsic silicon at 300 K including temperature coefficients," *Solar Energy Materials and Solar Cells,* vol. 92, no. 11, pp. 1305-1310, 2008.

[88] M. Rüdiger, J. Greulich, A. Richter, and M. Hermle, "Parameterization of free carrier absorption in highly doped silicon for solar cells," *IEEE Transactions on Electron Devices,* vol. 60, no. 7, pp. 2156-2163, 2013.

[89] A. Schenk, "Finite-temperature full random-phase approximation model of band gap narrowing for silicon device simulation," *Journal of Applied Physics,* vol. 84, no. 7, pp. 3684-3695, 1998.

[90] M. A. Green, "Solar cell fill factors: General graph and empirical expressions," *Solid-State Electronics,* vol. 24, no. 8, pp. 788-789, 1981/08/01/, 1981.

[91] M. Leilaeioun, and Z. C. Holman, "Accuracy of expressions for the fill factor of a solar cell in terms of open-circuit voltage and ideality factor," *Journal of Applied Physics,* vol. 120, no. 12, pp. 123111, 2016.

[92] P. Kowalczewski, and L. C. Andreani, "Towards the efficiency limits of silicon solar cells: How thin is too thin?," *Solar Energy Materials and Solar Cells,* vol. 143, pp. 260-268, 2015.

[93] P. Campbell, and M. A. Green, "The limiting efficiency of silicon solar cells under concentrated sunlight," *IEEE Transactions on Electron Devices,* vol. 33, no. 2, pp. 234-239, 1986.

[94] R. A. Sinton, and R. M. Swanson, "Recombination in highly injected silicon," *IEEE Transactions on Electron Devices,* vol. 34, no. 6, pp. 1380-1389, 1987.

[95] S. K. Pang, A. W. Smith, and A. Rohatgi, "Effect of trap location and trap-assisted Auger recombination on silicon solar cell performance," *IEEE Transactions on Electron Devices,* vol. 42, no. 4, pp. 662-668, 1995.

[96] K. Alberi, J. J. Berry, J. J. Cordell, D. J. Friedman, J. F. Geisz, A. R. Kirmani, B. W. Larson, W. E. McMahon, L. M. Mansfield, and P. F. Ndione, "A roadmap for tandem photovoltaics," *Joule*, 2024.

[97] A. S. Brown, and M. A. Green, "Detailed balance limit for the series constrained two terminal tandem solar cell," *Physica E: Low-dimensional Systems and Nanostructures,* vol. 14, no. 1-2, pp. 96-100, 2002.

[98] I. Almansouri, A. Ho-Baillie, S. P. Bremner, and M. A. Green, "Supercharging silicon solar cell performance by means of multijunction concept," *IEEE Journal of Photovoltaics,* vol. 5, no. 3, pp. 968-976, 2015.

[99] L. Mazzarella, Y. H. Lin, S. Kirner, A. B. Morales-Vilches, L. Korte, S. Albrecht, E. Crossland, B. Stannowski, C. Case, and H. J. Snaith, "Infrared light management using a nanocrystalline silicon oxide interlayer in monolithic perovskite/silicon heterojunction tandem solar cells with efficiency above 25%," *Advanced Energy Materials,* vol. 9, no. 14, pp. 1803241, 2019.

[100] S. Essig, C. Allebé, T. Remo, J. F. Geisz, M. A. Steiner, K. Horowitz, L. Barraud, J. S. Ward, M. Schnabel, and A. Descoeudres, "Raising the one-sun conversion efficiency of III–V/Si solar cells to 32.8% for two junctions and 35.9% for three junctions," *Nature Energy,* vol. 2, no. 9, pp. 1-9, 2017.

[101] J. Werner, B. Niesen, and C. Ballif, "Perovskite/silicon tandem solar cells: marriage of convenience or true love story?–An overview," *Advanced Materials Interfaces,* vol. 5, no. 1, pp. 1700731, 2018.

[102] G. E. Eperon, S. D. Stranks, C. Menelaou, M. B. Johnston, L. M. Herz, and H. J. Snaith, "Formamidinium lead trihalide: a broadly tunable perovskite for efficient planar heterojunction solar cells," *Energy & Environmental Science,* vol. 7, no. 3, pp. 982-988, 2014.

[103] A. W. Ho-Baillie, J. Zheng, M. A. Mahmud, F.-J. Ma, D. R. McKenzie, and M. A. Green, "Recent progress and future prospects of perovskite tandem solar cells," *Applied Physics Reviews,* vol. 8, no. 4, pp. 041307, 2021.

[104] J. Li, E. Alvianto, and Y. Hou, "Developing the next-generation perovskite/Si tandems: toward efficient, stable, and commercially viable photovoltaics," *ACS Applied Materials & Interfaces,* vol. 14, no. 30, pp. 34262-34268, 2022.

[105] F. Fu, J. Li, T. C. J. Yang, H. Liang, A. Faes, Q. Jeangros, C. Ballif, and Y. Hou, "Monolithic Perovskite‐Silicon Tandem Solar Cells: From the Lab to Fab?," *Advanced Materials,* vol. 34, no. 24, pp. 2106540, 2022.

[106] B. Chen, J. Y. Zhengshan, S. Manzoor, S. Wang, W. Weigand, Z. Yu, G. Yang, Z. Ni, X. Dai, and Z. C. Holman, "Blade-coated perovskites on textured silicon for 26%-efficient monolithic perovskite/silicon tandem solar cells," *Joule,* vol. 4, no. 4, pp. 850-864, 2020.

[107] M. De Bastiani, A. S. Subbiah, M. Babics, E. Ugur, L. Xu, J. Liu, T. G. Allen, E. Aydin, and S. De Wolf, "Bifacial perovskite/silicon tandem solar cells," *Joule,* vol. 6, no. 7, pp. 1431-1445, 2022.

[108] L. A. Zafoschnig, S. Nold, and J. C. Goldschmidt, "The race for lowest costs of electricity production: techno-economic analysis of silicon, perovskite and tandem solar cells," *IEEE Journal of Photovoltaics,* vol. 10, no. 6, pp. 1632-1641, 2020.

[109] D. Zhang, M. Najafi, V. Zardetto, M. Dörenkämper, X. Zhou, S. Veenstra, L. Geerligs, T. Aernouts, and R. Andriessen, "High efficiency 4-terminal perovskite/c-Si tandem cells," *Solar Energy Materials and Solar Cells,* vol. 188, pp. 1-5, 2018.

[110] M. A. Green, "Limiting efficiency of bulk and thin‐film silicon solar cells in the presence of surface recombination," *Progress in Photovoltaics: Research and Applications,* vol. 7, no. 4, pp. 327-330, 1999.

[111] N. v. Reich, W. Van Sark, E. Alsema, R. Lof, R. Schropp, W. Sinke, and W. Turkenburg, "Crystalline silicon cell performance at low light intensities," *Solar Energy Materials and Solar Cells,* vol. 93, no. 9, pp. 1471-1481, 2009.

[112] K. Rühle, M. K. Juhl, M. D. Abbott, and M. Kasemann, "Evaluating crystalline silicon solar cells at low light intensities using intensity-dependent analysis of I–V parameters," *IEEE Journal of Photovoltaics,* vol. 5, no. 3, pp. 926-931, 2015.

[113] V. Bhatnagar, and P. Owende, "Energy harvesting for assistive and mobile applications," *Energy Science & Engineering,* vol. 3, no. 3, pp. 153-173, 2015.

[114] M. Gorlatova, A. Wallwater, and G. Zussman, “Networking low-power energy harvesting devices: Measurements and algorithms,” *IEEE Transactions on Mobile Computing,* vol. 12, no. 9, pp. 1853-1865, 2012.

[115] A. Roy, A. Klinefelter, F. B. Yahya, X. Chen, L. P. Gonzalez-Guerrero, C. J. Lukas, D. A. Kamakshi, J. Boley, K. Craig, and M. Faisal, “A 6.45 mW Self-Powered SoC With Integrated Energy-Harvesting Power Management and ULP Asymmetric Radios for Portable Biomedical Systems,” *IEEE Transactions on biomedical circuits and systems,* vol. 9, no. 6, pp. 862-874, 2015.

[116] Z. L. Wang, and W. Wu, “Nanotechnology-enabled energy harvesting for self-powered micro-/nanosystems,” *Angewandte Chemie International Edition,* vol. 51, no. 47, pp. 11700-11721, 2012.

[117] T. Alam, “A reliable communication framework and its use in internet of things (IoT),” *CSEIT1835111| Received,* vol. 10, pp. 450-456, 2018.

[118] V. Bahrami-Yekta, and T. Tiedje, “Limiting efficiency of indoor silicon photovoltaic devices,” *Optics Express,* vol. 26, no. 22, pp. 28238-28248, 2018/10/29, 2018.

[119] CIE, "Commission internationale de l’eclairage proceedings," Cambridge University Press Cambridge, 1931.

[120] D. B. Judd, “Report of US secretariat committee on colorimetry and artificial daylight,” *CIE Proceedings, 1951,* vol. 1, pp. 11, 1951.

[121] J. J. Vos, “Colorimetric and photometric properties of a 2 fundamental observer,” *Color Research & Application,* vol. 3, no. 3, pp. 125-128, 1978.

[122] B. Thijs, L. Hanssens, G. Heremans, W. Wangermez, J. Rongé, and J. A. Martens, “Demonstration of a three compartment solar electrolyser with gas phase cathode producing formic acid from CO2 and water using Earth abundant metals,” *Frontiers in Chemical Engineering,* vol. 4, pp. 1028811, 2022.

[123] C. Ampelli, D. Giusi, M. Miceli, T. Merdzhanova, V. Smirnov, U. Chime, O. Astakhov, A. J. Martín, F. L. P. Veenstra, and F. A. G. Pineda, “An artificial leaf device built with earth-abundant materials for combined H 2 production and storage as formate with efficiency> 10%,” *Energy & Environmental Science,* vol. 16, no. 4, pp. 1644-1661, 2023.

[124] O. Kunz, R. J. Evans, M. K. Juhl, and T. Trupke, “Understanding partial shading effects in shingled PV modules,” *Solar Energy,* vol. 202, pp. 420-428, 2020.

[125] H. Schulte-Huxel, S. Blankemeyer, A. Morlier, R. Brendel, and M. Köntges, “Interconnect-shingling: Maximizing the active module area with conventional module processes,” *Solar Energy Materials and Solar Cells,* vol. 200, pp. 109991, 2019.

[126] S. R. Droes, T. T. Kodas, and M. J. Hampden-Smith, "Plasma-enhanced chemical vapor deposition (PECVD)," *Carbide, nitride and boride materials synthesis and processing*, pp. 579-603: Springer, 1997.

[127] J. M. Sebastian Gatz, Christian Schmidt, Mirko Kehr, Erik Ansorge, Egbert Vetter, "Novel Plasma Reactor Principle for Amorphous Silicon Deposition Enabling High Efficiency Energy Conversion."

[128] F. Shi, “Introductory chapter: basic theory of magnetron sputtering,” 2018.

[129] A. Lorenz, M. Linse, H. Frintrup, M. Jeitler, A. Mette, M. Lehner, R. Greutmann, H. Brocker, M. König, and D. Erath, "Screen printed thick film metallization of silicon solar cells—recent developments and future perspectives." pp. 819-824.

[130] S. Tepner, and A. Lorenz, “Printing technologies for silicon solar cell metallization: A comprehensive review,” *Progress in Photovoltaics: Research and Applications,* vol. 31, no. 6, pp. 557-590, 2023.

[131] Z. Wang, and Z. Zhang, "Electron Beam Evaporation Deposition," *Advanced Nano Deposition Methods*, pp. 33-58, 2016.

[132] T. Rudolf, “Application of Intensive Light Soaking on Silicon Heterojunction Solar Cells and Modules,” Department of Physics RWTH Aachen University, RWTH Aachen University, 2022.

[133] S. Bowden, and A. Rohatgi, "Rapid and accurate determination of series resistance and fill factor losses in industrial silicon solar cells."

[134] U. Chime, L. Wolf, V. Buga, D. Weigand, A. Gad, J. Köhler, A. Lambertz, W. Duan, K. Ding, T. Merdzhanova, U. Rau, and O. Astakhov, “How Thin Practical Silicon Heterojunction Solar Cells Could Be? Experimental Study under 1 Sun and under Indoor Illumination,” *Solar RRL,* vol. 6, no. 1, pp. 2100594, 2022.

[135] T. Koida, H. Sai, and M. Kondo, “Application of hydrogen-doped In2O3 transparent conductive oxide to thin-film microcrystalline Si solar cells,” *Thin Solid Films,* vol. 518, no. 11, pp. 2930-2933, Mar 31, 2010.

[136] P. Altermatt, A. Schenk, and G. Heiser, “A simulation model for the density of states and for incomplete ionization in crystalline silicon. I. Establishing the model in Si: P,” *Journal of Applied Physics,* vol. 100, no. 11, pp. 113715, 2006.

[137] T. Trupke, M. A. Green, P. Würfel, P. Altermatt, A. Wang, J. Zhao, and R. Corkish, “Temperature dependence of the radiative recombination coefficient of intrinsic crystalline silicon,” *Journal of Applied Physics,* vol. 94, no. 8, pp. 4930-4937, 2003.

[138] L. E. Black, and D. H. Macdonald, “On the quantification of Auger recombination in crystalline silicon,” *Solar Energy Materials and Solar Cells,* vol. 234, pp. 111428, 2022.

[139] C. Diestel, S. Kumar, N. Schüler, M. Leonhardt, J. Haunschild, and S. Rein, "Comparing MDP, QSSPC and PL Imaging for the Production Control of Heterojunction Solar Cells."

[140] R. Dumbrell, M. K. Juhl, T. Trupke, and Z. Hameiri, “Comparison of terminal and implied open-circuit voltage measurements,” *IEEE Journal of Photovoltaics,* vol. 7, no. 5, pp. 1376-1383, 2017.

[141] A. Cuevas, and S. López-Romero, “The combined effect of non-uniform illumination and series resistance on the open-circuit voltage of solar cells,” *Solar Cells,* vol. 11, no. 2, pp. 163-173, 1984.

[142] J. Greulich, M. Glatthaar, A. Krieg, G. Emanuel, and S. Rein, “JV characteristics of industrial silicon solar cells: Influence of distributed series resistance and Shockley Read Hall recombination,” *network,* vol. 6, no. 8, pp. 10, 2009.

[143] E. T. Roe, K. E. Egelhofer, and M. C. Lonergan, “Limits of contact selectivity/recombination on the open-circuit voltage of a photovoltaic,” *ACS Applied Energy Materials,* vol. 1, no. 3, pp. 1037-1046, 2018.

[144] R. Brendel, and R. Peibst, “Contact Selectivity and Efficiency in Crystalline Silicon Photovoltaics,” *IEEE Journal of Photovoltaics,* vol. 6, no. 6, pp. 1413-1420, 2016.

[145] U. Rau, and T. Kirchartz, “Charge carrier collection and contact selectivity in solar cells,” *Advanced materials interfaces,* vol. 6, no. 20, pp. 1900252, 2019.

[146] A. Onno, C. Chen, and Z. C. Holman, "Electron and hole partial specific resistances: a framework to understand contacts to solar cells." pp. 2329-2333.

[147] S. Harrison, O. Nos, A. Danel, D. Muñoz, J. Rakotoniaina, J. Gaume, C. Roux, and P. Ribeyron, "How to Deal with Thin Wafers in a Heterojunction Solar Cells

Industrial Pilot Line: First Analysis of the Integration of Cells Down to 70 μm Thick in Production Mode." pp. 358-362.

[148] A. Danel, S. Harrison, F. Gérenton, A. Moustafa, R. Varache, J. Veirman, and C. Roux, "Silicon heterojunction solar cells with open-circuit-voltage above 750mV." pp. 444-447.

[149] H. Sai, T. Oku, Y. Sato, M. Tanabe, T. Matsui, and K. Matsubara, "Potential of very thin and high-efficiency silicon heterojunction solar cells," *Progress in Photovoltaics: Research and Applications,* vol. 27, no. 12, pp. 1061-1070, 2019, 2019.

[150] A. Richter, J. Benick, F. Feldmann, A. Fell, M. Hermle, and S. W. Glunz, "n-Type Si solar cells with passivating electron contact: Identifying sources for efficiency limitations by wafer thickness and resistivity variation," *Solar Energy Materials and Solar Cells,* vol. 173, pp. 96-105, 2017.

[151] U. Chime, W. Duan, A. Lambertz, K. Bittkau, V. Lauterbach, K. Ding, U. Rau, T. Merdzhanova, and O. Astakhov, "Thin silicon heterojunction solar cells in perovskite shadow: Bottom cell prospective," *Solar Energy Materials and Solar Cells,* vol. 270, pp. 112813, 2024.

[152] H. Sai, H. Umishio, T. Matsui, S. Nunomura, T. Kawatsu, H. Takato, and K. Matsubara, "Impact of silicon wafer thickness on photovoltaic performance of crystalline silicon heterojunction solar cells," *Japanese Journal of Applied Physics,* vol. 57, no. 8S3, pp. 08RB10, 2018, 2018.

[153] D. L. Staebler, and C. Wronski, "Reversible conductivity changes in discharge-produced amorphous Si," *Applied physics letters,* vol. 31, no. 4, pp. 292-294, 1977.

[154] P. Mahtani, R. Varache, B. Jovet, C. Longeaud, J.-P. Kleider, and N. P. Kherani, "Light induced changes in the amorphous—crystalline silicon heterointerface," *Journal of Applied Physics,* vol. 114, no. 12, pp. 124503, 2013.

[155] P. Pathi, A. Peer, and R. Biswas, "Nano-photonic structures for light trapping in ultra-thin crystalline silicon solar cells," *Nanomaterials,* vol. 7, no. 1, pp. 17, 2017.

[156] H.-S. Kim, D. B. Patel, H. Kim, M. Patel, K. R. Chauhan, W. Park, and J. Kim, "Electrical and optical properties of Si microwire solar cells," *Solar Energy Materials and Solar Cells,* vol. 164, pp. 7-12, 2017.

[157] P. Bermel, C. Luo, L. Zeng, L. C. Kimerling, and J. D. Joannopoulos, “Improving thin-film crystalline silicon solar cell efficiencies with photonic crystals,” *Optics express,* vol. 15, no. 25, pp. 16986-17000, 2007.

[158] L. Zeng, P. Bermel, Y. Yi, B. Alamariu, K. Broderick, J. Liu, C. Hong, X. Duan, J. Joannopoulos, and L. Kimerling, “Demonstration of enhanced absorption in thin film Si solar cells with textured photonic crystal back reflector,” *Applied Physics Letters,* vol. 93, no. 22, pp. 221105, 2008.

[159] F. Sahli, J. Werner, B. A. Kamino, M. Bräuninger, R. Monnard, B. Paviet-Salomon, L. Barraud, L. Ding, J. J. Diaz Leon, and D. Sacchetto, “Fully textured monolithic perovskite/silicon tandem solar cells with 25.2% power conversion efficiency,” *Nature materials,* vol. 17, no. 9, pp. 820-826, 2018.

[160] O. Astakhov, T. Merdzhanova, L.-C. Kin, and U. Rau, “From room to roof: How feasible is direct coupling of solar-battery power unit under variable irradiance?,” *Solar Energy,* vol. 206, pp. 732-740, 2020.

[161] D. Kiermasch, L. Gil-Escrig, H. J. Bolink, and K. Tvingstedt, “Effects of masking on open-circuit voltage and fill factor in solar cells,” *Joule,* vol. 3, no. 1, pp. 16-26, 2019.

[162] S. Shcherbachenko, O. Astakhov, U. Chime, L.-C. Kin, K. Ding, B. Pieters, U. Rau, E. Figgemeier, and T. Merdzhanova, “Efficient Power Coupling in Directly Connected Photovoltaic-Battery Module,” *Solar RRL,* vol. 7, no. 3, pp. 2200857, 2023.

Acknowledgements

Completing this PhD has been a long and deeply meaningful journey, and I would not have reached this point without the support, guidance, kindness, and encouragement of many people.

I gratefully acknowledge the German Academic Exchange Service (DAAD) for the scholarship that enabled me to pursue my doctoral studies in Germany. I am deeply grateful for the opportunity and financial support that made this important chapter of my academic journey possible.

Dr. Tsvetelina Merdzhanova, thank you for your genuine kindness and for your supervision throughout my PhD. Thank you for being an exceptional group leader and for your patience, understanding, and generosity. I have learned a great deal from you, both scientifically and professionally, and I am grateful for the many things you have taught me along the way. Your dedication, hard work, and commitment to the group have been a great example to me. Thank you also for your support and encouragement throughout this journey.

Dr. Oleksandr Astakhov, thank you for your invaluable supervision and contribution to my PhD. Thank you for the knowledge you shared with me, your patience in teaching and explaining complex concepts, and your willingness to engage in countless scientific discussions. I have learned a great deal from you throughout my PhD, and I am deeply grateful for your kind words, encouragement, and support along the way.

Professor Uwe Rau, thank you for giving me the opportunity to be your PhD student and for your guidance and supervision throughout these years. I am also grateful for your support and encouragement, particularly in helping me bring this thesis to completion.

Professor Joachim Knoch, thank you for serving as the second reviewer of my doctoral thesis and for taking the time to carefully evaluate this work.

Daniel Weigand, thank you for being so resourceful and helpful throughout my PhD, particularly with wafer cutting, and especially the fabrication of my modules. Your practical support was an important part of the experimental work carried out in this thesis.

Joachim Kirchhoff, thank you for always being ready to help and for bringing such a positive spirit to the workplace. Your willingness to help and your consistently good mood made a difference, especially on the more stressful days.

To the Silicon Heterojunction baseline group, thank you for the knowledge, expertise, collaboration, and support that contributed to my research throughout these years. Dr. Kaining Ding, Dr. Weiyan Duan, Dr. Karsten Bittkau, and Dr. Andreas Lambertz, thank you for your invaluable collaboration, scientific advice, and discussions throughout parts of my PhD research and the resulting publications. Your work in developing and establishing the SHJ baseline also provided an important scientific foundation for much of the research presented in this thesis.

Volker Lauterbach, Alain Doumit, Sylke Lynen, Dr. Alexander Eberst, Dr. Kai Zhang, Hildegard Siekmann and Henrike Gattermann, thank you for your practical and technical support with the deposition and fabrication of my silicon heterojunction solar cells. Volker, a special thank you for your incredible patience and hard work through the dozens and hundreds of depositions you carried out for my experiments. I truly appreciate your dedication and willingness to keep going through all those samples. Kai, thank you particularly for your help with the encapsulation of my modules.

Wilfred Reetz and Christoph Zahren, thank you for your help with the characterization of my cells and modules in the laboratory. Timon Vaas, thank you for always being ready to help with the photoluminescence and electroluminescence characterization.

To my fellow PhD colleagues, Li-Chung, Sergey, Thérèse, Uchechi, Goodfriend, Ifeanyi, Suheir, Alex, Kai, Timon, and the many others who shared this journey with me, thank you for your friendship, collaboration, encouragement, and for the wonderful times we had together. Sharing the challenges and experiences of a PhD with people who understand the journey made it a lot more meaningful.

Dr. Suheir Nofal, thank you for always being ready to help and for generously sharing important information and advice with me, particularly during these final stages of my PhD. Your support has been greatly appreciated.

Dr. Solomon Agbo, thank you for being instrumental throughout every step of my PhD journey. Without your support and encouragement, I may not have made it to Germany in the first place. Thank you for believing in me, for your guidance and advice over the years, and for being there at so many important moments along this journey. Your contribution to both my academic and personal journey has been immense, and I will always be deeply grateful for it.

Professor Fabian Ezema, thank you for being a mentor to me and for introducing me to the world of scientific research. Your guidance played an important role in shaping my academic journey and in encouraging me to pursue research.

To my Mummy and Daddy, Akunna and Sunny Chime, thank you for giving me the foundation upon which I have built my life, for believing in me, and for always encouraging me to pursue my dreams. Your sacrifices, prayers, love, and unwavering support have carried me through every stage of my life.

To my sisters, Nneoma, Obiamaka, Modupe, Nkiru, Mmasi, Chikky, and Nesochi, thank you for being an important part of my life and for sharing this journey with me in your own ways. I am grateful for your love, support, and for simply being there.

To my dear friends, Perfect, Esther, Georgette, Eziama, Princess, and Mary, thank you for your friendship, love, encouragement, and support throughout the years. Thank you for being there for me, for listening, for celebrating my successes, and for standing by me through the difficult moments. I am grateful for each of you and for the special place you have in my life.

To my precious, darling husband, Nnamdi, thank you for sharing this life with me and for carrying so much alongside me during these years. Thank you for your patience with the long days, the deadlines, the disappointments, and all the moments when the PhD seemed to take over everything. Thank you for making me laugh when I needed it most, for believing in me when I doubted myself, and for giving me a home and a family that made all the hard work worthwhile. And, of course, thank you for our three beautiful children, who are the greatest gifts of our life together.

Kenenna, Usonna, and Ugonna, thank you for being the greatest joy in my life. Thank you for filling my days with laughter, love, and purpose, and for reminding me that there is a world beyond experiments, measurements, papers, and deadlines. You have been a very important part of this journey, even if you did not always understand why Mummy had to work so much.

To everyone whom I have not mentioned by name but who has, in one way or another, influenced my life or contributed to my journey, thank you. Your kindness, support, encouragement, advice, and contributions, however big or small, have not gone unnoticed, and I am sincerely grateful.

Above all, my deepest gratitude goes to God the Father, the Son, and the Holy Spirit. Thank You for Your grace, guidance, strength, and faithfulness throughout this journey. Through every challenge, uncertainty, disappointment, and success, You have sustained me. Without You, there is no me.

Band / Volume 725
Synthese und Bewertung hochaktiver Katalysatoren zur Herstellung höherer Alkohole aus Methanol als Kraftstoff
J. Häusler (2026), xiii, 265 Seiten
ISBN: 978-3-95806-962-6 (Print)
ISBN: 978-3-95806-963-3 (E-Book)

Band / Volume 726
Development and Characterization of Ni_3Fe Layered Double Hydroxide-Based Oxygen-Evolution Electrodes for Anion Exchange Membrane Water Electrolysis
I.Galkina (2026), vii, 173, xxxiii Seiten
ISBN: 978-3-95806-966-4 (Print)
ISBN: 978-3-95806-967-1 (E-Book)

Band / Volume 727
Surface Regeneration of Plasma-Facing Components by Wire-Based Laser Metal Deposition
J. Tweer (2026), XX, 186 pp
ISBN: 978-3-95806-970-1 (Print)
ISBN: 978-3-95806-971-8 (E-Book)

Band / Volume 728
Reducing the noble metal and titanium content of anode PTLs in PEM water electrolysis – performance and degradation
S. Zerressen (2026), XIII, 235 pp
ISBN: 978-3-95806-972-5 (Print)
ISBN: 978-3-95806-973-2 (E-Book)

Band / Volume 729
Gasfernleitungsnetze und deren Umstellung auf Wasserstoff
T. A. Triesch (2026), 364 pp
ISBN: 978-3-95806-978-7 (Print)
ISBN: 978-3-95806-979-4 (E-Book)

Band / Volume 730
Land-Atmosphere Coupling in a Changing Climate: Understanding Variability, Extremes, and Human Influence through Regional Climate Modeling
Y. Zhang (2026), 135 pp
ISBN: 978-3-95806-980-0 (Print)
ISBN: 978-3-95806-981-7 (E-Book)

Band / Volume 731
Abbildung gekoppelter Infrastrukturen in Energiesystemmodellen
P. Freitag (2026), XIX, 322 pp
ISBN: 978-3-95806-984-8 (Print)
ISBN: 978-3-95806-985-5 (E-Book)

Band / Volume 732
Cost-reduced and Sustainable Interconnects and their Coatings for Solid Oxide Cells
M. Hilger (2026), viii, 185 pp
ISBN: 978-3-95806-988-6 (Print)
ISBN: 978-3-95806-989-3 (E-Book)

Band / Volume 733
Liquid-Phase Synthesis of Silicon and Silicon Carbide Thin-Films via Atmospheric Pressure Chemical Vapor Deposition
B. Fischer (2026), xxii, 211, A15 pp
ISBN: 978-3-95806-990-9 (Print)
ISBN: 978-3-95806-991-6 (E-Book)

Band / Volume 734
Modellgestützte Transformationspfade des deutschen Energiesystems
R. Maier (2026), xxvii, 331 pp
ISBN 978-3-95806-994-7 (Print)
ISBN 978-3-95806-995-4 (E-Book)

Band / Volume 735
Dynamical drivers of deep and shallow branches in the stratospheric circulation and transport
R.- A. Baikhadzhaev (2026), 120 pp
ISBN 978-3-95806-996-1 (Print)
ISBN 978-3-95806-997-8 (E-Book)

Band / Volume 736
Silicon heterojunction solar cells on thin wafers – prospects in different utilization scenarios
U. K. Chime (2026), 151 pp
ISBN 978-3-95806-998-5 (Print)
ISBN 978-3-95806-999-2 (E-Book)

Energie & Umwelt / Energy & Environment
Band / Volume 736
ISBN 978-3-95806-999-2

JÜLICH
Forschungszentrum